論文 / 著書情報
Article / Book Information

題目(和文)	
Title(English)	Development of Novel Ferroelectrics Utilizing Distortions of Non-Lead Cations
著者(和文)	福田真幸
Author(English)	Masayuki Fukuda
出典(和文)	学位:博士(理学), 学位授与機関:東京工業大学, 報告番号:甲第11708号, 授与年月日:2022年3月26日, 学位の種別:課程博士, 審査員:東 正樹,舟窪 浩,川路 均,笹川 崇男,山本 隆文
Citation(English)	Degree:Doctor (Science), Conferring organization: Tokyo Institute of Technology, Report number:甲第11708号, Conferred date:2022/3/26, Degree Type:Course doctor, Examiner:,,,,
学位種別(和文)	博士論文
Type(English)	Doctoral Thesis

Development of Novel Ferroelectrics Utilizing Distortions of Non-Lead Cations

(非鉛カチオンの歪みを利用した新規強誘電体の開発)

Masayuki Fukuda
(Supervisor: Professor Masaki Azuma)

A Thesis

School of Materials and Chemical Technology
Tokyo Institute of Technology

List of Contents

Chapter 1. General Introduction

1.1 Perovskite Oxides

Some materials exhibit ferroelectricity below the phase transition temperature (Curie temperature, T_C), whereas they adapt paraelectric phases at high temperatures. Because of ion displacements with respect to the nonpolar references, ferroelectric materials exhibit spontaneous polarization, P_s. The direction of P_s can be reversed by an external electric field. Such switchable polarization provides electromechanical properties such as piezoelectricity.[1] Ferroelectrics, therefore, find various applications, such as actuators and sensors. Since the first report of ferroelectricity in Rochelle salts 100 years ago,[2] numerous ferroelectric materials have been studied. The most studied ferroelectrics are ferroelectric perovskite oxides, such as $PbTiO_3$ and $BaTiO_3$.[3,4] They have the composition of ABO_3, where A and B are cations. The wide variety of physical properties, such as ferroelectric, ferromagnetic, and catalytic properties, has been reported in perovskite oxides. Such excellent properties are governed by the composition and/or structural features, especially cation-cation, cation-vacancy and oxygen-vacancy orderings. The aristotype perovskite adopts a simple cubic space group $Pm\bar{3}m$ consisting of 5 atoms in a unit cell. In the ideal perovskite structure, the B cation is at the center of BO_6 octahedra. The octahedra are linked by sharing their corners into a three-dimensional network. Each A cation is surrounded by 12 equivalent O ions. The structural stability of perovskite oxides is evaluated using the Goldschmidt tolerance factor,[5]

$$t = (r_A + r_O) / \sqrt{2}(r_B + r_O),$$

where r_A, r_B and r_O are the ionic radii of twelve-coordinated A-cation, six-coordinated B-cation, and two-coordinated O anion. These values can be obtained from Shannon's reports,[6,7] or they can be calculated in bond valence sum analysis when Shannon's radii are not available.[8,9] As t values increase or decrease from 1, the distortion from $Pm\bar{3}m$ perovskite structure increases (Figure 1).

When $t > 1$, the B cation is too small for the oxygen octahedra so that the perovskite compound will show a polar displacement of the B cation, as in $BaTiO_3$. When $t = 1$, the perovskite compound crystalizes into the ideal cubic phase, as seen in $SrTiO_3$. On the other hand, for $t < 1$, the A cation is small for the space surrounded by the oxygen octahedra, leading to the BO_6 tilts ($GdFeO_3$-type tilts as in $CaTiO_3$). If t is significantly small, the compound will favor a more distorted structure, such as a $LiNbO_3$-type structure where A cations are coordinated by only six anions. $LiNbO_3$-type compounds yield a combination of the large tilts of BO_6 octahedra and polar displacements of A- and B-site cations along the same axis. $LiNbO_3$-type compounds have so large structural distortions that they are seldom obtained by conventional solid-phase reactions. Therefore, $LiNbO_3$-type compounds have been often obtained under extreme conditions such as high pressure, as reported in $LiNbO_3$-type $MnTiO_3$.[10] The $LiNbO_3$-type compounds are very important groups of materials because of their ferroelectricity and optical second harmonic generation.

1.2 Mechanism of Ferroelectric Distortions

Ferroelectrics are classified according to their mechanisms, such as displacement type and order-disorder type. Herein, two significant effects, first- or second-order Jahn-Teller distortion and stereochemical activity of ns^2 lone pairs are introduced, which widely work in displacement-type ferroelectrics. The mechanism of the Jahn–Teller effect can be highlighted in a perturbative expansion of the total energy E, of a system with Hamiltonian $\mathcal{H}$ in terms of the nuclear displacement, Q.[1]

$$E(Q) = E(0) + \langle 0|(\partial\mathcal{H}/\partial Q)_0|0\rangle Q + 1/2[\langle 0|(\partial^2\mathcal{H}/\partial Q^2)_0|0\rangle - 2\textstyle\sum_n \frac{|\langle 0|(\partial\mathcal{H}/\partial Q)_0|n\rangle|^2}{E_n - E_0}]Q^2 + \ldots$$

The first term, $E(0)$, refers to the total energy of the ground state. The second term is the contribution of the first-order Jahn–Teller distortion, which works only for nonzero d-electron systems with degenerate electronic ground states. This term leads the characteristic pyramidal distortions in d^1 and d^6 perovskites such as V^{4+} in $PbVO_3$ (Figure 2) and Co^{3+} in $BiCoO_3$.[11,12] The pyramidal VO_5 coordination lifts the degeneracy of t_{2g} orbitals, and the one d-electron of V^{4+} occupies the d_{xy} orbital lowered in energy. The third and fourth terms are the contribution of the second-order Jahn-Teller distortion, whose sign is determined by the magnitude of the two terms, $\langle 0|(\partial^2\mathcal{H}/\partial Q^2)_0|0\rangle$ and $2\sum_n \frac{|\langle 0|(\partial\mathcal{H}/\partial Q)_0|n\rangle|^2}{E_n - E_0}$. These terms provide off-center displacements of d^0 metal cations such as Ti^{4+} in $BaTiO_3$. The second-order Jahn-Teller distortion is associated with the hybridization of the empty d orbital of the metal and the O 2p orbital. It has been reported that large off-center displacements are observed in the order of d^0 cations' electronegativity: Os^{8+}, Mo^{6+}, W^{6+}, V^{5+}, Nb^{5+}, Ti^{4+}, Ta^{5+}, Hf^{4+}, Zr^{4+}, Re^{7+} and Y^{3+}.[13,14]

On the other hand, the stereochemical activity of ns_2 lone pairs also play a key role in ferroelectrics. Pb^{2+} is the most studied cation with this activity. It is known that the secondary Jahn-Teller effect of Ti^{4+} and the stereochemical effect of Pb^{2+} coexist in $PbTiO_3$ as shown in the charge density map (Figure 3).[15] $PbTiO_3$ exhibits a spontaneous polarization value about three times as large as that of $BaTiO_3$, in which only the former exists.[16] Bi^{3+} has the same electronic configuration as Pb^{2+}, and bismuth-based polar perovskite such as $BiFeO_3$ have also been attracting much attention.

1.3 Lead-Based and Lead-Free Ferroelectrics

Due to the stereochemical activity of Pb^{2+}, lead-based ferroelectrics show superior ferroelectric performance and high Curie temperature. Among them, $Pb(Zr,Ti)O_3$ (PZT) is the most commercially used piezoceramics. Since it was first reported in 1951,[17] PZT has been used for a long time.[18] In recent years, however, environmental considerations have restricted the use of lead-containing materials, and the development of lead-free ferroelectrics is attracting more and more attention, as shown in the increasing papers on lead-free ferroelectrics (Figure 4).[19,20] The example of currently studied lead-free ferroelectrics includes $BaTiO_3$, $Bi_{0.5}Na_{0.5}TiO_3$, $K_{0.5}Na_{0.5}NbO_3$, $AgNbO_3$, $NaNbO_3$, and $BiFeO_3$-based materials, having second-order Jahn-Teller distortion of d^0 cations or stereochemical activity of Bi^{3+}. Development of lead-free ferroelectrics utilizing these materials that can replace PZT is underway, not only by improving intrinsic factors such as crystal structure but also by improving extrinsic factors such as domain engineering.[21,22] However, the developed materials are unfortunately not yet at the stage of practical use, and a breakthrough in lead-free ferroelectric is required.

1.4 Polar Materials Synthesized at High Pressure

As described in 1.1, the application of high pressure stabilizes metastable phases inaccessible under ambient pressures. In particular, new perovskites and related oxides have emerged through exploration of the high-pressure and high-temperature phases of ABO_3 ternary systems.[23–25] Especially, many $LiNbO_3$-type polar materials have been synthesized as retrograde products of high-pressure perovskite phases during decompression.[10,26–28] About 20 $LiNbO_3$-type compounds have been obtained by high-pressure synthesis, whereas only 6 $LiNbO_3$-type oxides have been reported by conventional solid-state reactions under ambient pressure. In addition to $LiNbO_3$, other lead-free polar materials such as $BiInO_3$ and $CaMnTi_2O_6$ have been synthesized by high-pressure synthesis,[29,30] indicating the importance of this technology.

1.5 Objective of This Thesis

The objective of this thesis is to establish a novel strategy for lead-free ferroelectrics. In my thesis, by using the high-pressure synthesis technique, I have developed compounds with first- and second-order Jahn-Teller active cations, V^{4+} and Nb^{5+}. The first-order Jahn-Teller active V^{4+} has the potential to exhibit larger displacement than second-order active d^0 metals. Nb^{5+}-based perovskites are the most studied lead-free ferroelectrics, and it is important to extend their compositional space.

First, I succeeded in enhancing the spontaneous polarization in a novel lead-free compound, $CaMnTi_2O_6$, by partial V^{4+} substitution for Ti^{4+}. This enhancement was achieved by the combination of a first-order Jahn-Teller active V^{4+} ion and an order-disorder mechanism in $CaMnTi_2O_6$. On the other hand, the presence of antisite disorder between Ca^{2+} and Mn^{2+} associated with Mn−V inter-metallic charge transfer resulted in decreases in spontaneous polarization in V^{4+}-rich composition.

Next, I synthesized a novel perovskite niobite, $CuNbO_3$. I found this material shows a complex dipole ordering at room temperature, called "noncollinear ferrielectric", where Cu^{+} ions are displaced almost parallel along one axis and Nb^{5+} ions move almost antiparallel along another axis. Interestingly, at 470 K, this compound transforms into a phase with collinear ferroelectric dipole order where Cu^{+} and Nb^{5+} displace parallel with each other. Immediately after the phase transition, $CuNbO_3$ decomposes into Cu and perovskite-type $CuNb_2O_6$. The latter is a newly found metastable material, and its crystal structure and physical properties were investigated. This compound crystallizes in an A-site deficient quadruple perovskite structure and exhibits a colossal dielectric constant up to 10^4. This colossal value can be attributed to extrinsic effects, i.e., space charges, as previously reported in related compounds, $CaCu_3Ti_4O_{12}$ and $CuTa_2O_6$.[31,32]

1.6 Figures

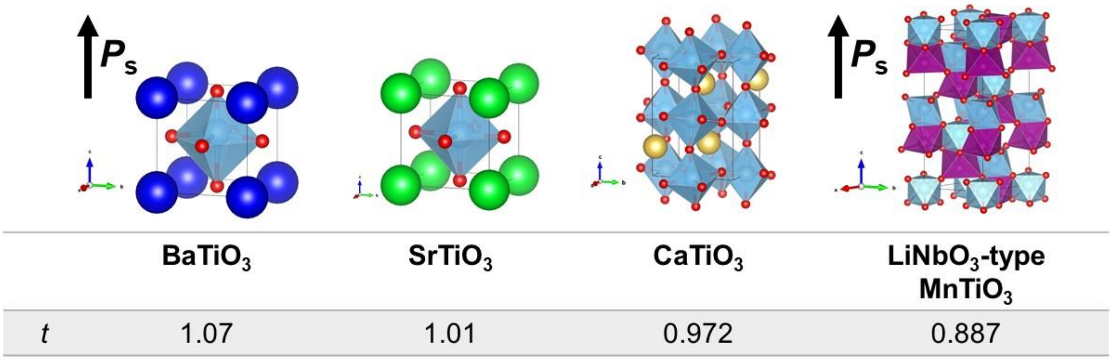

	$BaTiO_3$	$SrTiO_3$	$CaTiO_3$	$LiNbO_3$-type $MnTiO_3$
t	1.07	1.01	0.972	0.887

Figure 1. Variation of structural distortion in perovskite oxides depending on the *t* values.

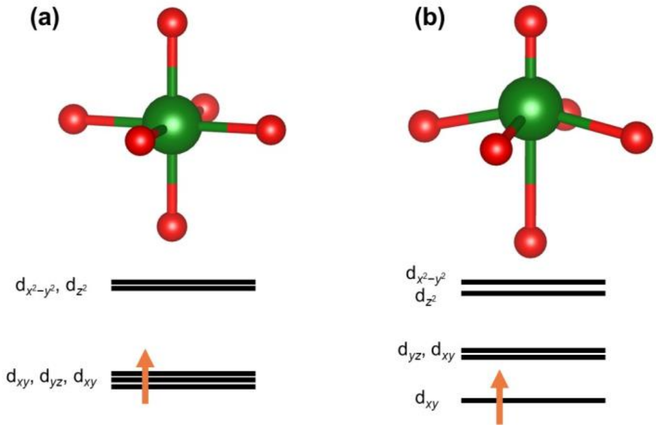

Figure 2. VO_6 octahedra and the corresponding energy diagram (a) without and (b) with the first-order Jahn-Teller distortion of V^{4+}.

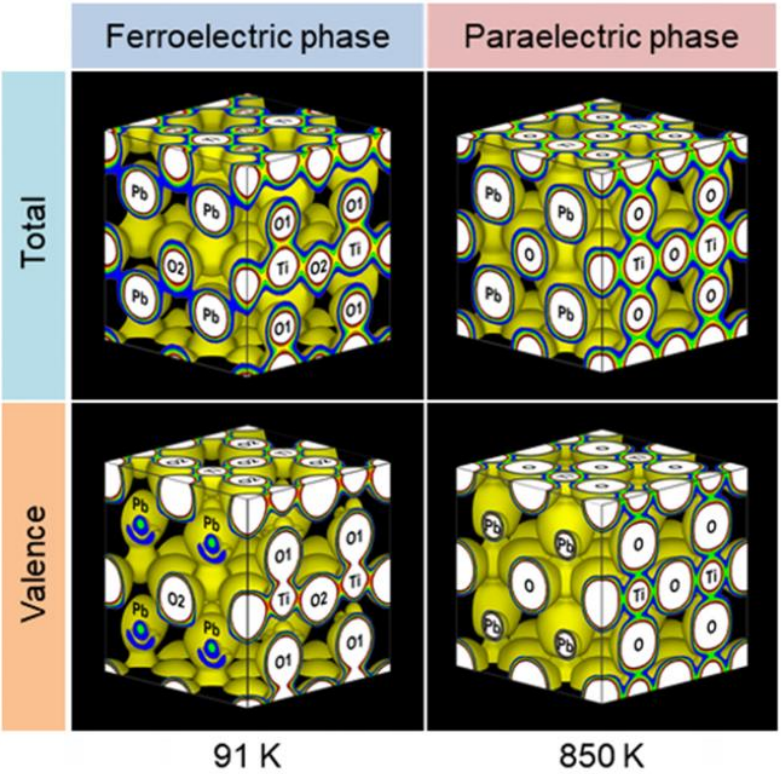

Figure 2. Total and valence electron density distributions of $PbTiO_3$ in ferroelectric and paraelectric phases, obtained by the maximum entropy method/Rietveld analysis. Reproduced from Ref 15, with the permission of AIP Publishing.

Figure 3. (a) The number of papers about lead-base and lead-free materials. Reproduced from Ref. 20 with permission from the Royal Society of Chemistry.

1.7 References

(1) Rabe, K. M.; Ahn, C. H.; Triscone, J.-M. *Physics of Ferroelectrics: A Modern Perspective*, 2007th ed.; Springer, 2007.

(2) Valasek, J. Piezo-Electric and Allied Phenomena in Rochelle Salt. *Phys. Rev.* **1921**, *17* (4), 475–481.

(3) Bhide, V. G.; Deshmukh, K. G.; Hegde, M. S. Ferroelectric Properties of $PbTiO_3$. *Physica* **1962**, *28* (9), 871–876.

(4) Bersuker, I. B. On the Origin of Ferroelectricity in Perovskite-Type Crystals. *Physics Letters* **1966**, *20* (6), 589–590.

(5) Goldschmidt, V. M. Die Gesetze Der Krystallochemie. *Naturwissenschaften* **1926**, *14* (21), 477–485.

(6) Shannon, R. D.; Prewitt, C. T. Effective Ionic Radii in Oxides and Fluorides. *Acta Crystallogr. B* **1969**, *25* (5), 925–946.

(7) Shannon, R. D. Revised Effective Ionic Radii and Systematic Studies of Interatomic Distances in Halides and Chalcogenides. *Acta Crystallogr. A* **1976**, *32* (5), 751–767.

(8) Brese, N. E.; O'Keeffe, M. Bond-Valence Parameters for Solids. *Acta Crystallogr. B* **1991**, *47* (2), 192–197.

(9) Whangbo, M.-H.; Gordon, E. E.; Bettis, J. L., Jr; Bussmann-Holder, A.; Köhler, J. Tolerance Factor and Cation-Anion Orbital Interactions Differentiating the Polar and Antiferrodistortive Structures of Perovskite Oxides ABO_3. *Z. Anorg. Allg. Chem.* **2015**, *641* (6), 1043–1052.

(10) Ko, J.; Prewitt, C. T. High-Pressure Phase Transition in $MnTiO_3$ from the Ilmenite to the $LiNbO_3$ Structure. *Phys. Chem. Miner.* **1988**, *15* (4), 355–362.

(11) Belik, A. A.; Azuma, M.; Saito, T.; Shimakawa, Y.; Takano, M. Crystallographic Features and Tetragonal Phase Stability of $PbVO_3$, a New Member of PbTiO3 Family. *Chem. Mater.* **2005**, *17* (2), 269–273.

(12) Oka, K.; Yamada, I.; Azuma, M.; Takeshita, S.; Satoh, K. H.; Koda, A.; Kadono, R.; Takano, M.; Shimakawa, Y. Magnetic Ground-State of Perovskite $PbVO_3$ with Large Tetragonal Distortion. *Inorg. Chem.* **2008**, *47* (16), 7355–7359.

(13) Kunz, M.; Brown, I. D. Out-of-Center Distortions around Octahedrally Coordinated D^0 Transition Metals. *J. Solid State Chem.* **1995**, *115* (2), 395–406.

(14) Gagné, O. C.; Hawthorne, F. C. Bond-Length Distributions for Ions Bonded to Oxygen: Results

for the Transition Metals and Quantification of the Factors Underlying Bond-Length Variation in Inorganic Solids. *IUCrJ* **2020**, *7* (Pt 4), 581–629.

(15) Abe, T.; Kim, S.; Moriyoshi, C.; Kitanaka, Y.; Noguchi, Y.; Tanaka, H.; Kuroiwa, Y. Visualization of Spontaneous Electronic Polarization in Pb Ion of Ferroelectric $PbTiO_3$ by Synchrotron-Radiation x-Ray Diffraction. *Appl. Phys. Lett.* **2020**, *117* (25), 252905.

(16) Jaffe, B.; Cook-Jr, W. R.; Jaffe, H. *Piezoelectric Ceramics*; Academic Press London and New York, 1971.

(17) Shirane, G.; Sawaguchi, E.; Takagi, Y. Dielectric Properties of Lead Zirconate. *Phys. Rev.* **1951**, *84* (3), 476–481.

(18) Guo, R.; Cross, L. E.; Park, S. E.; Noheda, B.; Cox, D. E.; Shirane, G. Origin of the High Piezoelectric Response in $PbZr_{1-x}Ti_xO3$. *Phys. Rev. Lett.* **2000**, *84* (23), 5423–5426.

(19) Coondoo, I.; Panwar, N.; Kholkin, A. Lead-Free Piezoelectrics: Current Status and Perspectives. *J. Adv. Dielectr.* **2013**, *03* (02), 1330002.

(20) Yang, Z.; Du, H.; Jin, L.; Poelman, D. High-Performance Lead-Free Bulk Ceramics for Electrical Energy Storage Applications: Design Strategies and Challenges. *J. Mater. Chem. A* **2021**, *9* (34), 18026–18085.

(21) Wang, K.; Li, J.-F. Domain Engineering of Lead-Free Li-Modified $(K,Na)NbO_3$ Polycrystals with Highly Enhanced Piezoelectricity. *Adv. Funct. Mater.* **2010**, *20* (12), 1924–1929.

(22) Lv, X.; Zhu, J.; Xiao, D.; Zhang, X.-X.; Wu, J. Emerging New Phase Boundary in Potassium Sodium-Niobate Based Ceramics. *Chem. Soc. Rev.* **2020**, *49* (3), 671–707.

(23) Rodgers, J. A.; Williams, A. J.; Paul Attfield, J. High-Pressure / High-Temperature Synthesis of Transition Metal Oxide Perovskites. *Z. Naturforsch. B* **2006**, *61* (12), 1515–1526.

(24) Belik, A. A.; Yi, W. High-Pressure Synthesis, Crystal Chemistry and Physics of Perovskites with Small Cations at the A Site. *J. Phys.: Condens. Matter* **2014**, *26* (16), 163201.

(25) Gilioli, E.; Ehm, L. High Pressure and Multiferroics Materials: A Happy Marriage. *IUCrJ* **2014**, *1* (Pt 6), 590–603.

(26) Sleight, A. W.; Prewitt, C. T. Preparation of $CuNbO_3$ and $CuTaO_3$ at High Pressure. *Mater. Res. Bull.* **1970**, *5* (3), 207–211.

(27) Funamori, N.; Yagi, T.; Miyajima, N.; Fujino, K. Transformation in Garnet from Orthorhombic Perovskite to $LiNbO_3$ Phase on Release of Pressure. *Science* **1997**, *275* (5299), 513–515.

(28) Inaguma, Y.; Aimi, A.; Shirako, Y.; Sakurai, D.; Mori, D.; Kojitani, H.; Akaogi, M.; Nakayama, M. High-Pressure Synthesis, Crystal Structure, and Phase Stability Relations of a LiNbO3-Type Polar Titanate $ZnTiO_3$ and Its Reinforced Polarity by the Second-Order Jahn-Teller Effect. *J. Am. Chem. Soc.* **2014**, *136* (7), 2748–2756.

(29) Belik, A. A.; Stefanovich, S. Y.; Lazoryak, B. I.; Takayama-Muromachi, E. $BiInO_3$: A Polar Oxide with GdFeO3-Type Perovskite Structure. *Chem. Mater.* **2006**, *18* (7), 1964–1968.

(30) Aimi, A.; Mori, D.; Hiraki, K.-I.; Takahashi, T.; Shan, Y. J.; Shirako, Y.; Zhou, J.; Inaguma, Y. High-Pressure Synthesis of A-Site Ordered Double Perovskite $CaMnTi_2O_6$ and Ferroelectricity Driven by Coupling of A-Site Ordering and the Second-Order Jahn–Teller Effect. *Chem. Mater.* **2014**, *26* (8), 2601–2608.

(31) Ramirez, A. P.; Subramanian, M. A.; Gardel, M.; Blumberg, G.; Li, D.; Vogt, T.; Shapiro, S. M. Giant Dielectric Constant Response in a Copper-Titanate. *Solid State Commun.* **2000**, *115* (5), 217–220.

(32) Renner, B.; Lunkenheimer, P.; Schetter, M.; Loidl, A.; Reller, A.; Ebbinghaus, S. G. Dielectric Behavior of Copper Tantalum Oxide. *J. Appl. Phys.* **2004**, *96* (8), 4400–4404.

Chapter 2. Experimental and Computational Details

2.1 Sample Preparation

Polycrystalline samples of $CaMn(Ti_{1-x}V_x)_2O_6$, $CaZnV_2O_6$, $CuTaO_3$, and $CuNbO_3$ were prepared by high-pressure and high-temperature methods. Stoichiometric amounts of starting materials, $CaTiO_3$, $MnTiO_3$, Mn_2O_3, and V_2O_3 for $CaMn(Ti_{1-x}V_x)_2O_6$ with $x \leq 0.5$, $Ca_2V_2O_7$, $CaTiO_3$, $MnTiO_3$, MnO, and V_2O_3 for $CaMn(Ti_{1-x}V_x)_2O_6$ with $x \geq 0.6$, $Ca_2V_2O_7$, ZnO, and V_2O_5 for $CaZnV_2O_6$, Cu_2O and Ta_2O_5 for $CuTaO_3$, and Cu_2O and Nb_2O_5 for $CuNbO_3$, respectively were mixed carefully. Each mixed powder was put into a Pt capsule within a high-pressure cell and treated at 6 GPa and 1473 K for 30 min for $CaMn(Ti_{1-x}V_x)_2O_6$, 12 GPa and 1473 K for 30 min for $CaZnV_2O_6$, 6−12 GPa and 1273 K for and 30 min for $CuNbO_3$, and 6−12 GPa and 1273 K for 30 min for $CuNbO_3$, followed by a rapid temperature quench and then a gradual pressure release. On the other hand, perovskite-type of $CuTa_2O_6$ and $CuNb_2O_6$ were synthesized at ambient pressure. High-pressure synthesized $CuTaO_3$ and $CuNbO_3$ were annealed in the air at 773 K for 16 h, forming CuO and $CuTa_2O_6$, and CuO and $CuNb_2O_6$, respectively. The post-annealed samples were washed with concentrated hydrochloric acid. $CuTa_2O_6$ was also synthesized by the conventional solid-state reaction, as previously reported.[1] The 1.06 : 1 mixture of CuO and Ta_2O_5 was sintered at 1298 K for 24 h, followed by a quench in a water bath.

2.2 Sample Characterizations

X-ray diffraction (XRD) patterns were recorded using RINT-2000 (RIGAKU) or D8 advance (Bruker) equipped with Cu Kα radiation. Synchrotron XRD (SXRD) patterns were collected at various temperatures on the BL02B2 and BL19B2 beamlines at SPring-8. The powder samples were loaded into Lindemann glass or quartz glass capillaries. Neutron powder diffraction (NPD) data were collected at room temperature on the D2B instrument at the Institut Laue-Langevin, Grenoble, with a sample powder encased in a vanadium can. The lattice parameters and atomic coordination were refined by Le Bail or Rietveld analysis using RIETAN-FP,[2] FullProf,[3] or JANA2006.[4] The crystal structures were drawn by the program VESTA.[5]

Powder optical second harmonic generation (SHG) measurements at room temperature were performed using a pulsed Ti:sapphire laser (pulse width, 120 fs; repetition rate, 1 kHz; photon energy, 1.58 eV) or a pulsed Nd:YAG laser (pulse width, 25 ps; repetition rate, 10 Hz, photon energy 2.33 eV) as a light source. The samples were irradiated with the pulse, and a generated SHG pulse of 3.16eV or 4.66 eV was detected by photomultipliers. Electron diffraction (ED) patterns and bright-field images were taken from (quasi-)single-crystal domains at room temperature using a JEM-ARM200F (JEOL) TEM. Scanning transmitting electron microscopy (STEM) observations were conducted with the TEM equipped with an energy-dispersive X-ray (EDX) spectrometer. The probe-forming semi-angle for STEM was around 25 mrad. High-angle annular dark-field (HAADF) images were acquired with an inner collection angle of 68 mrad.

Hard X-ray photoemission spectroscopy (HAXPES) measurements were carried out to evaluate the valence state of cations at the BL46XU beamline at SPring-8. The polycrystalline sintered body samples were fractured in the Ar-filled glove box. The binding energy was calibrated by the peak position of Au $4f_{7/2}$ peak (84.0 eV) and the Fermi edge of a gold film sample. Cu and Nb K-edge extended X-ray absorption fine structure (XANES) spectra were measured in the transmission mode on the BL14B2 beamline at SPring-8. The cation ratio within the sample was determined by an Inductively coupled plasma optical emission spectrometer (ICP−OES) on SPECTROBLUE (SPECTRO). Thermogravimetry-differential thermal analysis TG–DTA was carried out using TG8210 (RIGAKU) upon heating at a rate of 5 K min^{-1}. The magnetic susceptibility data were collected using a superconducting quantum interference device magnetometer MPMS (Quantum Design) under an applied field of 100 Oe. The specific heat was measured using PPMS (Quantum Design). Frequency- and temperature-dependent complex dielectric constant and loss tangent were measured for pelletized samples with a frequency response analyzer, 4192A LF (Hewlett-Packard) or SI-1260 (Solatron).

2.3 Computational Methods

Electronic and crystal structures of $CuNbO_3$ and $LiNbO_3$ were calculated by Dr. Murata within the framework of density functional theory using the projector augmented-wave (PAW) method[6] implemented in the Vienna ab-initio simulation package (VASP) code.[7–9] The cut-off energy of plane waves was set to 600 eV. The k-points sampling was performed by Γ-centered Monkhorst−Pack[10] 4×4×3, 4×4×4, and

6×6×6 meshes for Pc perovskite-type and $R3c$ $LiNbO_3$-type $CuNbO_3$ and Cu_2O, respectively. The exchange–correlational functional was evaluated with the PBEsol functional.[11] The effect of Hubbard U was considered using Dudarev's approach.[12] The effective on-site Coulomb term, U_{eff}, was set at 3 eV. The initial electronic configurations for PAW potentials were $3s^2 3p^6 3d^{10} 4s^1$, $1s^2 2s^1$,$4s^2 4p^6 5s^2 4d^3$, and $2s^2 2p^6$ for Cu, Li, Nb, and O, respectively. The crystal structures were fully optimized until residual forces and stresses were less than 1.0×10^{-4} and 1.0×10^{-3} eV Å^{-1}, respectively. Convergence tests were performed by comparing the results with more severe conditions, for example, 800 eV and two times denser k-meshes. I confirmed that total energies were converged within 3 meV atoms^{-1}.

Lattice dynamics calculations were performed by Parlinski-Li-Kawazoe method using phonopy code.[13–17] 2×2×2 rhombohedral supercell was used for $LiNbO_3$-type $CuNbO_3$. Cu K XANES calculations were performed with the full-potential linearized augmented plane wave plus local orbitals method and the PBEsol+U ($U_{\mathrm{eff}} = 3$ eV) functional available in the WIEN2kcode.[18,19] A core-hole was directly treated for final-state calculations. The cut-off parameter of the plane wave, $R_{\mathrm{MT}}K_{\mathrm{MAX}}$, was set to 6.0 bohr Ry$^{1/2}$. Calculated spectra were broadened by Lorenz functions with a natural width of Cu K shell.[20] To correct the calculated transition energies, the calculated Cu K XANES spectra in the present study were shifted by −29.0 eV, corresponding to a transition-energy difference between the theoretical and experimental Cu KXANES spectra for the reference material, Cu_2O.

2.4 References

(1) Ebbinghaus, S. G. Influence of Composition and Thermal Treatment on the Properties of $Cu_{2+x}Ta_4O_{12+\delta}$. *Prog. Solid State Chem.* **2007**, *35* (2), 421–431.

(2) Izumi, F.; Momma, K. Three-Dimensional Visualization in Powder Diffraction. *Solid State Phenom.* **2007**, *130*, 15–20.

(3) Rodríguez-Carvajal, J. Recent Advances in Magnetic Structure Determination by Neutron Powder Diffraction. *Physica B Condens. Matter* **1993**, *192* (1), 55–69.

(4) Petříček, V.; Dušek, M.; Palatinus, L. Crystallographic Computing System *JANA2006*: General features. *Z. Kristallogr.* **2014**, *229* (5), 345–352.

(5) Momma, K.; Izumi, F. *VESTA 3* for Three-Dimensional Visualization of Crystal, Volumetric and Morphology Data. *J. Appl. Crystallogr.* **2011**, *44* (6), 1272–1276.

(6) Blöchl, P. E. Projector Augmented-Wave Method. *Phys. Rev. B Condens. Matter* **1994**, *50* (24), 17953–17979.

(7) Kresse, G.; Hafner, J. Ab Initio Molecular Dynamics for Open-Shell Transition Metals. *Phys. Rev. B Condens. Matter* **1993**, *48* (17), 13115–13118.

(8) Kresse, G.; Furthmüller, J. Efficient Iterative Schemes for Ab Initio Total-Energy Calculations Using a Plane-Wave Basis Set. *Phys. Rev. B Condens. Matter* **1996**, *54* (16), 11169–11186.

(9) Kresse, G.; Joubert, D. From Ultrasoft Pseudopotentials to the Projector Augmented-Wave Method. *Phys. Rev. B Condens. Matter* **1999**, *59* (3), 1758–1775.

(10) Monkhorst, H. J.; Pack, J. D. Special Points for Brillouin-Zone Integrations. *Phys. Rev. B Condens. Matter* **1976**, *13* (12), 5188–5192.

(11) Perdew, J. P.; Ruzsinszky, A.; Csonka, G. I.; Vydrov, O. A.; Scuseria, G. E.; Constantin, L. A.; Zhou, X.; Burke, K. Restoring the Density-Gradient Expansion for Exchange in Solids and Surfaces. *Phys. Rev. Lett.* **2008**, *100* (13), 136406.

(12) Dudarev, S. L.; Botton, G. A.; Savrasov, S. Y.; Humphreys, C. J.; Sutton, A. P. Electron-Energy-Loss Spectra and the Structural Stability of Nickel Oxide: An LSDA+U Study. *Phys. Rev. B Condens. Matter* **1998**, *57* (3), 1505–1509.

(13) Togo, A.; Oba, F.; Tanaka, I. Transition Pathway of CO_2 Crystals under High Pressures. *Phys. Rev. B Condens. Matter* **2008**, *77* (18), 184101.

(14) Togo, A.; Oba, F.; Tanaka, I. First-Principles Calculations of the Ferroelastic Transition between Rutile-Type and $CaCl_2$-Type SiO_2 at High Pressures. *Phys. Rev. B* **2008**, *78* (13), 134106.

(15) Togo, A.; Tanaka, I. Evolution of Crystal Structures in Metallic Elements. *Phys. Rev. B* **2013**, *87* (18), 184104.

(16) Akamatsu, H.; Fujita, K.; Kuge, T.; Gupta, A. S.; Togo, A.; Lei, S.; Xue, F.; Stone, G.; Rondinelli, J. M.; Chen, L.-Q.; Tanaka, I.; Gopalan, V.; Tanaka, K. Inversion Symmetry Breaking by Oxygen Octahedral Rotations in the Ruddlesden-Popper NaRTiO4 Family. *Phys. Rev. Lett.* **2014**, *112* (18), 187602.

(17) Togo, A.; Tanaka, I. First Principles Phonon Calculations in Materials Science. *Scr. Mater.* **2015**, *108*, 1–5.

(18) Anisimov, V. I., VI; Solovyev, I. V., IV; Korotin, M. A.; Czyzyk, M. T.; Sawatzky, G. A. Density-Functional Theory and NiO Photoemission Spectra. *Phys. Rev. B* **1993**, *48* (23), 16929–16934.

(19) Schwarz, K.; Blaha, P.; Madsen, G. K. H. Electronic Structure Calculations of Solids Using the WIEN2k Package for Material Sciences. *Comput. Phys. Commun.* **2002**, *147* (1), 71–76.

(20) Krause, M. O.; Oliver, J. H. Natural Widths of Atomic K and L Levels, K α X - ray Lines and Several KLL Auger Lines. *J. Phys. Chem. Ref. Data* **1979**, *8* (2), 329–338.

Chapter 3. Enhanced Spontaneous Polarization by V^{4+} Substitution in $CaMnTi_2O_6$

*This work has already been published in *Inorg. Chem.* **2020**, *59* (16), 11749–11756. Reprinted with permission from "Fukuda, M.; Nishikubo, T.; Pan, Z.; Sakai, Y.; Zhang, M.-H.; Kawaguchi, S.; Yu, H.; Okimoto, Y.; Koshihara, S.-Y.; Itoh, M.; Rödel, J.; Azuma, M. Enhanced Spontaneous Polarization by V^{4+} Substitution in a Lead-Free Perovskite $CaMnTi_2O_6$. *Inorg. Chem.* **2020**, *59* (16), 11749–11756." Copyright 2020 American Chemical Society.

3.1 Introduction

The most commonly used ferroelectrics, such as $BaTiO_3$ and $Pb(Zr, Ti)O_3$ are called displacive type ferroelectrics because their spontaneous polarization (P_s) is achieved by polar distortions of particular ions, such as the second-order Jahn-Teller distortion of d^0 cations, Ti^{4+} or Nb^{5+}.[1–6] Recently, a tetragonal double perovskite-type $CaMnTi_2O_6$ has attracted much attention because it is an order-disorder type ferroelectric and thus potentially free from the size effects shared in displacive type ferroelectrics.[7–10] The A-site Ca^{2+} and Mn^{2+} in $CaMnTi_2O_6$ are ordered in a columnar manner and present three types of coordination: ten-coordinated Ca^{2+} (A-site), planar coordinated Mn^{2+} (A'-site), and tetrahedrally coordinated Mn^{2+} (A''-site). This kind of double perovskite-type oxides can therefore be discribed as $A_2A'A''B_4O_{12}$. In $CaMnTi_2O_6$ ($Ca_2MnMnTi_4O_{12}$), the displacements of planar coordinated Mn^{2+} and octahedrally coordinated Ti^{4+} along the c-direction contribute to the net spontaneous polarization. It has been shown by a DFT calculations that the planar coordinated Mn^{2+} spontaneously moved off the plane is stabilized by interaction with the oxygen neighbors.[9] In a paraelectric phase of $CaMnTi_2O_6$ (> 630 K), the planar-coordinated Mn^{2+} is displaced randomly, while in a ferroelectric phase, the cation is shifted to one direction, indicating that the paraelectric-ferroelectric transition is of the order-disorder type. In other words, the ferroelectric transition in $CaMnTi_2O_6$ is triggered by the ordering of Mn^{2+} positions.

$PbVO_3$ is a polar perovskite isostructural with $PbTiO_3$ but exhibits much larger spontaneous polarization due to the ordering of d_{xy} orbital of V^{4+} ion with d^1 electronic configuration, i.e., the first-order Jahn-Teller distortion.[11,12] The pyramidal VO_5 coordination lifts the degeneracy of t_{2g} orbitals, and the one d-electron of V^{4+} occupies the d_{xy} orbital lowered in energy. However, such a giant polarization of V^{4+}-containing compounds has only been reported in combination with Pb^{2+} or Bi^{3+}, having stereochemical activity of the $6s^2$ lone pair. For example, $BaTiO_3$ is a ferroelectric compound due to the second-order Jahn-Teller effect of Ti^{4+}, while $BaVO_3$ with the first-order Jahn-Teller active V^{4+} ion crystallizes in a cubic paraelectric structure, even though these two compounds exhibit similar tolerance factors.[13,14]

Herein, I attempted to enhance the spontaneous polarization of lead-free $CaMnTi_2O_6$ by partially substituting V^{4+} for Ti^{4+}. While the substitution of V^{4+} for Ti^{4+} in $BaTiO_3$ results in the disappearance of the polarization, the polar distortion is expected to be preserved and enhanced in $CaMnTi_2O_6$ because the polar structure is triggered by the ordering of planar coordinated Mn^{2+} ions. My study would present a new guideline for designing superior lead-free ferroelectric materials.

3.2. Results and Discussion

Figure 1a depicts SXRD patterns for $CaMn(Ti_{1-x}V_x)_2O_6$ (x = 0, 0.1, 0.2, 0.3, 0.4, 0.5, and 0.6) at room temperature. The patterns of V^{4+} substituted samples (x = 0.1–0.6) can be indexed with the tetragonal double perovskite $A_2A'A''B_4O_{12}$-type structure. With further increasing x, $CaMn_3V_4O_{12}$[15] appeared as a secondary phase, suggesting that this condition's solubility limit was at around $x = 0.6$. It is known that the polar $CaMnTi_2O_6$ (space group: $P4_2mc$) and a nonpolar $CaFeTi_2O_6$ (space group: $P4_2/nmc$) yield very similar XRD patterns. Therefore, the polar character of $CaMn(Ti_{0.4}V_{0.6})_2O_6$ (x =0.6) with the largest V^{4+} substitution was confirmed by an optical SHG measurement. As indicated by the red curve, quadratic to the incident laser power, the SHG signal was clearly observed from $CaMn(Ti_{0.4}V_{0.6})_2O_6$, strongly indicating noncentrosymmetric crystal structure (Figure 1b). Therefore, I deduced that all of $CaMn(Ti_{1-x}V_x)_2O_6$ (x = 0–0.6) adopt the same polar structures. Rietveld refinements of SXRD data were carried out assuming $P4_2mc$ $CaMnTi_2O_6$-type structure as initial models. The results of the fittings are displayed in Figures 2–8, and the refined structural parameters are listed in Table 1. The antisite disorder between Ca and Mn is suggested by my magnetic studies, as discussed later, but Ca and Mn cannot be distinguished by SXRD because of their close atomic numbers. Indeed, I performed the Rietveld refinements using the models with the antisite disordering of cations, such as $(Ca_{1-y}Mn_y)_2(Ca_{2y}Mn_{1-2y})Mn(Ti_{1-x}V_x)_4O_{12}$ and $(Ca_{1-y}Mn_y)_2Mn(Ca_{2y}Mn_{1-2y})(Ti_{1-x}V_x)_4O_{12}$, but they didn't improve the fittings and were not employed in the final refinements. In the refinements of some compositions, the B(O) values were fixed at 0.3 Å^2 concerning those in other compositions. The crystal structure of $CaMn(Ti_{1-x}V_x)_2O_6$ ($Ca_2MnMn(Ti_{1-x}V_x)_4O_{12}$) is depicted in Figure 9a. Figure 9b plots the lattice parameters (a, c, and $V^{1/3}$) as functions of x. The unit cell volume monotonously decreases with increasing x values, mainly because of the shrinkage of the BO_6 octahedra, as Ti^{4+} is substituted by smaller V^{4+}.

Next, I investigate the x value dependence of P_s. The black and red circles in Figure 10 present calculated total P_s values for the refined $CaMn(Ti_{1-x}V_x)_2O_6$ structures and those coming from B cations displacements, respectively, assuming the point charge model. The P_s value increases from $x = 0$ to 0.4, as I expected, and decreases with further increasing x values. The change in P_s is found to mainly result from the changing displacement of Ti^{4+}/V^{4+}. A clear P-E hysteresis curve at room temperature was observed for $x = 0$ as previously reported,[7] but $x = 0.2$ sample exhibited a large leakage current, hindering the measurement (Figure 11).

The upper and middle panels of Figure 12a and b depict temperature dependence of dielectric constant, ε', and loss tangent, $\tan\delta$, for $CaMn(Ti_{1-x}V_x)_2O_6$ with $x = 0$ and 0.2 at 1 MHz. One can clearly see the dielectric anomaly at 650 K for $x = 0$ and 610 K for $x = 0.2$, corresponding to the ferroelectric-paraelectric phase transition temperature, T_C, as previously reported in $CaMnTi_2O_6$.[7] Unfortunately, I could not obtain reliable dielectric data for $x = 0.4$ and 0.6 because of their large leakage currents.

Another approach to determine the phase transition temperature, high-temperature SXRD experiment was therefore performed. The temperature dependence of the lattice parameters (bottom panels of Figure 12a and b) reveals that the c length decreases on heating below T_C and increases above T_C. In the ferroelectric structure ($< T_C$), the unit cell is elongated along the polar c axis due to the polar distortion. Such enhancement of the c-axis length becomes tiny as the temperature approaches T_C. On the other hand, in the paraelectric phase ($> T_C$), the c-axis length increases because of the normal thermal expansion. A slight difference was observed between the anomalies in dielectric permittivity and the c-lattice parameter of $x = 0.2$ sample. This is because of the coexistence of thermal expansion in the former.

The T_C of $x = 0.4$ was estimated to be 450 K, which is the inflection temperature of the c-lattice parameter (Figure 13a). On the other hand, the change in the c-lattice parameter is not evident in the $x = 0.6$ sample between 300 and 700 K (Figure 13b), but since the polar character at room temperature is confirmed by SHG measurement (Figure 1b), T_C of $x = 0.6$ would be slightly higher than room temperature. Thus, I found that T_C decreases as x increases. It seems contradictory that P_s increases while T_C decreases with increasing x values. This counterintuitive result will be discussed later.

Figure 14a features the temperature dependence of the magnetic susceptibility, $M H^{-1} = \chi(T)$ of $\mathrm{CaMn(Ti_{1-x}V_x)_2O_6}$ ($x = 0, 0.2, 0.4$, and 0.6) measured in a magnetic field of 100 Oe after zero-field cooling. They all show antiferromagnetic transitions at similar temperatures ~10 K (see the inset in Figure 14a). In addition to the antiferromagnetic transition below 10 K, ferromagnetic-like behaviors were observed in $x = 0.4$ and 0.6 samples. However, I found they originate from a small amount of magnetic impurity not detectable in the SXRD measurement by carrying out specific heat measurements, as discussed later.

The fittings to the Curie-Weiss law were carried out at 100–300 K based on the following equation:

$$\chi(T) = \chi_0 + \frac{C}{T-\theta_\mathrm{W}},$$

where χ_0 is a temperature-independent term, C is the Curie constant, and θ_W is the Weiss temperature. The calculated C and θ_W values are plotted in Figure 14b. The negative θ_W values for all compositions imply the presence of antiferromagnetic interaction. The absolute values of θ_W drastically decrease between $x = 0.2$ and 0.4. The C values for $\mathrm{CaMn(Ti_{1-x}V_x)_2O_6}$ ($x = 0$ and 0.2) are close to the theoretical value for high spin $\mathrm{Mn^{2+}}$ (4.375), but drastically decrease for $x = 0.4$ and 0.6, even though the amount of magnetic ions increases with increasing x. These results suggest a considerable degree of antisite disorder between $\mathrm{Ca^{2+}}$ and $\mathrm{Mn^{2+}}$ in $x = 0.4$ and 0.6 samples. The decrease in C would be partially because ferromagnetic impurities at low temperatures (described below) hinder the calculation of C. Still, it would also be due to charge transfer between $\mathrm{Mn^{2+}}$ and $\mathrm{V^{4+}}$, as detected by HAXPES measurements.

Figure 15 present HAXPES spectra of Mn 3s and V2p for $\mathrm{CaMn(Ti_{1-x}V_x)_2O_6}$ ($x = 0.2, 0.4$, and 0.6). It has been reported that the oxidation state of Mn can be determined from the magnitude of the two Mn 3s peaks splitting,[16] unfortunately, that is not clear in the present case. On the other hand, the valence state change of V was clearly confirmed by fitting the V 2p data. Backgrounds were subtracted using the Tougaard method during the fitting. Since the peak intensity of V 2p for $\mathrm{CaMn(Ti_{1-x}V_x)_2O_6}$ was too weak to perform the two Gaussian fitting, including the small contribution from $\mathrm{V^{3+}}$, the fitting was performed based on a single Gaussian peak, assuming only the $\mathrm{V^{4+}}$ contribution, as shown in the inset in Figure 15. The obtained full width at half maximum, FWHM values are 2.17(3) eV, 2.35(5) eV, and 2.55(2) eV for $x = 0.2, 0.4$, and 0.6, respectively. This result is consistent with an increased fraction of $\mathrm{V^{3+}}$ due to charge transfer between $\mathrm{Mn^{2+}}$ and $\mathrm{V^{4+}}$ with increasing x.

Figures 16a and b depict the temperature dependence of the specific heat, C_p, for $x = 0$ and 0.4. The λ-type peaks corresponding to the antiferromagnetic transitions at ~10 K are observed for both samples. On the other hand, no anomaly is found at 75 K for $x = 0.4$. Therefore, the ferromagnetic-like behaviors in x

= 0.4 and 0.6 are attributed to magnetic impurity phases. To further investigate the possibility of the above-mentioned antisite disorder, I estimated the magnetic entropy gained at the antiferromagnetic transition. The magnetic specific heat, C_{m}, was calculated by subtracting the lattice contribution, C_{l}, which was estimated by fitting the data below 60 K to the following equation:

$$C_{\mathrm{l}}(T) / T = \beta_1 T^2 + \beta_2 T^4$$

(Figures 16c-1 and d-1). The estimated values of C_{m} / T and ΔS for $x = 0$ and 0.4 are provided in Figures 8c-2, d-2. The obtained entropy for $x = 0$ (13.8 J mol^{-1} K^{-1}) is close to that for Mn^{2+} with $S = 5/2$ (14.9 J mol^{-1} K^{-1}), while the value for $x = 0.4$ (9.5 J mol^{-1} K^{-1}) is about 2/3. This also suggests that the antiferromagnetic ordering of $\mathrm{CaMn(Ti_{1-\mathit{x}}V_{\mathit{x}})_2O_6}$ with $x = 0.4$ is imperfect owing to the antisite disorder between Ca and Mn.

V^{4+} substitution for Ti^{4+} in $\mathrm{CaMnTi_2O_6}$ enhances the spontaneous polarization, P_{s}, because of the first-order Jahn-Teller distortion of V^{4+}. On the other hand, the phase transition temperature, T_{C}, decreases, seemingly contradicting the Landau theory relation $T_{\mathrm{C}} \propto \alpha^2$, where α is an order parameter.[17] Since most ferroelectrics are of the displacement type, their P_{s} values coincide with α. In such cases, an increase in P_{s} leads an increase in T_{C}. In the case of the order-disorder type ferroelectric $\mathrm{CaMn(Ti_{1-\mathit{x}}V_{\mathit{x}})_2O_6}$, this relation does not apply. Instead, T_{C} is proportional to the number of dipole moments, N. The mixing of the Ca^{2+} and Mn^{2+} and charge transfer between Mn^{2+} and V^{4+} decrease N, leading the decrease in T_{C}. Furthermore, the decreasing V^{4+} results in a smaller displacement of the B-site ($x \geq 0.5$). Indeed, similar suppression of T_{C} was reported for $\mathrm{Ca_{2-\mathit{x}}Mn_{\mathit{x}}Ti_2O_6}$ prepared by spark plasma synthesis at 100 MPa.[9] The T_{C} was reperted to decrease linearly with decreasing Mn^{2+} contents due to the introduction of Ca^{2+} into the Mn^{2+} sites. It was also suggested that the degree of ordering between Ca^{2+} and Mn^{2+} increases with increasing the synthesis pressure. Similarly, in the case of $\mathrm{CaMn(Ti_{1-\mathit{x}}V_{\mathit{x}})_2O_6}$, higher synthesis pressures would effectively induce the higher ordering and would result in higher T_{C}. In addition, $\mathrm{CaMn(Ti_{1-\mathit{x}}V_{\mathit{x}})_2O_6}$ with $x \geq 0.7$ might be obtained by preparing at higher pressure.

3.3 Summary of This Chapter

Structural evolution and dielectric and magnetic properties were investigated $CaMn(Ti_{1-x}V_x)_2O_6$ ($x = 0$–0.6) with the order-disorder type ferroelectric mechanism. I found that V^{4+} substitution with the forst-order Jahn-Teller activity enhanced P_s for $x \leq 0.4$. Antisite disorder between Ca^{2+} and Mn^{2+} as well as the intermetallic charge transfer between Mn^{2+} and V^{4+} was suggested by magnetic and HAXPES studies. Accordingly, P_s for $x \geq 0.5$ and T_C in all regions decreased. These findings indicate that introduction of V^{4+} is efficient to enhance the P_S of order-disorder type ferroelectrics.

3.4 Tables and Figures

Table 1. Structural Parameters for $\mathrm{CaMn(Ti_{1-x}V_x)_2O_6}$ (x = 0–0.6) at room temperature.

atoms	site	g	x	y	z	B / Å^2
			$x = 0^a$			
Ca1	2*a*	1	0	0	0	0.41(3)
Ca2	2*b*	1	1/2	1/2	0.0456(4)	= *B*(Ca1)
Mn1	2*c*	1	0	1/2	0.0699(4)	0.64(4)
Mn2	2*c*	1	0	1/2	0.5172(4)	0.90(4)
Ti1	8*f*	1	0.2572(2)	0.2459(2)	0.2769(5)	0.26(1)
O1	4*d*	1	0.2912(6)	0	0.8217(8)	0.24(3)
O2	4*d*	1	0.1869(7)	0	0.2278(8)	= *B*(O1)
O3	4*e*	1	0.3011(6)	1/2	0.2911(9)	= *B*(O1)
O4	4*e*	1	0.2096(7)	1/2	0.7095(9)	= *B*(O1)
O5	8*f*	1	0.1951(5)	0.2844(6)	0.0129(7)	= *B*(O1)
			$x = 0.1^b$			
Ca1	2*a*	1	0	0	0	0.30(3)
Ca2	2*b*	1	1/2	1/2	0.0468(4)	= *B*(Ca1)
Mn1	2*c*	1	0	1/2	0.0703(5)	0.35(4)
Mn2	2*c*	1	0	1/2	0.5188(5)	0.67(4)
Ti1	8*f*	0.9	0.2563(5)	0.2448(5)	0.2768(6)	0.26(1)
V1	8f	0.1				
O1	4*d*	1	0.2921(8)	0	0.8245(9)	0.3
O2	4*d*	1	0.1919(10)	0	0.2201(9)	= *B*(O1)
O3	4*e*	1	0.3103(9)	1/2	0.2926(10)	= *B*(O1)
O4	4*e*	1	0.2133(9)	1/2	0.7032(10)	= *B*(O1)
O5	8*f*	1	0.2028(22)	0.2961(22)	0.0170(8)	= *B*(O1)
			$x = 0.2^c$			
Ca1	2*a*	1	0	0	0	0.19(5)
Ca2	2*b*	1	1/2	1/2	0.0472(7)	= *B*(Ca1)
Mn1	2*c*	1	0	1/2	0.0778(6)	1.00(8)
Mn2	2*c*	1	0	1/2	0.5201(8)	0.93(8)
Ti1	8*f*	0.8	0.2550(4)	0.2443(4)	0.2904(7)	0.45(2)
V1	8f	0.2				
O1	4*d*	1	0.2906(10)	0	08229(13)	0.3
O2	4*d*	1	0.2053(13)	0	0.2246(14)	= *B*(O1)
O3	4*e*	1	0.3122(10)	1/2	0.2860(15)	= *B*(O1)
O4	4*e*	1	0.2208(12)	1/2	0.7148(16)	= *B*(O1)
O5	8*f*	1	0.1970(24)	0.3003(24)	0.02730(10)	= *B*(O1)
			$x = 0.3^d$			
Ca1	2*a*	1	0	0	0	0.51(3)

Ca2	2*b*	1	1/2	1/2	0.0478(5)	= *B*(Ca1)
Mn1	2*c*	1	0	1/2	0.0731(4)	0.61(4)
Mn2	2*c*	1	0	1/2	0.5195(6)	1.29(6)
Ti1	8*f*	0.3	0.2545(2)	0.2459(2)	0.2893(5)	0.26(1)
V1	8f	0.7				
O1	4*d*	1	0.2820(7)	0	0.8213(9)	0.19(3)
O2	4*d*	1	0.1993(9)	0	0.2219(8)	= *B*(O1)
O3	4*e*	1	0.3144(8)	1/2	0.2857(10)	= *B*(O1)
O4	4*e*	1	0.2095(8)	1/2	0.7073(10)	= *B*(O1)
O5	8*f*	1	0.2103(7)	0.3086(6)	0.0197(7)	= *B*(O1)
			x = 0.4[e]			
Ca1	2*a*	1	0	0	0	0.53(4)
Ca2	2*b*	1	1/2	1/2	0.0484(5)	= *B*(Ca1)
Mn1	2*c*	1	0	1/2	0.0686(5)	0.62(5)
Mn2	2*c*	1	0	1/2	0.5178(6)	1.55(7)
Ti1	8*f*	0.6	0.2534(2)	0.2459(2)	0.2917(5)	0.27(1)
V1	8f	0.4				
O1	4*d*	1	0.2856(8)	0	0.8264(10)	0.15(3)
O2	4*d*	1	0.1979(10)	0	0.2104(9)	= *B*(O1)
O3	4*e*	1	0.3220(8)	1/2	0.2816(10)	= *B*(O1)
O4	4*e*	1	0.2054(9)	1/2	0.7021(10)	= *B*(O1)
O5	8*f*	1	0.2085(11)	0.3008(10)	0.0205(7)	= *B*(O1)
			x = 0.5[f]			
Ca1	2*a*	1	0	0	0	1.27(5)
Ca2	2*b*	1	1/2	1/2	0.0491(7)	= *B*(Ca1)
Mn1	2*c*	1	0	1/2	0.0560(8)	0.43(5)
Mn2	2*c*	1	0	1/2	0.5228(10)	2.07(9)
Ti1	8*f*	0.5	0.2524(4)	0.2453(4)	0.2778(9)	0.65(2)
V1	8f	0.5				
O1	4*d*	1	0.2836(11)	0	0.8237(13)	0.35(3)
O2	4*d*	1	0.1962(11)	0	0.1980(12)	= *B*(O1)
O3	4*e*	1	0.31119(9)	1/2	0.2829(12)	= *B*(O1)
O4	4*e*	1	0.2132(12)	1/2	0.6939(15)	= *B*(O1)
O5	8*f*	1	0.2139(17)	0.2927(16)	0.0119(10)	= *B*(O1)
			x = 0.6[g]			
Ca1	2*a*	1	0	0	0	0.20(8)
Ca2	2*b*	1	1/2	1/2	0.0265(8)	= *B*(Ca1)
Mn1	2*c*	1	0	1/2	0.04334(8)	3.19(21)
Mn2	2*c*	1	0	1/2	0.5114(13)	0.96(13)
Ti1	8*f*	0.4	0.2479(4)	0.2446(4)	0.2727(7)	0.41(2)
V1	8f	0.6				
O1	4*d*	1	0.2883(20)	0	0.8267(15)	0.3
O2	4*d*	1	0.2054(19)	0	0.1927(15)	= *B*(O1)
O3	4*e*	1	0.3258(14)	1/2	0.2703(16)	= *B*(O1)

O4	4*e*	1	0.1985(24)	1/2	0.7172(15)	= *B*(O1)
O5	8*f*	1	0.2293(19)	0.2897(16)	0.0133(16)	= *B*(O1)

$^a a$ = 7.54607(1) Å, c = 7.59866(1)Å; R_{wp} = 6.215 % and R_{B} = 5.034 %.

$^b a$ = 7.54017(1) Å, c = 7.58728(2)Å, R_{wp} = 8.281 % and R_{B} = 6.936 %.

$^c a$ = 7.53576(1) Å, c = 7.58452(4)Å; R_{wp} = 2.762 % and R_{B} = 5.895 %.

$^d a$ = 7.53288(1) Å, c = 7.56382(3)Å; R_{wp} = 4.572 % and R_{B} = 4.023 %.

$^e a$ = 7.52846(1) Å, c = 7.54713(2)Å; R_{wp} = 4.726 % and R_{B} = 4.760 %.

$^f a$ = 7.51889(1) Å, c = 7.53160(3)Å; R_{wp} = 3.214 % and R_{B} = 2.726 %.

$^g a$ = 7.51271(2) Å, c = 7.51513(3)Å; R_{wp} = 5.243 % and R_{B} = 5.985 %.

$R_{\mathrm{wp}} = [\Sigma w_{\mathrm{i}}\,(y_{\mathrm{io}} - y_{\mathrm{ic}})^2 / \Sigma w_{\mathrm{i}} y_{\mathrm{io}}^2]^{1/2}$, where y_{io} and y_{ic} are the observed and calculated intensities, respectively, and w_{i} is the weighting factor. $R_{\mathrm{B}} = \Sigma|I_{\mathrm{o}}(h_K) - I_{\mathrm{c}}(h_K)| / \Sigma|I_{\mathrm{o}}(h_K)|$, where $I_{\mathrm{o}}(h_K)$ and $I_{\mathrm{c}}(h_K)$ are the observed and calculated integrated intensities for reflection K, respectively.

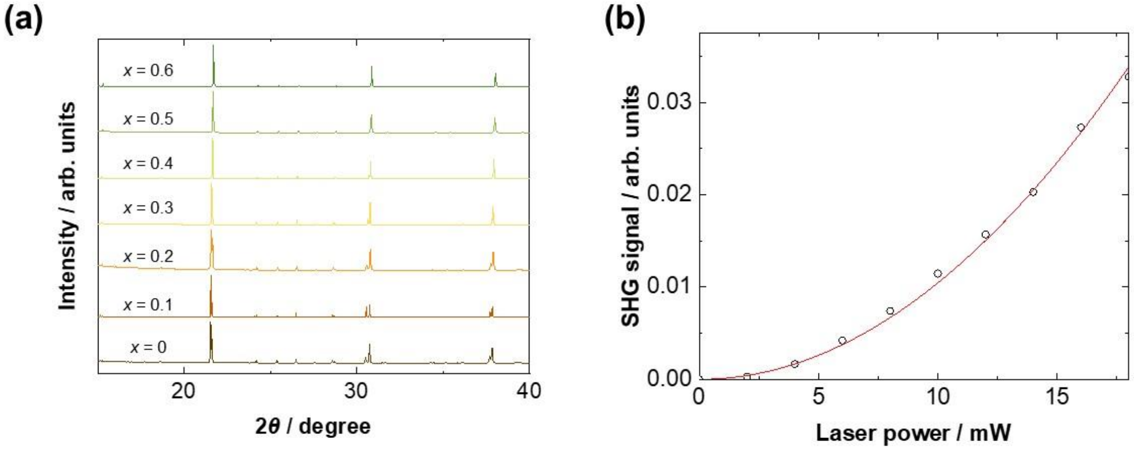

Figure 1. (a) SXRD patterns for $\mathrm{CaMn(Ti_{1-x}V_x)_2O_6}$ (x = 0, 0.1, 0.2, 0.3, 0.4, 0.5, and 0.6) at room temperature (λ = 0.99985 Å for x =0.2 and 0.99932 Å for others). The wavelengths were calibrated using a $\mathrm{CeO_2}$ standard. (b) Incident laser power dependence of SHG intensity for $\mathrm{CaMn(Ti_{0.4}V_{0.6})_2O_6}$, indicating the polar nature of the structure.

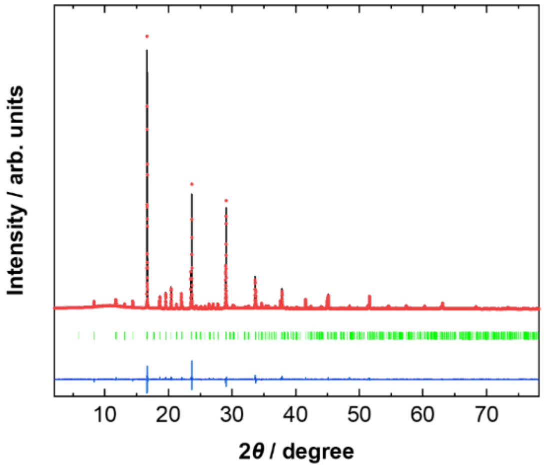

Figure 2. Results of Rietveld refinement against SXRD data (λ = 0.77435 Å) of $CaMnTi_2O_6$ at room temperature. The observed (red circles), calculated (solid black lines), and difference (blue bottom line) profiles are represented. The green ticks correspond to the positions of the allowed Bragg reflections.

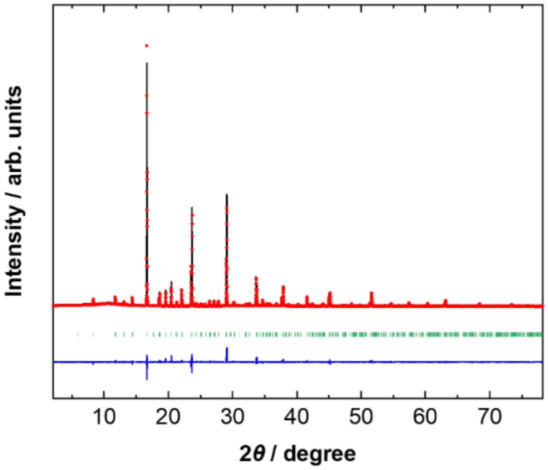

Figure 3. Results of Rietveld refinement against SXRD data (λ = 0.77435Å) of $CaMnTi_{1.8}V_{0.2}O_6$ at room temperature. The observed (red circles), calculated (solid black lines), and difference (blue bottom line) profiles are represented. The green ticks correspond to the positions of the allowed Bragg reflections.

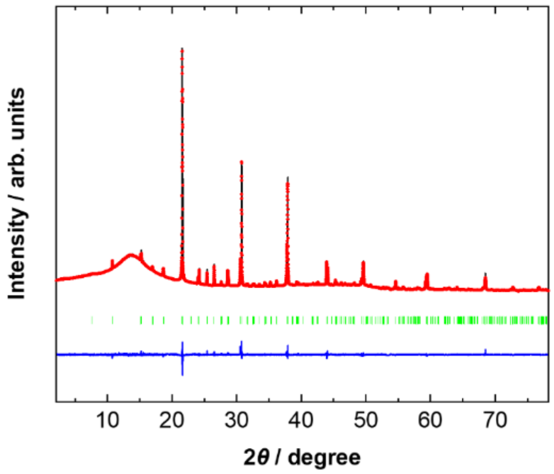

Figure 4. Results of Rietveld refinement against SXRD data (λ = 0.99985Å) of $CaMnTi_{1.6}V_{0.4}O_6$ at room temperature. The observed (red circles), calculated (solid black lines), and difference (blue bottom line) profiles are represented. The green ticks correspond to the positions of the allowed Bragg reflections.

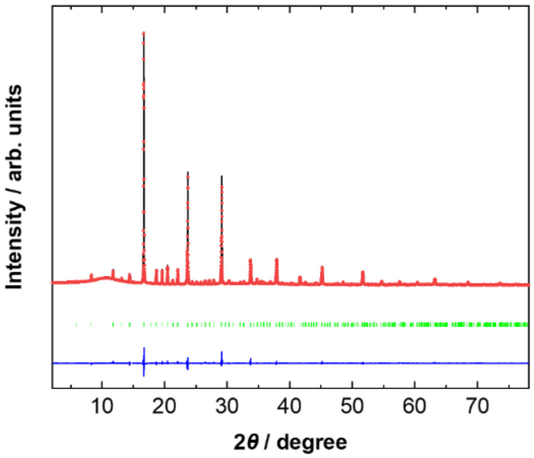

Figure 5. Results of Rietveld refinement against SXRD data (λ = 0.77435 Å) of $CaMnTi_{1.4}V_{0.6}O_6$ at room temperature. The observed (red circles), calculated (solid black lines), and difference (blue bottom line) profiles are represented. The green ticks correspond to the positions of the allowed Bragg reflections.

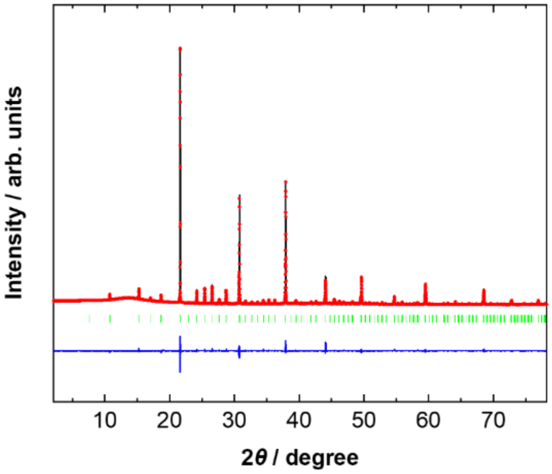

Figure 6. Results of Rietveld refinement against SXRD data (λ = 0.99932Å) of $CaMnTi_{1.2}V_{0.8}O_6$ at room temperature. The observed (red circles), calculated (solid black lines), and difference (blue bottom line) profiles are represented. The green ticks correspond to the positions of the allowed Bragg reflections.

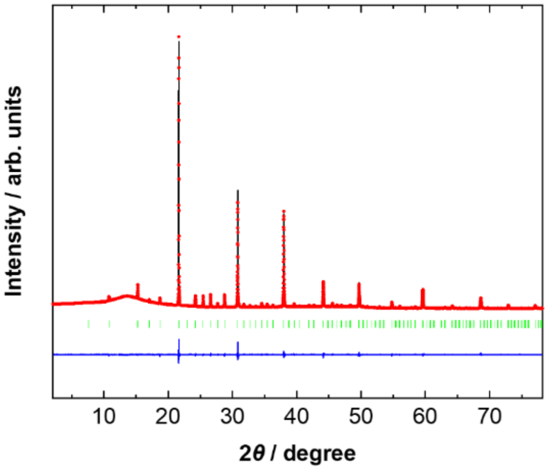

Figure 7. Results of Rietveld refinement against SXRD data (λ = 0.99932Å) of $CaMnTiVO_6$ at room temperature. The observed (red circles), calculated (solid black lines), and difference (blue bottom line) profiles are represented. The green ticks correspond to the positions of the allowed Bragg reflections.

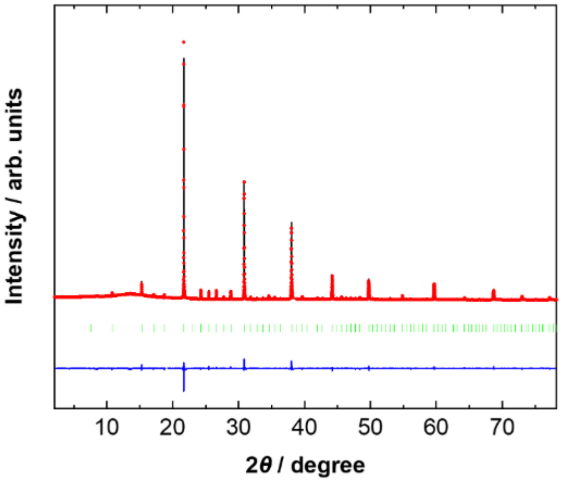

Figure 8. Results of Rietveld refinement against SXRD data (λ = 0.99932Å) of $CaMnTi_{0.8}V_{1.2}O_6$ at room temperature. The observed (red circles), calculated (solid black lines), and difference (blue bottom line) profiles are represented. The green ticks correspond to the positions of the allowed Bragg reflections.

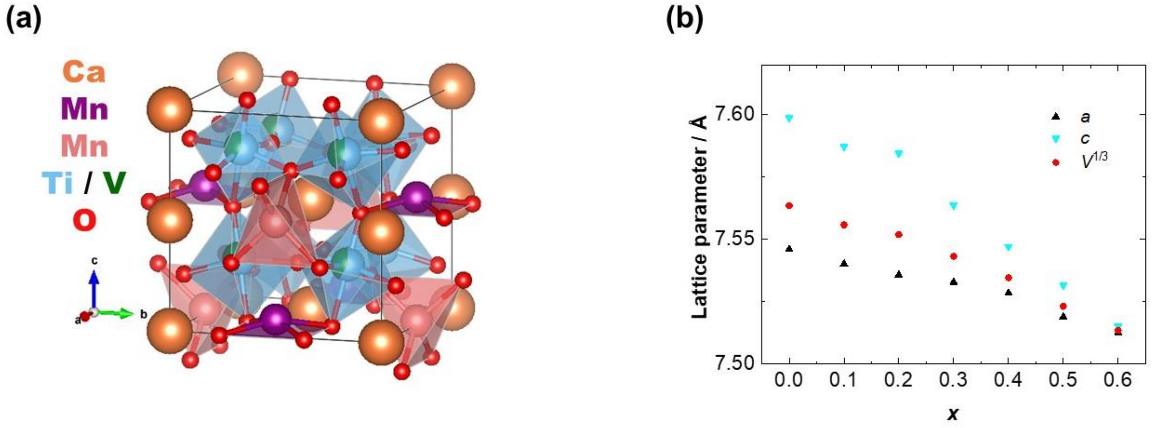

Figure 9. Evolutions of the structural parameters of $CaMn(Ti_{1-x}V_x)_2O_6$ (x = 0, 0.1, 0.2, 0.3, 0.4, 0.5, and 0.6. (a) Visualization of the crystal structure. (b) The x values dependence of (b) lattice parameters.

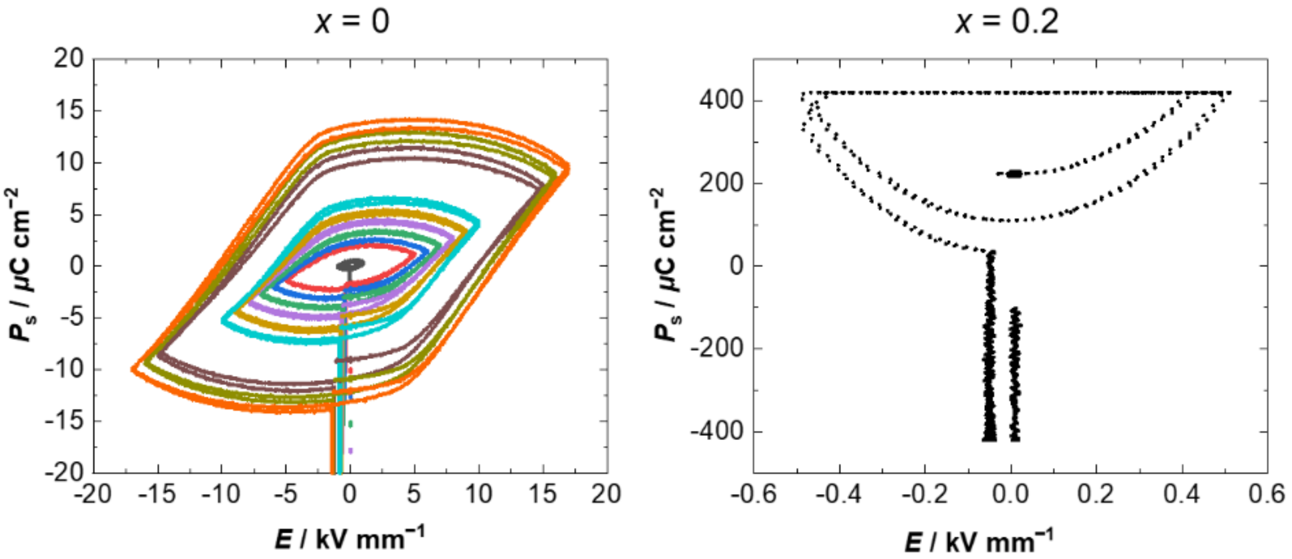

Figure 10. *P*-*E* curves measured on $x = 0$ and 0.2 samples at room temperature. The measurement frequency is 10 Hz.

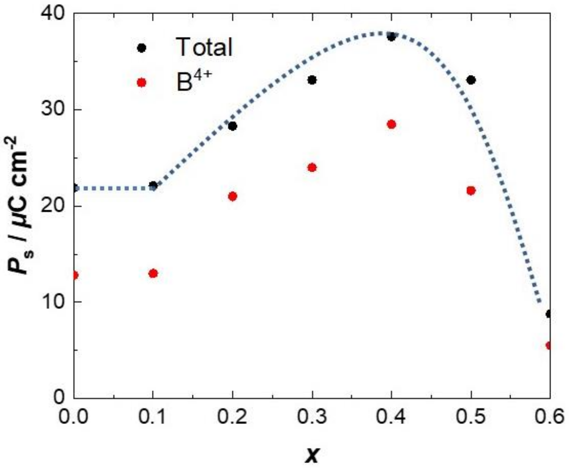

Figure 11. The calculated spontaneous polarization, P_s, as a function of x. The dotted line is a guide to the eye.

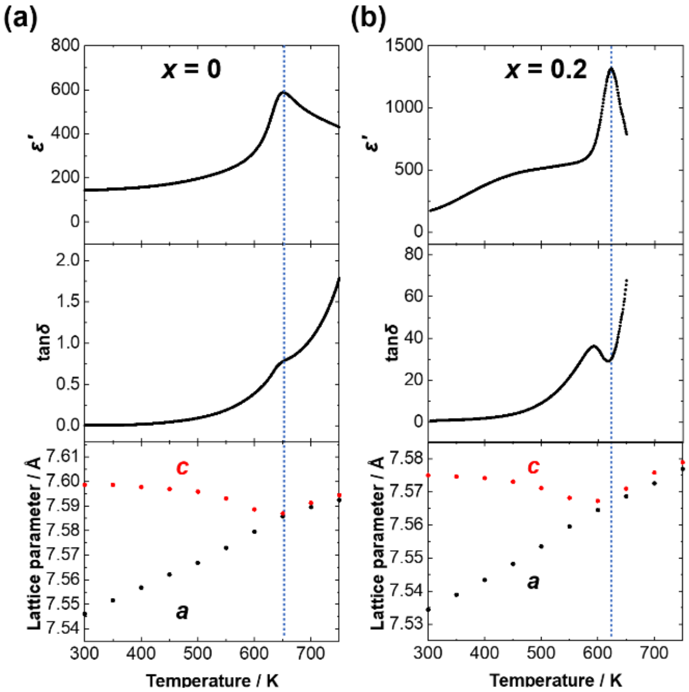

Figure 12. Determination of the Curie temperature, T_C of CaMn(Ti$_{1-x}$V$_x$)$_2$O$_6$ ($x = 0$ and 0.2) temperature dependence of relative permittivity ε' and loss tangent, tanδ at 1 MHz, and lattice parameters, *a* and *c* for (a) $x = 0$ and for (b) $x = 0.2$. The dotted lines correspond to T_C.

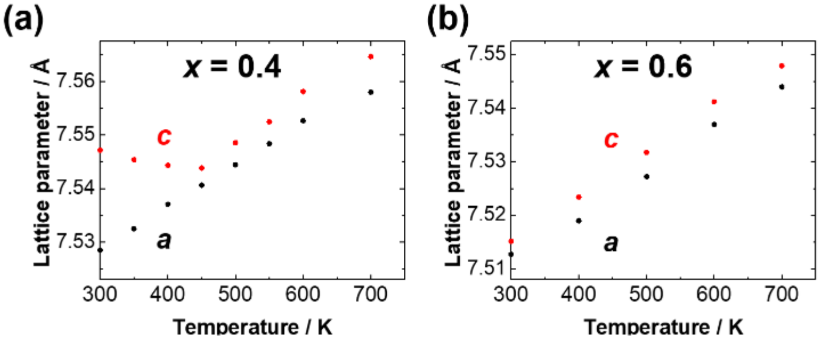

Figure 13. Temperature dependence of lattice parameters, *a* and *c* for CaMn(Ti$_{1-x}$V$_x$)$_2$O$_6$ with (a) $x = 0.4$ and (b) $x = 0.6$ revealing the phase transitions.

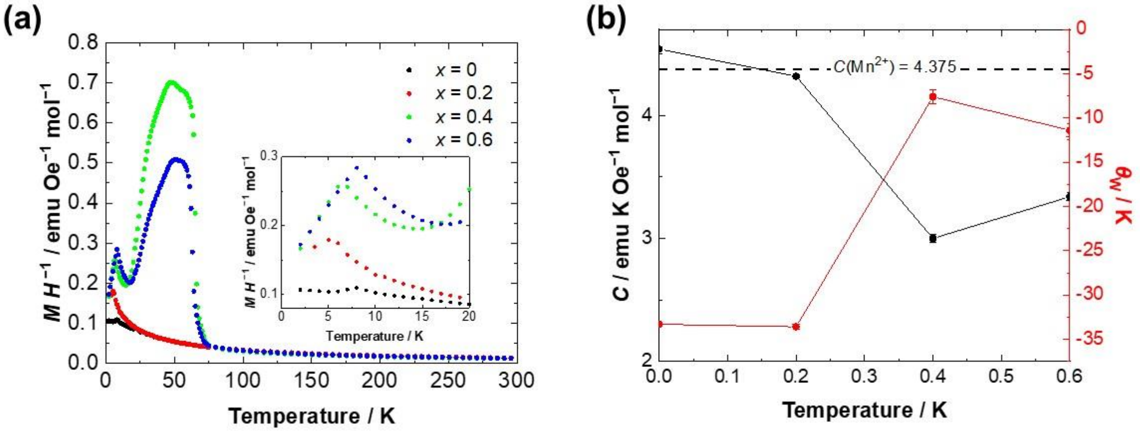

Figure 14. (a) Temperature dependence of magnetic susceptibility for CaMn$(Ti_{1-x}V_x)_2O_6$ (x = 0, 0.2, 0.4, and 0.6) measured at H = 100 Oe after zero-field cooling. The inset features a magnified view near the antiferromagnetic transition temperature. (b) The x value dependence of the Curie constant, C, and the Weiss temperature, θ_{W}.

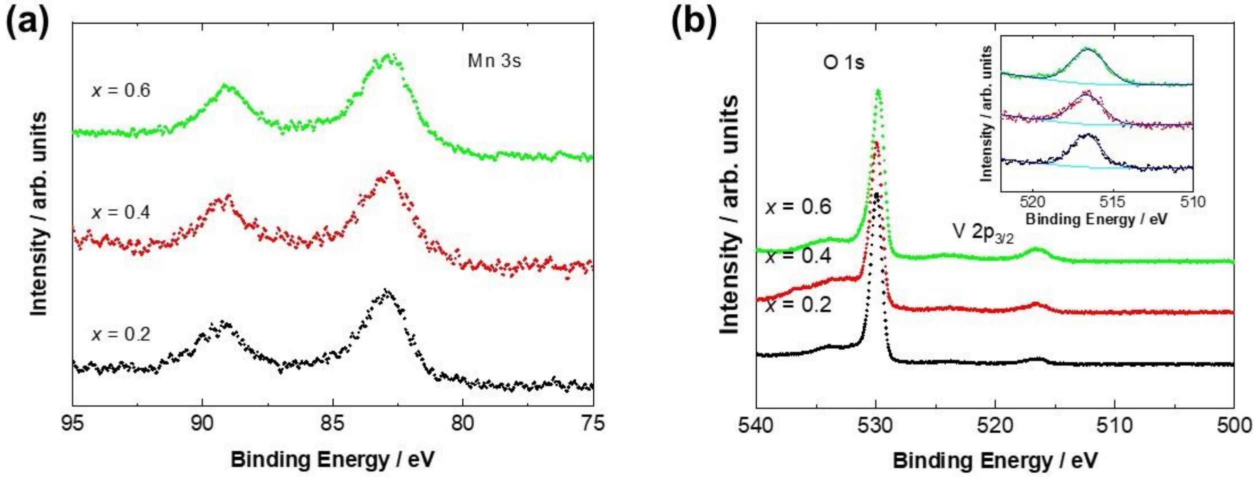

Figure 15. Observed HAXPES spectra of (a)Mn 3s and (b) O 1s and V 2p peaks. The inset in (b) shows fitting results using one Gaussian peak with backgrounds obtained by the Tougaard method.

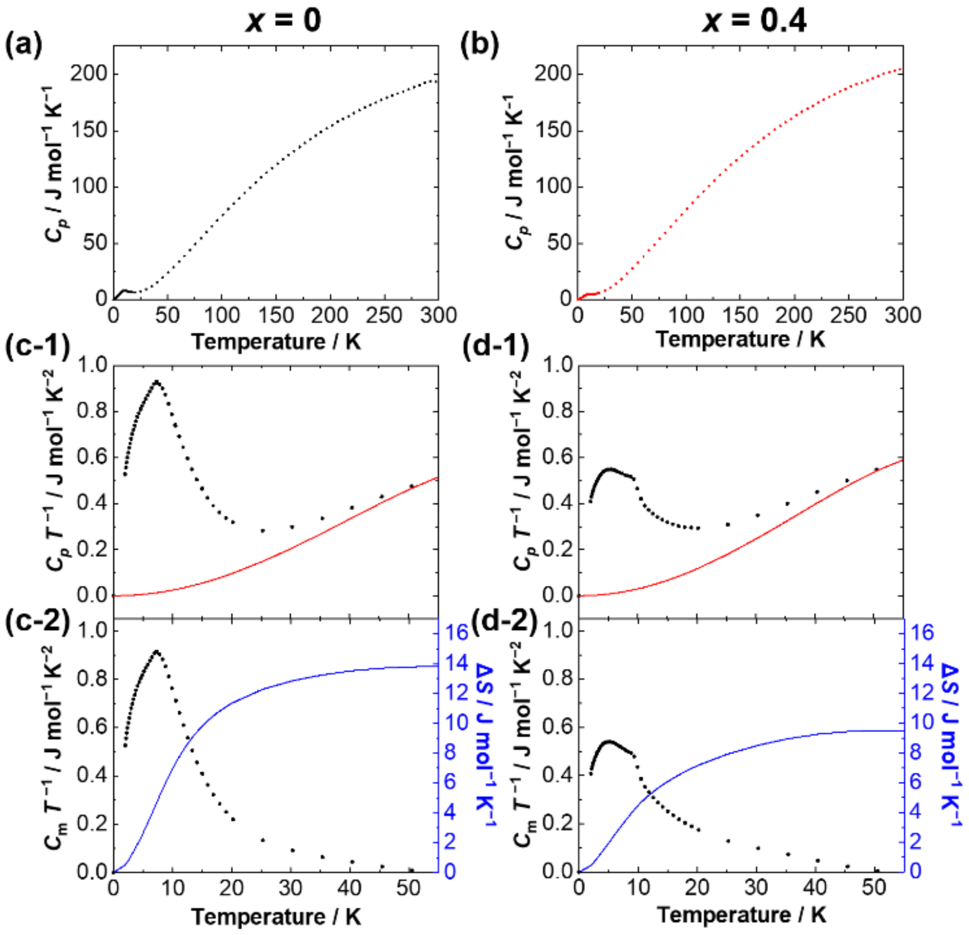

Figure 16. Temperature dependence of specific heat, C_p for CaMn(Ti$_{1-x}$V$_x$)$_2$O$_6$ with (a) $x = 0$ and (b) 0.4. The fitting results of the lattice specific heat for (c-1) $x = 0$ and (d-1) 0.4. The magnetic specific heat divided by temperature, $C_\mathrm{m} T^{-1}$ (dot lines) and the magnetic entropy (solid lines) for (c-2) $x = 0$ and (d-2) 0.4.

3.5 References

(1) Roberts, S. Dielectric and Piezoelectric Properties of Barium Titanate. *Phys. Rev.* **1947**, *71* (12), 890–895.

(2) von Hippel, A. Ferroelectricity, Domain Structure, and Phase Transitions of Barium Titanate. *Rev. Mod. Phys.* **1950**, *22* (3), 221–237.

(3) Cohen, R. E. Origin of Ferroelectricity in Perovskite Oxides. *Nature* **1992**, *358* (6382), 136–138.

(4) Kunz, M.; Brown, I. D. Out-of-Center Distortions around Octahedrally Coordinated D0 Transition Metals. *J. Solid State Chem.* **1995**, *115* (2), 395–406.

(5) Noheda, B.; Cox, D. E.; Shirane, G.; Gonzalo, J. A.; Cross, L. E.; Park, S.-E. A Monoclinic Ferroelectric Phase in the $Pb(Zr_{1-x}Ti_x)O3$ Solid Solution. *Appl. Phys. Lett.* **1999**, *74* (14), 2059–2061.

(6) Ok, K. M.; Halasyamani, P. S.; Casanova, D.; Llunell, M.; Alemany, P.; Alvarez, S. Distortions in Octahedrally Coordinated d^0 Transition Metal Oxides: A Continuous Symmetry Measures Approach. *Chem. Mater.* **2006**, *18* (14), 3176–3183.

(7) Aimi, A.; Mori, D.; Hiraki, K.-I.; Takahashi, T.; Shan, Y. J.; Shirako, Y.; Zhou, J.; Inaguma, Y. High-Pressure Synthesis of A-Site Ordered Double Perovskite $CaMnTi_2O_6$ and Ferroelectricity Driven by Coupling of A-Site Ordering and the Second-Order Jahn–Teller Effect. *Chem. Mater.* **2014**, *26* (8), 2601–2608.

(8) Gou, G.; Charles, N.; Shi, J.; Rondinelli, J. M. A-Site Ordered Double Perovskite $CaMnTi_2O_6$ as a Multifunctional Piezoelectric and Ferroelectric-Photovoltaic Material. *Inorg. Chem.* **2017**, *56* (19), 11854–11861.

(9) Li, Z.; Cho, Y.; Li, X.; Li, X.; Aimi, A.; Inaguma, Y.; Alonso, J. A.; Fernandez-Diaz, M. T.; Yan, J.; Downer, M. C.; Henkelman, G.; Goodenough, J. B.; Zhou, J. New Mechanism for Ferroelectricity in the Perovskite $Ca_{2-x}Mn_xTi_2O_6$ Synthesized by Spark Plasma Sintering. *J. Am. Chem. Soc.* **2018**, *140* (6), 2214–2220.

(10) Andryushin, N. D.; Zinenko, V. I.; Pavlovskii, M. S.; Shinkorenko, A. S. Calculation and Comparison of Electronic, Vibrational, Polarization, and Magnetic Properties of Double Perovskites $CaMnTi_2O_6$ and $CaFeTi_2O_6$. *J. Exp. Theor. Phys.* **2019**, *129* (6), 1036–1044.

(11) Belik, A. A.; Azuma, M.; Saito, T.; Shimakawa, Y.; Takano, M. Crystallographic Features and Tetragonal Phase Stability of $PbVO_3$, a New Member of $PbTiO_3$ Family. *Chem. Mater.* **2005**, *17* (2),

269–273.

(12) Oka, K.; Yamada, I.; Azuma, M.; Takeshita, S.; Satoh, K. H.; Koda, A.; Kadono, R.; Takano, M.; Shimakawa, Y. Magnetic Ground-State of Perovskite $PbVO_3$ with Large Tetragonal Distortion. *Inorg. Chem.* **2008**, *47* (16), 7355–7359.

(13) Nishimura, K.; Yamada, I.; Oka, K.; Shimakawa, Y.; Azuma, M. High-Pressure Synthesis of $BaVO_3$: A New Cubic Perovskite. *J. Phys. Chem. Solids* **2014**, *75* (6), 710–712.

(14) Bannikov, V. V. Elastic, Electronic and Magnetic Properties of New Oxide Perovskite $BaVO_3$: A First-Principles Study. *Mater. Chem. Phys.* **2016**, *171*, 119–125.

(15) Zhang, S.; Saito, T.; Mizumaki, M.; Chen, W.-T.; Tohyama, T.; Shimakawa, Y. Site-Selective Doping Effect in $AMn_3V_4O_{12}$ ($A = Na^+$, Ca^{2+}, and La^{3+}). *J. Am. Chem. Soc.* **2013**, *135* (16), 6056–6060.

(16) Biesinger, M. C.; Payne, B. P.; Grosvenor, A. P.; Lau, L. W. M.; Gerson, A. R.; Smart, R. S. C. Resolving Surface Chemical States in XPS Analysis of First Row Transition Metals, Oxides and Hydroxides: Cr, Mn, Fe, Co and Ni. *Appl. Surf. Sci.* **2011**, *257* (7), 2717–2730.

(17) Abrahams, S. C.; Kurtz, S. K.; Jamieson, P. B. Atomic Displacement Relationship to Curie Temperature and Spontaneous Polarization in Displacive Ferroelectrics. *Phys. Rev.* **1968**, *172* (2), 551–553.

Chapter 4. Noncollinear Ferrielectric to Collinear Ferroelectric Transition in $CuNbO_3$

*This work has already been published in *Chem. Mater.* **2020**, *32* (12), 5016–5027. Reprinted with permission from "Fukuda, M.; Yamada, I.; Murata, H.; Hojo, H.; Hernandez, O. J.; Ritter, C.; Tanaka, K.; Fujita, K. Perovskite-Type $CuNbO_3$ Exhibiting Unusual Noncollinear Ferrielectric to Collinear Ferroelectric Dipole Order Transition. *Chem. Mater.* **2020**, *32* (12), 5016–5027." Copyright 2020 American Chemical Society.

In this chapter, I report a perovskite oxide with a new type of polar structure, $CuNbO_3$, obtained by the high-pressure and high-temperature synthesis. My structural analysis reveals that $CuNbO_3$ perovskite crystallizes in a polar monoclinic space group (Pc), a subgroup of the polar rhombohedral space group $R3c$. This compound exhibits a "noncollinear ferrielectric" structure with parallel displacements of Cu^+ and antiparallel displacements of Nb^{5+} along different axes, representing a new type of polar phase in the perovskite structure. I also observe that the noncollinear ferrielectric Pc structure transforms around 470 K into the collinear ferroelectric $R3c$ structure that features parallel displacements of Cu^+ and Nb^{5+} in the same direction. The present work extends the accessible composition range of the perovskite niobate series and demonstrates the role of A–O covalency in determining their crystal structure.

4.1 Introduction

Perovskite niobates, $ANb^{5+}O_3$ (A = Li, Na, K, and Ag), are an important group of ferroelectric perovskites, exhibiting a wide variety of properties, including piezoelectricity, ferroelectricity, antiferroelectricity, and nonlinear optical effects.[1–3] Recently, they have also attracted much attention due to their excellent photocatalytic and photovoltaic properties as well.[4,5]

$KNbO_3$ is a ferroelectric with a tolerance factor, $t > 1$ ($t = 1.06$), showing B-site driven ferroelectricity as described in **1-1**.[6,7] In the room-temperature phase of $KNbO_3$, the second-order Jahn-Teller distortion[8–10] of $Nb^{5+}(4d^0)$ ions develops off-centering displacements along the pseudo-cubic $\langle 110 \rangle_{pc}$ axis in an orthorhombic polar phase (space group $Amm2$). $LiNbO_3$ is a compound with $t < 1$ ($t = 0.85$), exhibiting A-site driven polarization (see also **1-1**).[11–13]

Since the *t* values of $NaNbO_3$ ($t = 0.97$) and $AgNbO_3$ ($t = 0.97$) are slightly less than 1, the coexistence of the second-order Jahn-Teller Nb displacements and NbO_6 octahedral tilts provides complex crystal structures and phase diagrams.[14–18] The room-temperature phase of $NaNbO_3$ adopts an orthorhombic antiferroelectric structure (space group *Pbcm*), where the displacements of Nb^{5+} and Na^+ ions are ordered in an antiferroelectric way, and the dipole moments are totally canceled within the unit cell.[14] Despite the similar ionic radii (twelve-coordinated) of Ag^+ (1.37 Å) and Na^+ (1.39 Å), $AgNbO_3$ crystallizes into a slightly different phase from $NaNbO_3$. $AgNbO_3$ forms an orthorhombic ferroelectric structure (space group $Pmc2_1$).[18] The $Pmc2_1$ $AgNbO_3$ exhibits the same octahedral tilt system as the *Pbcm* $NaNbO_3$, but their cation displacements are ordered differently. In the case of $AgNbO_3$, both displacements of Ag^+ and Nb^{5+} ions are ordered in a ferrielectric way. The respective dipole moments are not completely canceled within the unit cell, providing a net polarization and weak ferroelectricity.[16,18] Note that the ordered dipole moments from the two cation displacements are collinear to the $<100>_{pc}$ axis. Namely, $AgNbO_3$ adopts a collinear ferrielectric structure. The formation of ferrielectric structure was ascribed to covalency of Ag–O bonds as well as that of Nb–O bonds; the covalent character arises from the Ag 4d–O 2p as well as the Nb 4d–O 2p orbital overlaps.[19] The Ag–O and Nb–O covalencies are also responsible for the visible photocatalytic properties of $AgNbO_3$.

Considering the functionality of perovskite niobates, extending their compositional space to other elements is important. In this study, Cu^+-including perovskite niobate, $CuNbO_3$, is targeted because of the expectation that the covalent *A*–O and *B*–O bonding due to Cu 3d–O 2p and Nb 4d–O 2p orbital overlaps would result in an unusual electric dipole order as in the case of $AgNbO_3$. However, although $ANbO_3$ (*A* = Li, Na, K, and Ag) can be synthesized under ambient conditions, $CuNbO_3$ is known to crystallize in a non-perovskite structure in such conditions; the ambient-pressure phase of $CuNbO_3$ (AP-$CuNbO_3$) adopts a $RbTaO_3$-type structure with a nonpolar monoclinic *C*2/*m* symmetry.[20,21] The $RbTaO_3$-type $CuNbO_3$ shows a corner- and edge-sharing NbO_6 lamellar linkage, in contrast to the perovskite structure with corner-sharing NbO_6 octahedra 3D network. The perovskite instability in $CuNbO_3$ is partly ascribed to the small Cu^+ ions on the *A*-sites, leading to a small *t* value ($t = 0.89$). The high-pressure synthesis allows me to isolate a polar $CuNbO_3$ (HP-$CuNbO_3$) perovskite, as previously reported. In 1970, Sleight *et al.* reported the synthesis of a monoclinic phase of $CuNbO_3$ at 6.5 GPa and 1273–1473 K, but the crystal structure was not solved, even no space group was unambiguously identified.[22]

Herein, I present a comprehensive structural characterization of the metastable perovskite phase of Pv-

$CuNbO_3$ using X-ray, neutron, and electron diffractions, an optical second harmonic generation, and first-principles lattice dynamics calculations. The results show that Pv-$CuNbO_3$ crystallizes in a monoclinic perovskite-type structure (space group *Pc*), featuring an unusual electric dipole order within a new type of polar phase in the perovskite structure. The perovskite-type *Pc* phase is a weakly polar material due to a "noncollinear ferrielectric" dipole order, i.e., a combination of almost parallel small displacements of Cu^+ ions along $[111]_{pc}$ with respect to the closed-packed oxygen subcell and almost antiparallel large off-centering displacements of Nb^{5+} ions along $<100>_{pc}$. I also observe that, upon heating to 470 K in ambient pressure, the weak polar *Pc* phase transforms into the strong polar *R*3*c* phase with parallel displacements of Cu^+ and Nb^{5+} ions. My results highlight that the bonding nature of *A*-site cations, as well as their ionic size, has a great impact on the electric dipole order in a small-tolerance-factor perovskite.

4.2 Results

4.2.1 Temperature-Induced Phase Transition

According to variable temperature SXRD experiments, I found temperature-induced phase transition in Pv-$CuNbO_3$ at 470 K. Figure 1 shows SXRD patterns of Pv-$CuNbO_3$ at 300 and 470 K upon heating under ambient pressure. At 470 K, the pattern agrees with the reflection conditions for the both of polar (*R*3*c*) and nonpolar ($R\bar{3}c$) phases of rhombohedral $LiNbO_3$-type structure ($-h + k + l = 3n$ for hkl, $h + l = 3n$ and $l = 2n$ for $h\bar{h}l$, $l = 3n$ for hhl, and $l = 6n$ for $00l$ in the hexagonal setting). Below 450 K, a symmetry lowering from the rhombohedral structure to a monoclinic structure is observed, accompanied by peak splittings (e.g., 012_h into 002_m and 110_m, and 110_h into 112_m and 020_m, where h and m represent hexagonal and monoclinic cells) and superlattice reflections (e.g., 012_m and 102_m). To the best of my knowledge, such a lower-symmetry phase of $LiNbO_3$-type has not been reported before.

First, to deduce the space group of the higher-temperature rhombohedral phase, I examined the temperature variation of the lattice parameters at 470–510 K, as done in $CaMn(Ti_{1-x}V_x)_2O_6$ (see **Chapter 3**), and found that the a_h increased with increasing temperature, while the temperature rise led to c_h decrease (Figure 2), where *h* represents a hexagonal setting. Similar behavior has been observed for *R*3*c* compounds, like $LiNbO_3$, $LiTaO_3$,[23] and $LiOsO_3$,[24] where the relaxation of the spontaneous ferroelectric strains along the polar *c* axis upon heating leads to a decrease of the c_h parameters and an increase of the a_h parameters; in the absence of spontaneous strains. The space group of the higher-temperature phase was hence determined as the polar $R3c$. I confirmed that there were only tiny changes in the Cu occupancies in the temperature region of the $R3c$ phase [g(Cu) = 0.929(9) at 470 K and 0.932(4) at 510 K], so Cu defect did not decrease c_h.

I fixed the Nb1 position at (0, 0, 0) in my crystal structure refinements. I refined the cation site occupancies to confirm the deviations from the stoichiometry and detected a small Cu defect (g(Cu)=0.929(9)). This nonstoichiometric composition model ($Cu_{0.93}NbO_3$) led to better overall fits than the stoichiometric composition model (R_{wp} = 7.91% and R_B = 7.11% for $Cu_{0.93}NbO_3$, and R_{wp} = 7.92% and R_B = 11.4% for $CuNbO_3$). The Cu deficiency is related to the onset of the decomposition of the $R3c$ phase driven by the release of A-site Cu, as mentioned later and is described in detail in the next chapter. The Rietveld plot of the $R3c$ $CuNbO_3$ at 470 K is shown in Figure 3(a). The refined structure is displayed in Figure 3(b), and the refined structural parameters are given in Table 1. The calculated spontaneous polarization along for $R3c$ $Cu_{0.93}NbO_3$ is 15 μC cm^{-2}, assuming the point charge model. Note that as explained later, in the lower-temperature phase, stoichiometric composition model was confirmed to be appropriate by various experiments. The temperature-induced phase transition almost concurs with the decomposition reaction of the $R3c$ phase, forming Cu_2O and $CuNb_2O_6$, according to the temperature-variable SXRD experiments. The former compound, Cu_2O, is formed by releasing A-site Cu in the $R3c$ phase and its subsequent oxidation by atmospheric oxygen. The latter compound, $CuNb_2O_6$, is described in the next chapter.

4.2.2 Crystal structure of Lower-Temperature Phase

Next, I analyze the crystal structure of the lower-temperature phase. ED was performed to deduce the crystal symmetry of Pv-$CuNbO_3$. Figure 4 shows the ED patterns at room temperature along the [001], [0$\bar{1}$0], and [100] zone axes. All reflections can be indexed with a monoclinic cell with $a \approx 5.5$ Å ($\approx \sqrt{2}a_{pc}$), $b \approx 5.2$ Å ($\approx \sqrt{2}a_{pc}$), $c \approx 7.7$ Å ($\approx 2a_{pc}$), and $\beta \approx 95°$, where pc means the pseudo-cubic unit cell. 120 reflection at [001] and 012 reflection at [100] (see red circles in Figure 1) were observed, indicating a primitive monoclinic unit cell. The absence of 00l reflections with l = odd in the [0$\bar{1}$0] pattern means the presence of the c-glide symmetry. Such a forbidden 001 reflection is observed along [100] due to multiple scattering effects. Given the 0k0 reflections with k = odd in the [001] and [100] zone axes, one will expect the absence of the 2_1 screw axis. However, when the multiple scattering effects are significant, the 010 reflections are observed even in the presence of the 2_1 screw axis. Namely, the presence or absence of the

2_1 screw axis cannot be determined by the ED analysis alone. Thus, ED results led to three possible space groups, Pc, $P2/c$, and $P2_1/c$.

SXRD patterns at 300−450 K can be indexed with the monoclinic unit cell with $a = \sqrt{2}a_{\mathrm{pc}}$, b = $\sqrt{2}a_{\mathrm{pc}}$, $c = 2a_{\mathrm{pc}}$, and $\beta \approx 95°$, in good agreement with the ED analysis. The pseudo-cubic lattice volumes, V_{pc}, of the lower-temperature monoclinic phase together with the higher temperature $R3c$ phases are plotted in Figure 5 against temperature. A continuous change in V_{pc} across the phase transition is found, indicative of a second-order phase transition. There are two space groups of monoclinic crystals, Pc and Cc, in subgroups of $R3c$, exhibiting a second-order phase transition. Based on the ED results and this group theory analysis, the space group of the low-symmetry phase is found to be Pc. The structural relationship between the Pc and $R3c$ phases is a maximal non-isomorphic group/subgroup with the following transformation matrix:

$$\begin{pmatrix} a_{\mathrm{m}} \\ b_{\mathrm{m}} \\ c_{\mathrm{m}} \end{pmatrix} = \begin{pmatrix} -1/3 & -2/3 & 1/3 \\ -1 & 0 & 0 \\ -2/3 & -4/3 & -1/3 \end{pmatrix} \begin{pmatrix} a_{\mathrm{h}} \\ b_{\mathrm{h}} \\ c_{\mathrm{h}} \end{pmatrix},$$

where a_{m}, b_{m}, and c_{m} are the lattice parameters of the monoclinic unit cell, and a_{h}, b_{h}, and c_{h} are the lattice parameters in the hexagonal setting of the rhombohedral $R3c$ unit cell. To the best of my knowledge, simple ABO_3 perovskites crystallizing in Pc with $a_{\mathrm{m}} \approx \sqrt{2}a_{\mathrm{pc}}$, $b_{\mathrm{m}} \approx \sqrt{2}a_{\mathrm{pc}}$, and $c_{\mathrm{m}} \approx 2a_{\mathrm{pc}}$ unit cell have not been discovered yet.

Next, I performed the crystal structure refinements using SXRD and NPD data at 300 K. The reflection conditions in the SXRD and NPD data agree with Pc. Rietveld refinements were performed against NPD and SXRD patterns of Pv-$CuNbO_3$ at 300 K by assuming as an initial model a Pc unit cell with a $\sqrt{2}a_{\mathrm{pc}} \times \sqrt{2}a_{\mathrm{pc}} \times 2a_{\mathrm{pc}}$ unit cell. The initial structural model was derived from the group-subgroup relationship with an $R3c$ ($LiNbO_3$-type) model using the program ISODISTORT of the ISOTROPY Software Suite,[25] and was confirmed by structure solution against the SXRD data by direct methods with EXPO2013.[26] I fixed the Nb1 position at (0, 0, 0). Figure 6a and b display the refinement results for SXRD and NPD data, respectively. In the SXRD data, the presences of heavy Nb and Cu atoms lead to a meager contribution of oxygen atoms. The B_{iso} values of oxygen atoms were accordingly fixed to the B_{iso} value of Nb2. The stoichiometric composition models provided good overall fits to the observed patterns for both SXRD (weighted profile R factor $R_{\mathrm{wp}} = 11.60$ % and Bragg R factor $R_{\mathrm{B}} = 6.62$ %) and NPD data ($R_{\mathrm{wp}} = 10.34$ % and $R_{\mathrm{B}} = 3.66$ %). The cation site occupancies were refined to check the deviations in the stoichiometry, but the refined occupancies remained within 1 or 2 % of the expected full site values. This result agrees with complementary ICP-OES analysis in which the cationic ratio is almost stoichiometric (Cu/Nb = 1.05) within standard uncertainties. I also examined the possibility of cation mixing in the *A*-site. According to the previous structural analyses on $LiNbO_3$, the cation distribution was estimated to be $(Li_{1-5x}Nb_x\square_{4x})NbO_3$, where □ represents a vacancy.[27,28] In the course of my refinements against SXRD and NPD data, the introduction of a small amount of Nb (a few percent) at the Cu1 or Cu2 sites did not improve the fitting quality. The refined structural parameters from SXRD and NPD data are listed in Table 2 and Table 3, respectively. The selected bond lengths and bond angles are tabulated in Table 4.

The calculated density of Pv-$CuNbO_3$ [6.12 g cm^{-3} (SXRD) and 6.14 g cm^{-3} (NPD)] is significantly larger than that of $RbTaO_3$-type $CuNbO_3$ (5.02 g cm^{-3}),[27] consistent with the expectation that the high-pressure synthesis provides a higher-density phase. Bond-valence-sum calculations[29] using the NPD-refined bond lengths give +0.93(3), +0.99(2), +4.85(7), and +4.84(8)) for Cu1, Cu2, Nb1, and Nb2, respectively, confirming the $Cu^{+}Nb^{5+}O_3$ ionic model. This result conforms to XANES and temperature-dependent magnetic susceptibility experiments, which will be separately described below. Figure 7a depicts the crystal structures of Pv-$CuNbO_3$ refined against the NPD data at 300 K. The monoclinic distortion of Pv-$CuNbO_3$ highlights the tilting distortion of NbO_6 octahedra and the off-center displacements of Nb^{5+} ions. The octahedral tilt system is $a^-a^-c^-$. Glazer has shown that applying this tilt system to an aristotype cubic $Pm\bar{3}m$ perovskite without the cation displacement results in a centrosymmetric monoclinic $C2/c$ structure.[30] In Pv-$CuNbO_3$ perovskite, the symmetry is further lowered to the space group *Pc* by the two inequivalent off-center displacements of Nb^{5+} ions (see arrows in Figure 7b).

In ABO_3 perovskite oxides, the decrease in the *A*-site ionic radius, i.e., the reduction in the tolerance factor *t*, results in enhanced octahedral tilting, leading to the decrease of the *B*−O−*B* bond angle. As expected from the small *t* value ($t = 0.89$), the *Pc* phase of Pv-$CuNbO_3$ possesses a considerable magnitude of NbO_6 octahedral tilts, with the Nb–O–Nb angles deviating significantly from the ideal value of 180° by up to ~36° (see Table 4). The Nb–O–Nb bond angles of Pv-$CuNbO_3$ (144–148°) are smaller than those of $NaNbO_3$ (157–162°),[31] but are larger than that of $LiNbO_3$ (140°).[11] Namely, the average Nb–O–Nb bond angle decreases in the order $NaNbO_3$ (t = 0.97) > $CuNbO_3$ (t = 0.89) > $LiNbO_3$ (t = 0.85), demonstrating the *A*-site-cation-size-dependent octahedral tilting. In *Pc* $CuNbO_3$, the coordination environments of the two independent Nb sites, Nb1 and Nb2, are strongly asymmetric due to their off-center displacements along [001] (=<100>$_{\mathrm{pc}}$) within the octahedra (see Figure 7b). The NbO_6 octahedral distortion Δ of Pv-$CuNbO_3$ was calculated from the NPD-refined bond lengths; $\Delta = 1/6\Sigma_i[(d_i-\langle d\rangle)/\langle d\rangle]^2$, where d_i is the individual Nb–O bond length and $\langle d\rangle$ is the average Nb–O bond length (see Table 4). I obtained $\Delta(Nb1O_6) = 1.5(2) \times 10^{-3}$ and $\Delta(Nb2O_6) = 2.9(1) \times 10^{-3}$.The magnitude of these octahedral distortions is comparable to that for other perovskite niobates, $ANbO_3$ with second-order Jahn–Teller active $Nb^{5+}(4d^0)$ ions (e.g., $3.11(1) \times 10^{-3}$ for $LiNbO_3$[11] and $4.0(3) \times 10^{-3}$ for $KNbO_3$[30]). The large octahedral distortions for Pv-$CuNbO_3$ are thus ascribed to the second-order Jahn–Teller effects.

Asymmetric environments are also observed for the Cu coordination in *Pc* $CuNbO_3$: Cu atoms are displaced approximately along $[20\bar{3}]$ (=[111]$_{\mathrm{pc}}$) with respect to the oxygen-triangle planes, occupying two independent Cu sites, Cu1 and Cu2 (see Figure 7b). Each of Cu1 and Cu2 atoms forms three shorter and nine longer bonds with the oxygen atoms (see also Table 4), although the *A*-site cations in aristotype perovskites are surrounded by 12 equidistant anions. The distances of the longer Cu–O bonds (2.64(3)–3.26(2) Å for Cu1 and 2.76(2)–3.20(2) Å for Cu2) are much larger than those of the shorter Cu–O bonds (2.01(3), 2.04(3), 2.08(1) Å for Cu1 and 2.00(1), 2.03(2), 2.03(2) Å for Cu2), and so the effective coordination number of Cu atoms is three. The coordination environments of $Cu1O_3$ and $Cu2O_3$ differ in terms of polyhedral distortions and average bond lengths. The displacement from the centers of oxygen triangles is about nine times larger for Cu1 than for Cu2 (see Figure 7b and Figure 11).

Interestingly, I notice that the perovskite-type Pv-$CuNbO_3$ has the same crystal symmetry and unit-cell metrics as the lowest-temperature monoclinic phase of WO_3, ε-WO_3.[32] Namely, both of them crystallize in *Pc* symmetry with $a_m \approx \sqrt{2}a_{\mathrm{pc}}$, $b_m \approx \sqrt{2}a_{\mathrm{pc}}$, and $c_m \approx 2a_{\mathrm{pc}}$. Note that the structure of WO_3 can be regarded as an ABO_3 perovskite-type structure with empty *A*-sites. In the *Pc* structure of Pv-$CuNbO_3$, the *B*1 and *B*2 atoms (*B* = Nb in Pv-$CuNbO_3$ or W in ε-WO_3) undergo almost antiparallel off-center displacements along [001] (=<100>$_{\mathrm{pc}}$) within the octahedra. For ε-WO_3, the antiparallel displacements of W1 and W2 atoms with different amplitudes produce “collinear ferrielectricity”. For Pv-$CuNbO_3$, the antiparallel displacements of Nb1 and Nb2 with different magnitudes are accompanied by the parallel displacements of Cu1 and Cu2 atoms approximately along $[20\bar{3}]$ (=[111]$_{\mathrm{pc}}$). Consequently, a noncollinear ferrrielectric structure appears in the *Pc* phase of Pv-$CuNbO_3$. The spontaneous polarization calculated from the NPD-refined crystal structure using the formal charges of Cu^+ and Nb^{5+} is 9.7 μC cm^{-2}, which is smaller than that of the higher-symmetry *R*3*c* $CuNbO_3$ at 470 K. The counterintuitive result is because that the almost antiparallel off-center displacements of Nb^{5+} ions in *Pc* $CuNbO_3$ cancel each other’s polarization, suppressing the net polarization. Such antiparallel displacements of Nb^{5+} along [001] would decrease with increasing temperature, leading to the fact that c_m decreases with increasing temperature (Figure 8). It is worth underlining that ferrielectricity is observed in $AgNbO_3$, but it stems from collinear electric dipole order. On the other hand, Pv-$CuNbO_3$ is a rare example of a ferrielectric material with noncollinear electric dipole order, representing a new type of polar phase in the perovskite structure.

4.2.3 Valence State

Figure 8a, b displays the experimental and calculated XANES spectra at the Cu K-edge, respectively. The experimental Cu absorption edge position of Pv-$CuNbO_3$ is close to that of Cu_2O, but different from that of CuO. The contrasting coordination environment between Pv-$CuNbO_3$ (triangular-coordination) and Cu_2O (linear coordination), however, makes it difficult to clearly estimate the Cu valency in Pv-$CuNbO_3$. So, XANES calculations were performed for Pv-$CuNbO_3$ as well as for a reference compound, Cu_2O (Figure 5b). The experimental spectra for Pv-$CuNbO_3$ and Cu_2O match qualitatively with the calculated spectra based on $Cu^+Nb^{5+}O_3$ and $Cu^+{}_2O$ models, respectively, revealing that the Cu cations are present as Cu^+ in both compounds. On the other hand, the Nb valency in Pv-$CuNbO_3$ (octahedral coordination) can be easily estimated to be +5 from the similarity of its experimental spectrum to that of Nb_2O_5 (octahedral coordination) (Figure 6). Thus, my XANES analyses unambiguously evidence that the valence states in $CuNbO_3$ are +1 for Cu and +5 for Nb.

Figure 9 gives the temperature dependence of magnetic susceptibility, $\chi(T)$, of Pv-$CuNbO_3$ measured at 100 Oe on heating after zero-field cooling. The fitting was done by the Curie−Weiss law described by the following equation:

$$\chi(T) = \chi_0 + \frac{C}{(T - \theta_{\mathrm{w}})},$$

where χ_0 is a temperature-independent term, C the Curie constant, and θ_{w} the Weiss temperature. The fitting results are $\chi_0 = -2.6(1) \times 10^{-4}$ emu Oe^{-1} mol^{-1}, $\theta_{\mathrm{w}} = -1.8(2)$ K, and $C = 1.13(5) \times 10^{-2}$ emu K Oe^{-1} mol^{-1}. The calculated Curie constant is significantly smaller than that for Cu^{2+} (0.375 emu K Oe^{-1} mol^{-1}). The paramagnetic behavior is thus attributed to a small amount of magnetic impurities. In addition, $\chi(T)$ is negative above 50 K, with the absolute values being larger than those of the container used for the measurement. These facts mean that Pv-$CuNbO_3$ is diamagnetic owing to the presence of closed-shell cations, $Cu^+(d^{10})$ and $Nb^{5+}(d^0)$.

4.3 Discussion

As described above, I found two new polar polymorphs of $CuNbO_3$. One is the monoclinic *Pc* perovskite-type phase (Pv-$CuNbO_3$) stabilized via the high-pressure and high-temperature synthesis, and the other is the rhombohedral *R*3*c* perovskite-type (or $LiNbO_3$-type) phase observed as the higher-temperature phase of the *Pc* phase. The former is the first example of a simple ABO_3 perovskite crystallizing in monoclinic *Pc* symmetry with $a \approx \sqrt{2}a_{pc}$, $b \approx \sqrt{2}a_{pc}$, and $c \approx 2a_{pc}$ unit cell. It also represents a rare example of a "noncollinear ferrielectric" dipole order. Here, it should be noted that, in contrast to the *Pc* phases, the higher-symmetry *R*3*c* phases have been often observed in ABO_3 compounds by the use of high-temperature and high-pressure conditions; examples include $CuTaO_3$,[31–33] $AFeO_3$ (A = Sc, Ga, and In),[33–35] $ATiO_3$ (A = Mg, Mn, Fe, Zn, and Hg),[36–42] $LiBO_3$ (B = Sb, W, and Os)[24,43,44], and so forth. To examine the stable structure of Pv-$CuNbO_3$, phonon calculations were performed using the parent *R*3*c* phase. The crystal structure was optimized in the *R*3*c* symmetry. Phonon dispersion curves for the *R*3*c* structure are depicted in Figure 12. One can see an imaginary mode at the F point. Within the framework of a second-order phase transition, freezing the F-point soft mode yields a monoclinic polar *Pc* structure with $a \approx \sqrt{2}a_{pc}$, $b \approx \sqrt{2}a_{pc}$, $c \approx 2a_{pc}$, and $\beta \approx 95°$, ascribed to the antiparallel off-center displacements of Nb^{5+} and the $a^-a^-c^-$-type tilts of NbO_6 octahedra. The calculations demonstrate that the *Pc* structure has lower energy than the *R*3*c* structure and is dynamically stable, consistent with the experimental observation that the low-temperature and high-temperature phases of Pv-$CuNbO_3$ crystallize in the space groups *Pc* and *R*3*c*, respectively.

It is worth emphasizing that Pv-$CuNbO_3$ (*Pc*) has a lower-symmetry structure than $LiNbO_3$ (*R*3*c*), despite the very close t values between $CuNbO_3$ ($t = 0.89$) and $LiNbO_3$ ($t = 0.85$). Comparing the crystal structure of $CuNbO_3$ and $LiNbO_3$ (see Figure 13) reveals that *A*-site cations (Cu^+ in $CuNbO_3$ and Li^+ in $LiNbO_3$) are displaced from the closed-packed oxygen planes along $[111]_{pc}$, but the Li displacements are much larger than the Cu displacements. While the large Li displacements in *R*3*c* $LiNbO_3$ lead to the formation of LiO_6 octahedra (see Figure 11b), the relatively small Cu displacements in Pv-$CuNbO_3$ confine the Cu–O bonds to three oxide ions forming triangles (see Figure 11a), i.e., Cu^+ ions are virtually three-coordinated in Pv-$CuNbO_3$. This may be explained by the difference in the bonding character between Li–O (ionic) and Cu–O (covalent).

To evaluate the comparatively of the bonding character for Pv-$CuNbO_3$ and $LiNbO_3$, their electronic structures were also calculated. In the calculations, the same $R3c$ structure used in the phonon calculations was utilized. Figure 14a and b depict the calculated total and partial density of states (DOS) for $R3c$ $CuNbO_3$ and $LiNbO_3$, respectively. For $CuNbO_3$, the valence band mainly consists of Cu 3d and O 2p states, and the conduction band is composed of the Nb 4d state. The Cu 3d state contributes to the formation of the top of the valence band through the orbital overlap with the O 2p state (see Figure 14a). This is in striking contrast to $LiNbO_3$, where the valence band is composed of the O 2p state, without any significant participation of Li orbitals (see Figure 14b). Thus, the covalent bond character of *A*-site cations is obvious for $CuNbO_3$. Ehe Nb 4d states of $CuNbO_3$ and $LiNbO_3$, completely empty in the ionic limits, are slightly occupied through orbital overlap with the O 2p states, forming the bottom of the valence band. This is indicative of the Nb–O covalency that drives the second-order Jahn–Teller effect. I believe that the covalent character of Cu–O bond can induce a polar structure in other compounds without $6s^2$ or second-order Jahn-Teller active cations as observed in Pv-$CuNbO_3$.

4.4 Summary of This Chapter

A novel perovskite niobate, $CuNbO_3$, is found to form a monoclinic *Pc* structure as a ground state, representing a rare example of a "noncollinear ferrielectric" dipole order. The *Pc* phase transforms to a "collinear ferroelectric" $R3c$ structure upon heating at 470 K. The noncollinear ferrielectric (*Pc*)–collinear ferroelectric ($R3c$) transition is of displacive origin, and the condensed soft mode responsible for the phase transition is observed at the F point of the rhombohedral Brillouin zone, which corresponds to the structural distortion mainly due to the antiparallel off-center Nb displacements and the $a^-a^-c^-$ NbO_6 octahedral tilting. The original distortion within the monoclinic *Pc* perovskite phase, in particular with respect to $LiNbO_3$, is explained on the basis of bonding character, as highlighted by the electronic structure calculations.

4.5 Tables and Figures

Table 1. Structural Parameters of Pv-$CuNbO_3$ at 470 K Obtained from Refinements against the SXRD Data

atom	site	*g*	*x*	*y*	*z*	$U_{\mathrm{eq/iso}}$ / Å^2
Cu1	6*a*	0.929(9)	0	0	0.255(3)	0.035(3)
Nb1	6*a*	1	0	0	0	0.0166(7)
O1	18*b*	1	0.078(3)	0.352(5)	0.078(2)	0.01665(1)

Space group: *R*3*c* (No. 161), $Z = 6$. $Cu_{0.93}NbO_3$ (fw = 199.9 g mol^{-1}): $\lambda = 0.77565$ Å, lattice parameters: $a = 5.2433(2)$ Å, $c = 14.0006(4)$ Å, and $V = 333.34(2)$ Å^3, $R_{\mathrm{wp}} = 7.91$ %, $R_{\mathrm{B}} = 7.11$ %. Cu1 and Nb1 were refined anisotropically.

Table 2. Structural Parameters of Pv-$CuNbO_3$ at 300 K Obtained from Refinements against the SXRD Data

atom	site	*g*	*x*	*y*	*z*	U_{iso} / Å^2
Cu1	2*a*	1	0.5269(4)	0.9961(19)	0.2100(3)	0.0153(7)
Cu2	2*a*	1	0.9986(4)	0.4953(17)	0.7206(3)	0.0082(6)
Nb1	2*a*	1	0	0	0	0.0100(5)
Nb2	2*a*	1	0.4910(3)	0.5074(6)	0.4513(2)	0.0020(3)
O1	2*a*	1	0.183(3)	0.687(3)	0.428(2)	0.0020(3)
O2	2*a*	1	0.691(3)	0.193(3)	0.928(2)	$=U_{\mathrm{iso}}$(O1)
O3	2*a*	1	0.289(3)	0.204(3)	0.537(2)	$=U_{\mathrm{iso}}$(O1)
O4	2*a*	1	0.791(3)	0.707(3)	0.028(2)	$=U_{\mathrm{iso}}$(O1)
O5	2*a*	1	0.962(2)	0.103(3)	0.227(1)	$=U_{\mathrm{iso}}$(O1)
O6	2*a*	1	0.475(2)	0.612(2)	0.716(1)	$=U_{\mathrm{iso}}$(O1)

Space group: *Pc* (No. 7), $Z = 4$. $CuNbO_3$ (fw = 204.45 g mol^{-1}): $\lambda = 0.75003$ Å, lattice parameters: $a = 5.54535(4)$ Å, $b = 5.21029(3)$ Å, $c = 7.67491(6)$Å, $\beta = 94.6924(6)$°, and $V = 221.007(3)$ Å^3, $R_{\mathrm{wp}} = 11.60$ % and $R_{\mathrm{B}} = 6.62$ %.

Table 3. Structural Parameters of Pv-$CuNbO_3$ at 300 K Obtained from Refinements against the NPD Data

atom	site	g	x	y	z	$U_{eq/iso}$/Å^2
Cu1	2*a*	1	0.514(4)	0.988(2)	0.226(2)	0.065(5)
Cu2	2*a*	1	0.989(2)	0.498(2)	0.735(2)	0.011(1)
Nb1	2*a*	1	0	0	0	0.094(13)
Nb2	2*a*	1	0.4830(14)	0.5122(14)	0.4610(8)	0.015(2)
O1	2*a*	1	0.184(2)	0.686(2)	0.433(2)	0.007(1)
O2	2*a*	1	0.686(3)	0.185(2)	0.935(2)	0.014(2)
O3	2*a*	1	0.290(3)	0.205(2)	0.546(2)	0.005(2)
O4	2*a*	1	0.795(3)	0.701(2)	0.043(2)	0.002(2)
O5	2*a*	1	0.993(3)	0.119(2)	0.233(2)	0.007(1)
O6	2*a*	1	0.491(3)	0.613(2)	0.733(2)	0.008(2)

Space group: *Pc* (No. 7), $Z = 4$. $CuNbO_3$ (fw = 204.45 g mol^{-1}): $\lambda = 1.594$ Å, lattice parameters: a = 5.548088(10) Å, b = 5.208766(9) Å, c = 7.695716(15) Å, β = 94.67983(10)° , and V = 221.6547(7) Å^3, R_{wp} = 10.34 % and R_B = 3.66 %. Cu1 was refined anisotropically.

Table 4. Selected Bond Lengths (Å) and Bond Angles (deg) of Pv-$CuNbO_3$ at 300 K.

		Cu−O						Nb−O			
		Shorter bonds									
Cu1	−O2	2.01(2)	Cu2	−O1	2.03(2)	Nb1	−O1	2.02(1)	Nb2	−O1	1.89(1)
	−O3	2.04(3)		−O4	2.03(2)		−O2	2.02(2)		−O2	1.96(2)
	−O6	2.08(1)		−O5	2.00(1)		−O3	1.94(2)		−O3	2.06(2)
		Longer bonds					−O4	1.98(1)		−O4	2.11(2)
Cu1	−O1	2.97(3)	Cu2	−O1	2.82(2)		−O5	1.90(2)		−O6	1.87(2)
	−O1	3.26(2)		−O2	2.87(2)		−O5	2.14(2)		−O6	2.15(2)
	−O2	2.70(3)		−O2	3.12(2)						
	−O3	3.06(3)		−O3	2.76(2)	Nb1−O5−Nb1			144.1(6)		
	−O4	2.64(3)		−O3	2.82(2)	Nb1−O1−Nb2			144.8(6)		
	−O4	3.22(3)		−O4	2.88(2)	Nb1−O2−Nb2			148.4(6)		
	−O5	2.74(3)		−O5	3.21(1)	Nb1−O3−Nb2			144.5(7)		
	−O5	2.97(3)		−O6	2.83(2)	Nb1−O4−Nb2			146.6(7)		
	−O6	3.14(1)		−O6	2.85(2)	Nb2−O6−Nb2			145.4(8)		

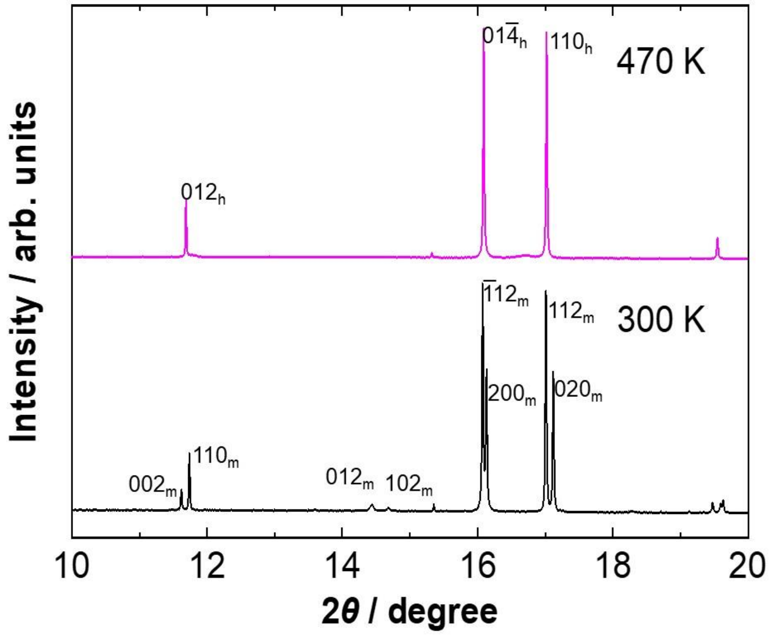

Figure 1. Comparison between SXRD patterns (λ = 0.77565 Å) at 300 K (monoclinic) and at 470 K (rhombohedral). The subscript *h* and *m* represent the rhombohedral unit cell in a hexagonal setting and the monoclinic unit cell, respectively.

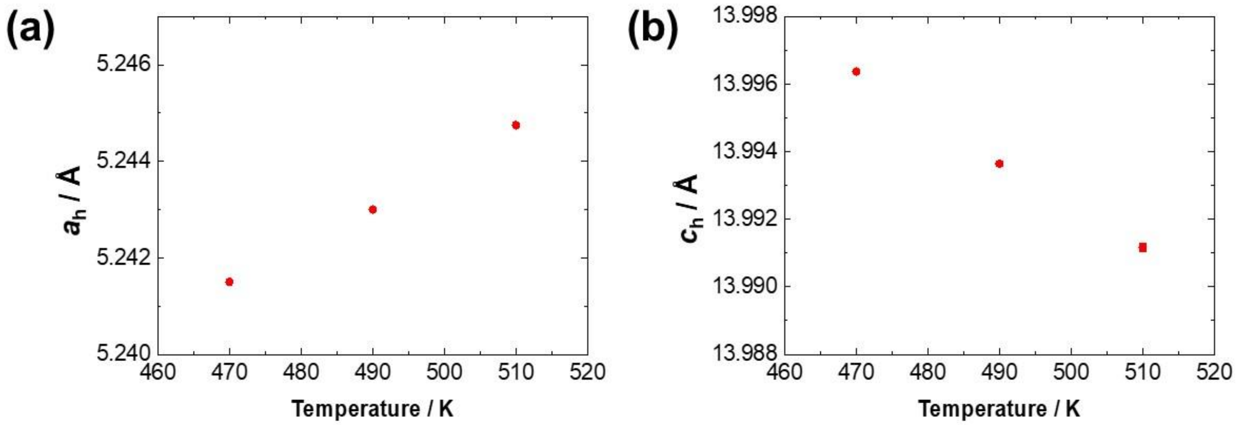

Figure 2. Temperature variation of the lattice parameters of the higher-temperature phase of Pv-CuNbO$_3$, (a) a_h, and (b) c_h, in the hexagonal setting (470 K ≤ T ≤ 510 K).

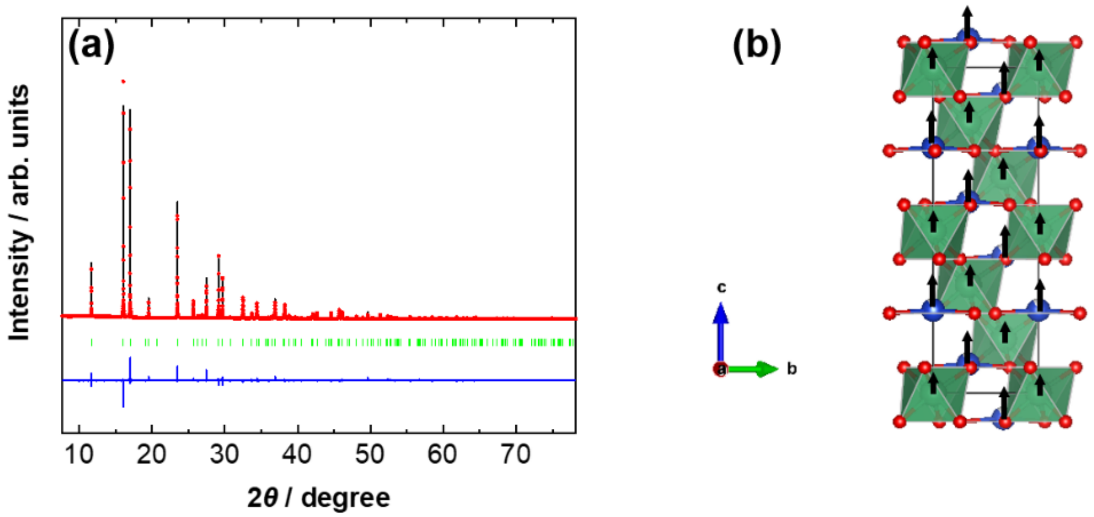

Figure 3. (a) Rietveld refinements against SXRD patterns (λ = 0.77565 Å) of Pv-$CuNbO_3$ at 470 K. The refinement was performed based on the rhombohedral *R*3*c* perovskite-type structure model with *A*-site deficiency (i.e., $LiNbO_3$-type $Cu_{0.93}NbO_3$), showing the observed (red circles) and calculated (solid black lines) profiles. The solid blue lines represent the difference between the observed and calculated profiles. The green ticks correspond to the positions of the allowed Bragg reflections. Peaks of Cu_2O and $CuNb_2O_6$ were excluded in the refinement. (b)The refined crystal structure of *R*3*c* ($LiNbO_3$-type) $Cu_{0.94}NbO_3$ at 470 K. The arrows indicate the cation displacements from the closed-packed oxygen planes and those from the centroids of NbO_6 octahedra.

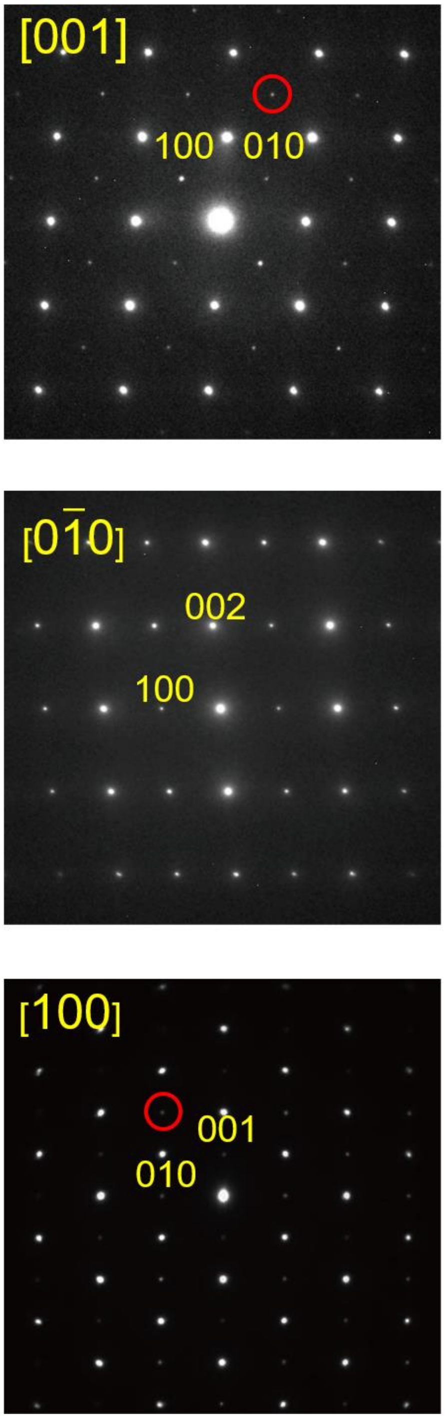

Figure 4. ED patterns of Pv-CuNbO$_3$ at room temperature taken along [001], [0$\bar{1}$0], and [100] zone axes. Representative indices are shown just above the corresponding reflection spots. The reflections marked in red are indicative of a primitive cell.

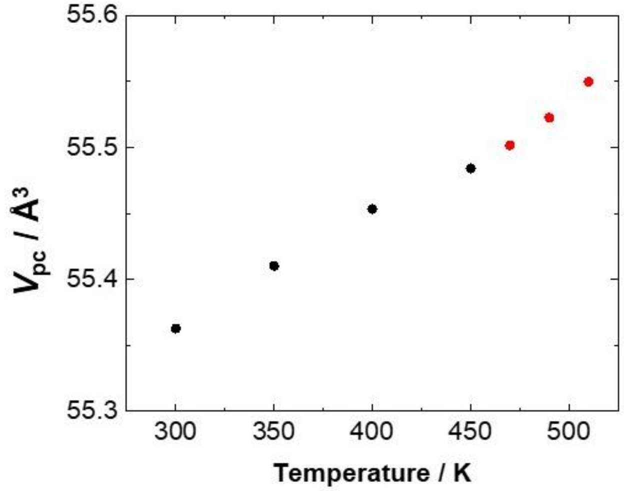

Figure 5. Temperature variation of the pseudo-cubic lattice volumes, V_{pc} for lower-temperature (black circle) and higher-temperature (red circle) Pv-CuNbO$_3$.

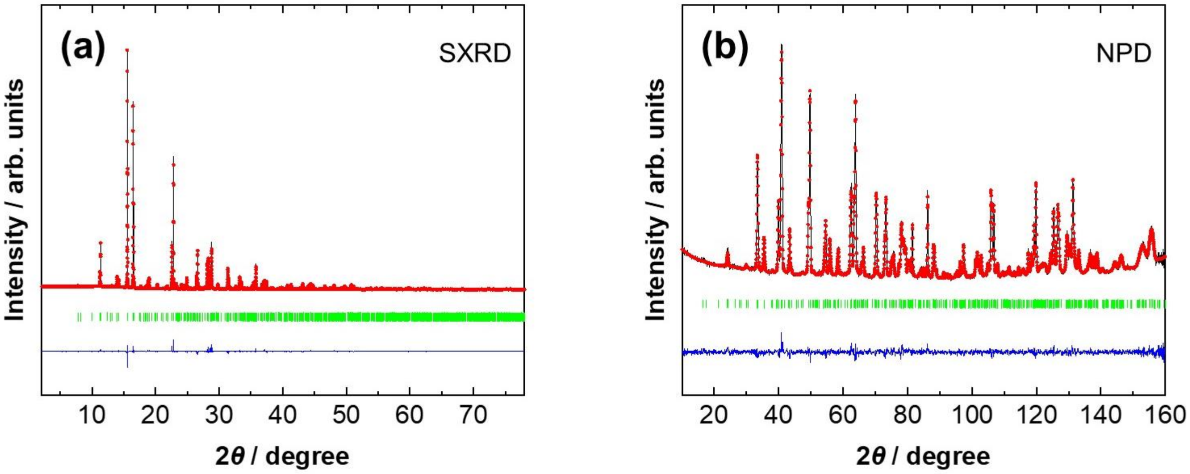

Figure 6. Rietveld refinements against (a) SXRD (λ = 0.75003 Å) and (b) NPD (λ = 1.594 Å) patterns of Pv-CuNbO$_3$ at 300 K. These refinements were performed on the basis of the monoclinic Pc perovskite-type structure model with a $\sqrt{2}a_{\mathrm{pc}} \times \sqrt{2}a_{\mathrm{pc}} \times 2a_{\mathrm{pc}}$ unit cell, showing the observed (red circles) and calculated (solid black lines) profiles. The solid blue lines represent the difference between the observed and calculated profiles. The green ticks correspond to the positions of the allowed Bragg reflections.

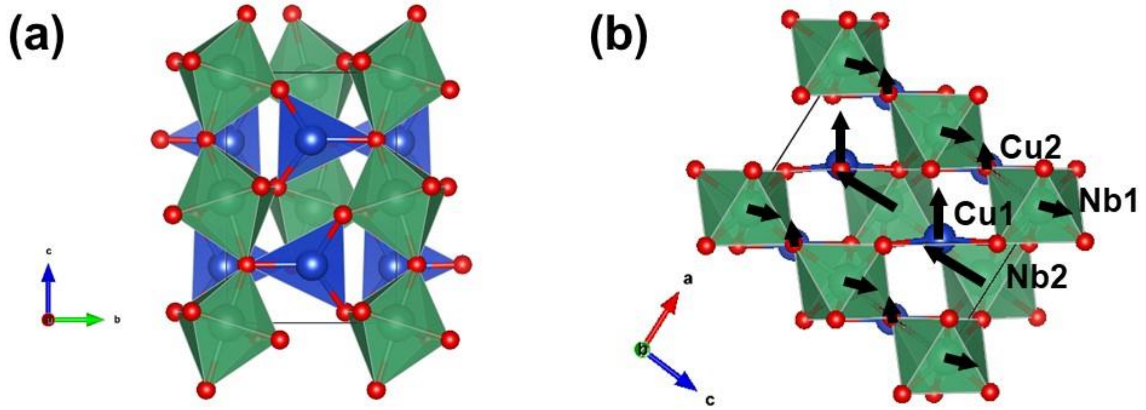

Figure 7. The refined crystal structures of Pv-$CuNbO_3$ from the NPD data at 300 K. The structural views in (a) *bc* and (b) *ac* planes are shown. The arrows in (b) indicate the cation displacements from the closed-packed oxygen planes and those from the centroids of NbO_6 octahedra.

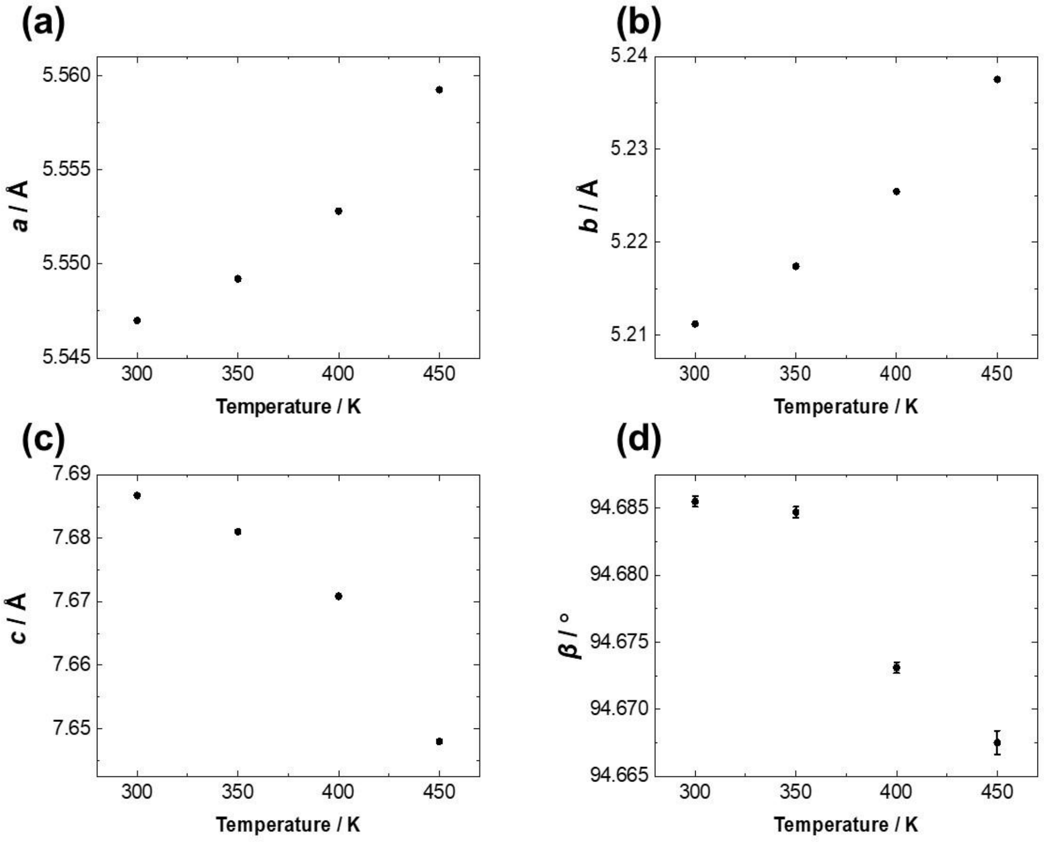

Figure 8. Temperature variation of the lattice parameters of lower-temperature (*Pc*) phase of Pv-$CuNbO_3$, (a) *a*, (b) *b*, (c) c, and (d) β ($300\ \text{K} \leq T \leq 450\ \text{K}$).

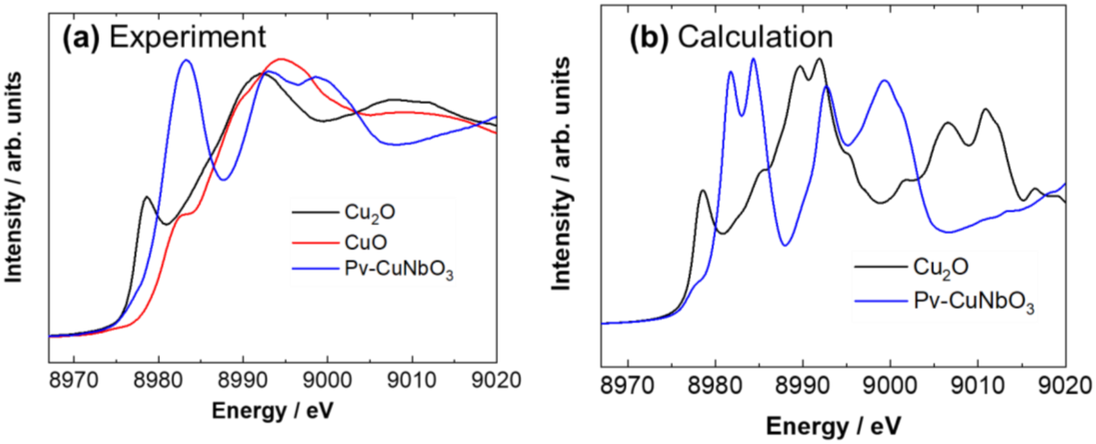

Figure 9. (a) The experimental Cu *K*-edge XANES spectrum of Pv-CuNbO$_3$ (blue) in comparison with those of Cu$_2$O (black) and CuO (red). (b) The calculated Cu *K*-edge XANES spectra of Pv-CuNbO$_3$ (blue) and Cu$_2$O (black).

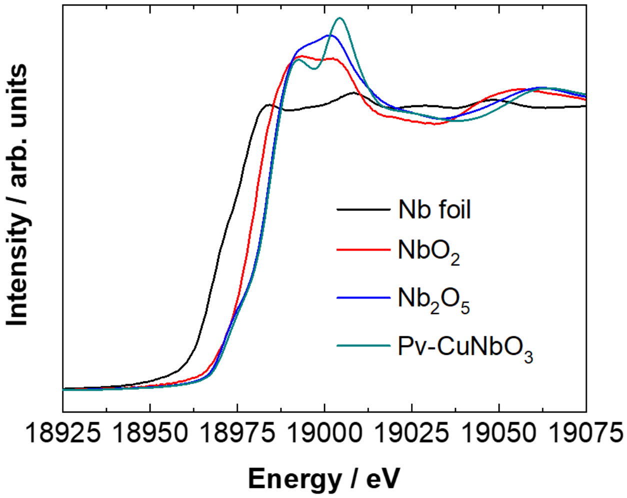

Figure 10. The experimental Nb *K*-edge XANES spectrum of Pv-CuNbO$_3$ (green) in comparison with those of Nb foil (black), NbO$_2$ (red), and Nb$_2$O$_5$ (blue).

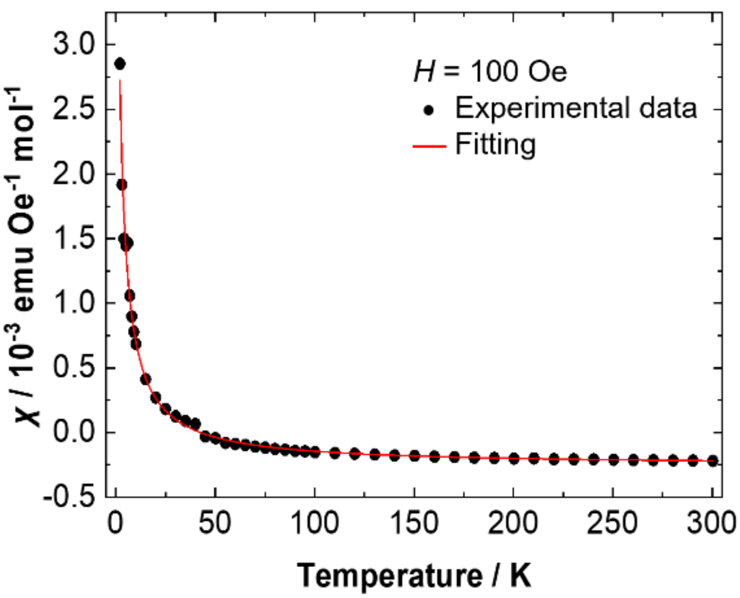

Figure 11. Temperature dependence of magnetic susceptibility, $\chi = M/H$, of Pv-CuNbO$_3$ measured at H = 100 Oe after zero-field cooling. The dots represent the observed data, while the solid red line is the fitted curve according to the Curie−Weiss law.

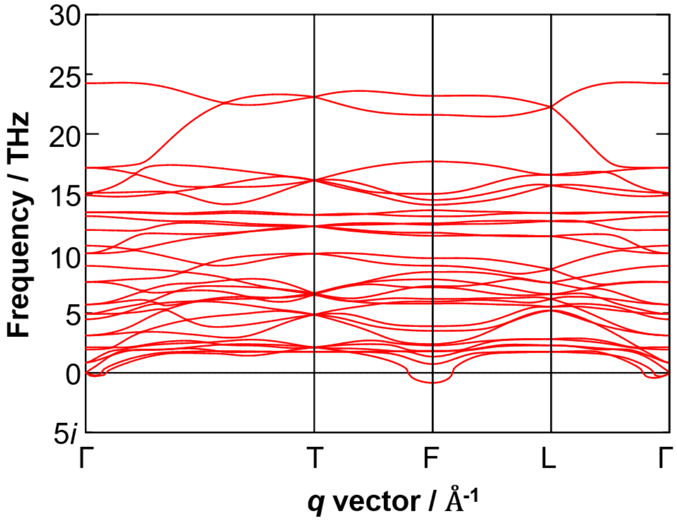

Figure 12. Phonon dispersion curves of Pv-CuNbO$_3$ calculated with the $R3c$ symmetry.

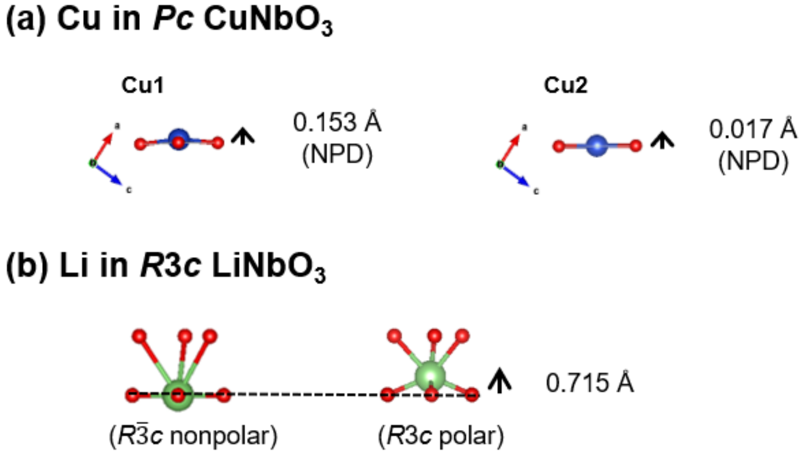

Figure 13. Short distance coordination around (a) Cu in Pv-CuNbO$_3$ (this work) and (b) Li in LiNbO$_3$ (from Ref. 21). The light green, blue, and red spheres correspond to Li, Cu, and O atoms, respectively.

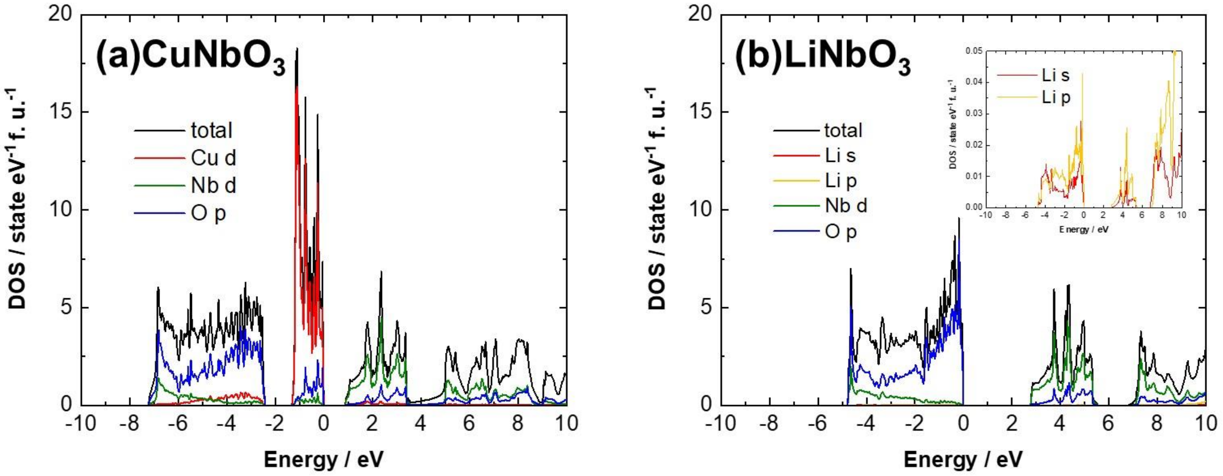

Figure 14. The calculated projected total and partial density of states (DOS) of *R*3*c* (a) CuNbO$_3$ and (b) LiNbO$_3$. The zero of energy is set to the top of the valence band. The inset of (b) shows an enlarged view of the partial DOS of Li 4s and Li 4p states.

4.6 References

(1) Cohen, D. A.; Hossein-Zadeh, M.; Levi, A. F. J. High-Q Microphotonic Electro-Optic Modulator. *Solid State Electron.* **2001**, *45* (9), 1577–1589.

(2) Saito, Y.; Takao, H.; Tani, T.; Nonoyama, T.; Takatori, K.; Homma, T.; Nagaya, T.; Nakamura, M. Lead-Free Piezoceramics. *Nature* **2004**, *432* (7013), 84–87.

(3) Lv, X.; Zhu, J.; Xiao, D.; Zhang, X.-X.; Wu, J. Emerging New Phase Boundary in Potassium Sodium-Niobate Based Ceramics. *Chem. Soc. Rev.* **2020**, *49* (3), 671–707.

(4) Liu, J. W.; Chen, G.; Li, Z. H.; Zhang, Z. G. Hydrothermal Synthesis and Photocatalytic Properties of $ATaO_3$ and $ANbO_3$ (A=Na and K). *Int. J. Hydrogen Energy* **2007**, *32* (13), 2269–2272.

(5) Huan, Y.; Shen, H. T.; Zhu, Y. N.; Li, M.; Li, H. Y.; Wang, Z. X.; Hao, Y. A.; Wei, T. Enhanced Ferro-Photocatalytic Performance for $ANbO_3$ (A = Na, K) Nanoparticles. *Math. Biosci. Eng.* **2019**, *16* (5), 4122–4134.

(6) Shirane, G.; Danner, H.; Pavlovic, A.; Pepinsky, R. Phase Transitions in Ferroelectric $KNbO_3$. *Phys. Rev.* **1954**, *93* (4), 672–673.

(7) Kawamura, S.; Magome, E.; Moriyoshi, C.; Kuroiwa, Y.; Taniguchi, N.; Tanaka, H.; Maki, S.; Takata, M.; Wada, S. Electronic Polarization in $KNbO_3$ Visualized by Synchrotron Radiation Powder Diffraction. *Jpn. J. Appl. Phys.* **2013**, *52* (9S1), 09KF04.

(8) Cohen, R. E. Origin of Ferroelectricity in Perovskite Oxides. *Nature* **1992**, *358* (6382), 136–138.

(9) Kunz, M.; Brown, I. D. Out-of-Center Distortions around Octahedrally Coordinated D^0 Transition Metals. *J. Solid State Chem.* **1995**, *115* (2), 395–406.

(10) Ok, K. M.; Halasyamani, P. S.; Casanova, D.; Llunell, M.; Alemany, P.; Alvarez, S. Distortions in Octahedrally Coordinated d^0 Transition Metal Oxides: A Continuous Symmetry Measures Approach. *Chem. Mater.* **2006**, *18* (14), 3176–3183.

(11) Abrahams, S. C.; Reddy, J. M.; Bernstein, J. L. Ferroelectric Lithium Niobate. 3. Single Crystal X-Ray Diffraction Study at 24°C. *J. Phys. Chem. Solids* **1966**, *27* (6–7), 997–1012.

(12) Sánchez-Dena, O.; Fierro-Ruiz, C. D.; Villalobos-Mendoza, S. D.; Carrillo Flores, D. M.; Elizalde-Galindo, J. T.; Farías, R. Lithium Niobate Single Crystals and Powders Reviewed—Part I. *Crystals* **2020**, *10* (11), 973.

(13) Sánchez-Dena, O.; Villalobos-Mendoza, S. D.; Farías, R.; Fierro-Ruiz, C. D. Lithium Niobate

Single Crystals and Powders Reviewed—Part II. *Crystals* **2020**, *10* (11), 990.

(14) Megaw, H. D. The Seven Phases of Sodium Niobate. *Ferroelectrics* **1974**, *7* (1), 87–89.

(15) Sciau, P.; Kania, A.; Dkhil, B.; Suard, E.; Ratuszna, A. Structural Investigation of $AgNbO_3$ Phases Using X-Ray and Neutron Diffraction. *J. Phys. Condens. Matter* **2004**, *16* (16), 2795.

(16) Fu, D.; Endo, M.; Taniguchi, H.; Taniyama, T.; Itoh, M. $AgNbO_3$: A Lead-Free Material with Large Polarization and Electromechanical Response. *Appl. Phys. Lett.* **2007**, *90* (25), 252907.

(17) Koruza, J.; Tellier, J.; Malič, B.; Bobnar, V.; Kosec, M. Phase Transitions of Sodium Niobate Powder and Ceramics, Prepared by Solid State Synthesis. *J. Appl. Phys.* **2010**, *108* (11), 113509.

(18) Yashima, M.; Matsuyama, S.; Sano, R.; Itoh, M.; Tsuda, K.; Fu, D. Structure of Ferroelectric Silver Niobate $AgNbO_3$. *Chem. Mater.* **2011**, *23* (7), 1643–1645.

(19) Yashima, M.; Matsuyama, S. Origin of the Ferrielectricty and Visible-Light Photocatalytic Activity of Silver Niobate $AgNbO_3$. *J. Phys. Chem. C* **2012**, *116* (47), 24902–24906.

(20) Joshi, U. A.; Palasyuk, A. M.; Maggard, P. A. Photoelectrochemical Investigation and Electronic Structure of a P-Type $CuNbO_3$ Photocathode. *J. Phys. Chem. C* **2011**, *115* (27), 13534–13539.

(21) Harb, M.; Masih, D.; Takanabe, K. Screened Coulomb Hybrid DFT Investigation of Band Gap and Optical Absorption Predictions of $CuVO_3$, $CuNbO_3$ and $Cu_5Ta_{11}O_{30}$ Materials. *Phys. Chem. Chem. Phys.* **2014**, *16* (34), 18198–18204.

(22) Sleight, A. W.; Prewitt, C. T. Preparation of $CuNbO_3$ and $CuTaO_3$ at High Pressure. *Mater. Res. Bull.* **1970**, *5* (3), 207–211.

(23) Sugii, K.; Koizumi, H.; Miyazawa, S.; Kondo, S. Temperature Variations of Lattice Parameters of $LiNbO_3$, $LiTaO_3$ and $Li(Nb_{1-y}Ta_y)O_3$ Solid-Solutions. *J. Cryst. Growth* **1976**, *33* (1), 199–202.

(24) Shi, Y.; Guo, Y.; Wang, X.; Princep, A. J.; Khalyavin, D.; Manuel, P.; Michiue, Y.; Sato, A.; Tsuda, K.; Yu, S.; Arai, M.; Shirako, Y.; Akaogi, M.; Wang, N.; Yamaura, K.; Boothroyd, A. T. A Ferroelectric-like Structural Transition in a Metal. *Nat. Mater.* **2013**, *12* (11), 1024–1027.

(25) Campbell, B. J.; Stokes, H. T.; Tanner, D. E.; Hatch, D. M. *ISODISPLACE*: A Web-Based Tool for Exploring Structural Distortions. *J. Appl. Crystallogr.* **2006**, *39* (4), 607–614.

(26) Altomare, A.; Cuocci, C.; Giacovazzo, C.; Moliterni, A.; Rizzi, R.; Corriero, N.; Falcicchio, A. *EXPO2013*: A Kit of Tools for Phasing Crystal Structures from Powder Data. *J. Appl. Crystallogr.* **2013**, *46* (4), 1231–1235.

(27) Abrahams, S. C.; Marsh, P. Defect Structure Dependence on Composition in Lithium Niobate.

Acta Crystallogr. B **1986**, *42* (1), 61–68.

(28) Iyi, N.; Kitamura, K.; Izumi, F.; Yamamoto, J. K.; Hayashi, T.; Asano, H.; Kimura, S. Comparative Study of Defect Structures in Lithium Niobate with Different Compositions. *J. Solid State Chem.* **1992**, *101* (2), 340–352.

(29) Brese, N. E.; O'Keeffe, M. Bond-Valence Parameters for Solids. *Acta Crystallogr. B* **1991**, *47* (2), 192–197.

(30) Glazer, A. M. The Classification of Tilted Octahedra in Perovskites. *Acta Crystallogr. B* **1972**, *28* (11), 3384–3392.

(31) Johnston, K. E.; Tang, C. C.; Parker, J. E.; Knight, K. S.; Lightfoot, P.; Ashbrook, S. E. The Polar Phase of $NaNbO_3$: A Combined Study by Powder Diffraction, Solid-State NMR, and First-Principles Calculations. *J. Am. Chem. Soc.* **2010**, *132* (25), 8732–8746.

(32) Salje, E. K. H.; Rehmann, S.; Pobell, F.; Morris, D.; Knight, K. S.; Herrmannsdörfer, T.; Dove, M. T. Crystal Structure and Paramagnetic Behaviour of ε-WO_{3-x}. *J. Phys. Condens. Matter* **1997**, *9* (31), 6563.

(33) Kawamoto, T.; Fujita, K.; Yamada, I.; Matoba, T.; Kim, S. J.; Gao, P.; Pan, X.; Findlay, S. D.; Tassel, C.; Kageyama, H.; Studer, A. J.; Hester, J.; Irifune, T.; Akamatsu, H.; Tanaka, K. Room-Temperature Polar Ferromagnet $ScFeO_3$ Transformed from a High-Pressure Orthorhombic Perovskite Phase. *J. Am. Chem. Soc.* **2014**, *136* (43), 15291–15299.

(34) Fujita, K.; Kawamoto, T.; Yamada, I.; Hernandez, O.; Hayashi, N.; Akamatsu, H.; Lafargue-Dit-Hauret, W.; Rocquefelte, X.; Fukuzumi, M.; Manuel, P.; Studer, A. J.; Knee, C. S.; Tanaka, K. $LiNbO_3$-Type $InFeO_3$: Room-Temperature Polar Magnet without Second-Order Jahn–Teller Active Ions. *Chem. Mater.* **2016**, *28* (18), 6644–6655.

(35) Niu, H.; Pitcher, M. J.; Corkett, A. J.; Ling, S.; Mandal, P.; Zanella, M.; Dawson, K.; Stamenov, P.; Batuk, D.; Abakumov, A. M.; Bull, C. L.; Smith, R. I.; Murray, C. A.; Day, S. J.; Slater, B.; Cora, F.; Claridge, J. B.; Rosseinsky, M. J. Room Temperature Magnetically Ordered Polar Corundum GaFeO3 Displaying Magnetoelectric Coupling. *J. Am. Chem. Soc.* **2017**, *139* (4), 1520–1531.

(36) Sleight, A. W.; Prewitt, C. T. High-Pressure $HgTiO_3$ and $HgPbO_3$: Preparation, Characterization, and Structure. *J. Solid State Chem.* **1973**, *6* (4), 509–512.

(37) Ko, J.; Prewitt, C. T. High-Pressure Phase Transition in $MnTiO_3$ from the Ilmenite to the $LiNbO_3$ Structure. *Phys. Chem. Miner.* **1988**, *15* (4), 355–362.

(38) Leinenweber, K.; Utsumi, W.; Tsuchida, Y.; Yagi, T.; Kurita, K. Unquenchable High-Pressure Perovskite Polymorphs of $MnSnO_3$ and $FeTiO_3$. *Phys. Chem. Miner.* **1991**, *18* (4), 244–250.

(39) Linton, J. A.; Fei, Y.; Navrotsky, A. Complete Fe-Mg Solid Solution in Lithium Niobate and Perovskite Structures in Titanates at High Pressures and Temperatures. *Am. Mineral.* **1997**, *82* (5–6), 639–642.

(40) Shan, Y. J.; Inaguma, Y.; Tetsuka, H.; Nakamura, T.; Gauckler, L. J. Synthesis and Phase Transition of $HgTiO_3$. *Ferroelectrics* **2006**, *337* (1), 71–76.

(41) Aimi, A.; Katsumata, T.; Mori, D.; Fu, D.; Itoh, M.; Kyômen, T.; Hiraki, K.-I.; Takahashi, T.; Inaguma, Y. High-Pressure Synthesis and Correlation between Structure, Magnetic, and Dielectric Properties in $LiNbO_3$-Type Mn$M$$O_3$ (M=Ti, Sn). *Inorg. Chem.* **2011**, *50* (13), 6392–6398.

(42) Inaguma, Y.; Aimi, A.; Shirako, Y.; Sakurai, D.; Mori, D.; Kojitani, H.; Akaogi, M.; Nakayama, M. High-Pressure Synthesis, Crystal Structure, and Phase Stability Relations of a $LiNbO_3$-Type Polar Titanate $ZnTiO_3$ and Its Reinforced Polarity by the Second-Order Jahn-Teller Effect. *J. Am. Chem. Soc.* **2014**, *136* (7), 2748–2756.

(43) Inaguma, Y.; Aimi, A.; Mori, D.; Katsumata, T.; Ohtake, M.; Nakayama, M.; Yonemura, M. High-Pressure Synthesis, Crystal Structure, Chemical Bonding, and Ferroelectricity of $LiNbO_3$-Type $LiSbO_3$. *Inorg. Chem.* **2018**, *57* (24), 15462–15473.

(44) Ishida, K.; Ikeuchi, Y.; Tassel, C.; Takatsu, H.; Brown, C. M.; Kageyama, H. High-Pressure Synthesis of Non-Stoichiometric Li_xWO_3 ($0.5 \leq x \leq 1.0$) with $LiNbO_3$ Structure. *Inorganics* **2019**, *7* (5), 63.

Chapter 5. Topochemical Synthesis of $CuNb_2O_6$ with Colossal Dielectric Constant

*This work has already been published in *J. Mater. Chem. C* **2021**, *9* (39), 13981–13990. Reprinted with permission from "Fukuda, M.; Yamada, I.; Hojo, H.; Takahashi, C.; Yoshida, Y.; Tanaka, K.; Azuma, M.; Fujita, K. Topochemical Synthesis of Perovskite-Type $CuNb_2O_6$ with Colossal Dielectric Constant. *J. Mater. Chem. C* **2021**, *9* (39), 13981–13990." Copyright 2021 the Royal Society of Chemistry.

In this chapter, I report a novel A-site deficient quadruple perovskite (Pv) oxide, $CuNb_2O_6$, obtained by a combination of high-pressure synthesis and topochemical structural transformation. Post-annealing of high-pressure-synthesized Pv-$CuNbO_3$ above 470 K at ambient pressure leads to the formation of Pv-$CuNb_2O_6$ due to the topochemical deinsertion of half of the copper ions, which is accompanied by changes in the valence state and coordination environment of the remaining copper ions from triangular coordinated Cu^+ into square-planar coordinated Cu^{2+}. A combined structural analysis shows that Pv-$CuNb_2O_6$ crystallizes into a non-centrosymmetric cubic structure. Magnetic characterization reveals an antiferromagnetic order below 12 K. I find that this compound exhibits a colossal dielectric constant up to the order of 10^4. The topochemical cation deinsertion is also found in another high-pressure-synthesized Pv-$CuTaO_3$, which produces cubic $Pm\overline{3}$ Pv-$CuTa_2O_6$.

5.1 Introduction

Topochemical reactions in perovskites and related compounds have attracted much attention because they provide a series of new compounds not obtainable by conventional solid-state reactions.[1,2] During the topochemical reactions, products retain the structural topology of starting materials. Topochemical methods are powerful pathways for searching materials with exotic physical properties, like piezoelectricity[3,4] and ionic conductivity.[5,6] There have been several reports on "hard-soft" chemistry, where the "soft" topochemical modification is combined with "hard" high-pressure synthesis techniques. For example, topochemical reactions such as reduction or anion exchange are performed "softly" for the dense perovskite-type $ACrO_3$ (A = Ca and Sr) whose instabilities are locked "hardly" under high-pressure conditions.[7–10] This approach can topochemically expand the possibility of stabilizing new compounds.

In this section, I report a new type of "hard-soft" route involving cation deinsertion with high-pressure synthesis. I observed that Pv-$CuNbO_3$ is stabilized under high-pressure and high-temperature conditions and exhibits a monoclinic-rhombohedral phase transition upon heating to 470 K at ambient pressure (see **Chapter 4**). Almost simultaneously with the phase transition, the rhombohedral phase decomposes into Pv-$CuNb_2O_6$ and Cu_2O. In the transformation of Pv-$CuNbO_3$ to Pv-$CuNb_2O_6$, half of the copper ions are removed, and the valence state and coordination environment of the remaining half of the copper ions change from triangular coordinated Cu^+ into square-planar coordinated Cu^{2+}. Note that NbO_6 corner-sharing networks are retained during this structural modification (Figure. 1). The formation process of Pv-$CuNb_2O_6$ thus represents a rare example of the topochemical cation deinsertion.

While Pv-$CuTa_2O_6$ can be synthesized by the conventional solid-state reactions, Pv-$CuNb_2O_6$ had not been reported.[11,12] Instead, orthorhombic and monoclinic columbite-type $CuNb_2O_6$ has been obtained by conventional solid-state reactions.[11,13,14] $LiNbO_3$-type $Li_{1-x}Cu_xNbO_3$ has been synthesized by lithium insertion into columbite-type $CuNb_2O_6$.[15] However, this reaction is not the topochemical reaction defined here because the NbO_6 connectivity changed during the reaction; The NbO_6 octahedra in the columbite-type structure form chains connected by edge-sharing, unlike a corner-sharing network in perovskite-type structures.

It is known that many quadruple perovskite-type oxides like Pv-$CuTa_2O_6$ display interesting dielectric properties. Since the giant dielectric constant ($\varepsilon' \approx 10^5$) was reported for a quadruple perovskite-type oxide, $CaCu_3Ti_4O_{12}$, in 2000,[16] the dielectric properties of this and the related derivatives have been intensively studied.[17–22] The significant tilt distortion of the BO_6 octahedra in $CaCu_3Ti_4O_{12}$ yields a complex A-cation ordering of 12-coordinated A- (Ca-) sites and planar-coordinated A'- (Cu-) sites. Because of the ordered arrangement of the two distinct A- and A'-sites in the ratio of 1:3, $CaCu_3Ti_4O_{12}$ is classified as a "quadruple" perovskite. A-site deficient quadruple perovskite-type compounds, Pv-$CuTa_2O_6$ and Pv-$LiCuNb_3O_9$, show crystal structures similar to $AA'_3B_4O_{12}$, but the A- (Ca-) sites are fully vacant in both the cases, and the A'-sites are nominally two-thirds occupied by Cu^{2+} ions in Pv-$CuTa_2O_6$[23,24] and eight-ninth by Li^+ and Cu^{2+}

ions in Pv-$LiCuNb_3O_9$.[25] They exhibit as large dielectric constant ($\varepsilon' \approx 10^5$) as $CaCu_3Ti_4O_{12}$.[26–32]

Pv-$CuTa_2O_6$ is also known to exhibit compositional flexibility on Cu stoichiometry. The copper ions are present as the mixed-valence state of Cu^+ and Cu^{2+} ions, and the formal composition can be described as $Cu_{1+x}Ta_2O_6$. Similarly, Pv-$LiCuNb_3O_9$ has been reported to contain Cu^+ and Cu^{2+} ions in an approximately 1:9 ratio.[29] Such mixed-valence states are suggested to be one of the reasons for the giant dielectric constant of Pv-$CuTa_2O_6$ and Pv-$LiCuNb_3O_9$. Further, depending on the cooling rate from the sintering temperatures (1293 K), either orthorhombic or cubic phase is observed in $Cu_{1+x}Ta_2O_6$ ($x < 0.2$).[33] The slow-cooled Pv-$CuTa_2O_6$ is orthorhombic with an ordered arrangement of Cu-rich and Cu-poor layers along the *c*-axis (Figure 2(a)). The rapid-cooled one is cubic without such a layered ordering (Figure 2(b)). On the other hand, Pv-$LiCuNb_3O_9$ crystallizes into only a cubic *I*23 structure (Figure 2(c)).[25]

Herein, I have revisited the topochemical reaction of Pv-$CuNbO_3$ and succeeded in isolating the novel A-site deficient quadruple perovskite, Pv-$CuNb_2O_6$. I present the detailed crystal structure of Pv-$CuNb_2O_6$. I also demonstrate that this compound behaves as an antiferromagnet with T_N = 12 K and exhibits a colossal dielectric constant at room temperature. Thus, my work will provide a new approach to developing functional materials.

5.2 Results and Discussion

5.2.1 Crystallography

Figure 3 shows laboratory XRD patterns of the as-synthesized $CuNbO_3$ sample synthesized at 12 GPa and 1273 K and that post-annealed at 773 K and ambient pressure. One can see that the high-pressure-synthesized Pv-$CuNbO_3$ decomposed into Pv-$CuNb_2O_6$ and CuO upon heating. The difference in the copper oxide products in the **Chapter 4** (Cu_2O) and this chapter (CuO) is due to the oxygen contents in the closed capillary and in an open system. The deposition of smaller CuO grains onto larger Pv-$CuNb_2O_6$ grains was observed through HAADF images and EDX results (Figure 4).

To get more detailed information on Pv-$CuNb_2O_6$, I removed CuO from the mixture of Pv-$CuNb_2O_6$ and CuO using HCl solution and successfully obtained the single-phase brown-colored sample. Figure. 5 displays the SXRD pattern of the washed sample at 300 K. The diffraction peaks from CuO disappeared, and only those from Pv-$CuNb_2O_6$ remained. The SXRD pattern revealed that Pv-$CuNb_2O_6$ has the superstructure with an enlarged $2a_{pc} \times 2a_{pc} \times 2a_{pc}$ unit cell, indicating the formation of an A-site deficient quadruple perovskite-type structure. Previous reports for Pv-$CuTa_2O_6$ show that the cubic and orthorhombic phases can be distinguished from each other, seeing the absence or presence of splitting of various diffraction peaks in XRD patterns, such as 400.[52] The layered ordering in the orthorhombic phase causes a difference between a and c-lattice parameters. As shown in the inset of Figure 5, no peak splitting was observed for Pv-$CuNb_2O_6$, revealing that it belongs to the cubic symmetry.

I deduced the space group of Pv-$CuNb_2O_6$ based on the two reflection conditions commonly found in both the SXRD (Figure 5) and ED (Figure 8) patterns ($0kl$: $k + l$ = even and $00l$: l = even). There are nine possible space groups that satisfy the reflection conditions. In order to identify the space group, I checked SHG responses of Pv-$CuNb_2O_6$ and a reference material (cubic Pv-$CuTa_2O_6$). I observed that Pv-$CuNb_2O_6$ was SHG active, while cubic Pv-$CuTa_2O_6$ was SHG inactive (Figure 6). The result for Pv-$CuTa_2O_6$ agreed with the previous report that the reference compound belongs to the centrosymmetric space group $Pm\overline{3}$. In contrast to the case of Pv-$CuTa_2O_6$, Pv-$CuNb_2O_6$ was found to crystallize in non-centrosymmetric space group. Considering the SXRD and ED reflection conditions and SHG results together, there are three space group candidates ($I23$, $I2_13$, and $I\overline{4}3m$) for Pv-$CuNb_2O_6$. I excluded the two space groups other than $I23$ because they are not compatible with the crystal structure with tilted NbO_6 and planar-coordinated CuO_4, characteristic of quadruple perovskites.

Rietveld refinements against the SXRD data were performed for Pv-$CuNb_2O_6$ using the cubic $I23$ structure of Pv-$LiCuNb_3O_9$ as an initial model. The occupancies of Nb and O atoms were fixed to unity. Some observed peak broadening was selectively relaxed, presumably due to the modulated structures observed in the ED experiment (Figure 8 and 9). Refinement converged well with a weighted reliability factors of R_{wp} = 8.65 % and R_B = 5.46 %. The Rietveld refinements and the structural parameters are shown in Figure. 5 and Table 1. The refined composition, $Cu_{1.02}Nb_2O_6$, implies that Cu^{2+} ions were slightly reduced to Cu^+ ions, forming $Cu^+_{0.04}Cu^{2+}_{0.98}Nb_2O_6$.

In $I23$ Pv-$CuNb_2O_6$, the Jahn-Teller active Cu ions had four shorter (2.021(4) Å) and four longer bonds (2.803(4) Å). Because of the significant difference in their lengths, the coordination environment of Cu ions can be regarded as a planar one. The overall crystal structures of $I23$ Pv-

$CuNb_2O_6$ and $Pm\overline{3}$ Pv-$CuTa_2O_6$ look very similar, but one can clearly see the difference in the coordination environment of the B-site cations between the two compounds. The B-site cations in $I23$ and $Pm\overline{3}$ Pv-CuB_2O_6 are displaced in the direction of the vacant A-sites, i.e., the vertice or body canter of the quadruple perovskite unit cell. For non-centrosymmetric $I23$ Pv-$CuNb_2O_6$, four Nb^{5+} ions are significantly displaced toward the vertice, and the remaining four Nb^{5+} ions are largely shifted toward the body center (Figure. 7 (a)). On the other hand, for centrosymmetric $Pm\overline{3}$ Pv-$CuTa_2O_6$, all eight Ta^{5+} ions in the unit cell are slightly displaced toward the vertice because of its inversion symmetry (Figure. 7 (b)). Therefore, in Pv-$CuNb_2O_6$, the number of B^{5+} ions displaced toward the same position is half of that in Pv-$CuTa_2O_6$, which suppresses the electrostatic repulsion between B^{5+} ions. Such a reduced cation-cation repulsion should allow the larger second-order Jahn-Teller distortions of Nb^{5+} ions in Pv-$CuNb_2O_6$. Thus, $I23$ Pv-$CuNb_2O_6$ with the larger B-site cations displacements has three longer (2.079(5) Å) and three shorter (1.903(5) Å) Nb-O bonds (Figure. 7 (c)), whereas the six Ta-O bonds of $Pm\overline{3}$ Pv-$CuTa_2O_6$ are almost the same length (1.977(2) Å × 3 and 1.974(2) Å × 3) (Figure. 7 (d)). It is known that both Nb^{5+} ($4d^0$) and Ta^{5+} ($5d^0$) ions are second-order Jahn-Teller active, but generally, Nb^{5+} ions are more greatly shifted within the BO_6 octahedra.[34,35] Further information about refined compositions, crystal symmetries, lattice volumes, selected bond lengths, bond angles, and bond valence sums (BVS)[36] of Pv-CuB_2O_6 (B = Nb, Ta) and Pv-$LiCuNb_3O_9$ are listed in Table 2. The BVS values of Pv-$CuNb_2O_6$, considering the occupancies, are 1.8 and 5.0 for Cu1 and Nb1, respectively, confirming the $Cu^{2+}Nb^{5+}{}_2O_6$ model.

ED experiments were performed at room temperature to examine the crystal symmetry of Pv-$CuNb_2O_6$. Figure 8 shows the ED patterns for the quasi-single-crystal domain along $[1\overline{1}0]$ and [100]. All reflections can be indexed with the same cubic unit cell with $2a_p \times 2a_p \times 2a_p$ as those in the SXRD pattern. At first sight, I suspected that the 001 reflection was present along $[1\overline{1}0]$ (the red arrow in Figure 8(a)). However, this reflection turned out not to be from the basic structure because the 001 reflection was elliptical (not round) in the $[1\overline{1}0]$ axis and not observed along the [100] direction (Figure 8(b)). Given that Pv-$CuNb_2O_6$ belongs to $I23$ as stated above, the hhl reflections with l = odd along the $[1\overline{1}0]$ axis should also be systematically absent. In fact, they exhibit distorted shapes. Thus, these $00l$ and hhl reflections with l = odd in $[1\overline{1}0]$ would be satellite reflections originating from a modulation along the c-axis.

Satellite reflections, indicated by blue arrows, are also observed in the [100] direction (Figure 8(b)).

This observation revealed a modulation along a direction slightly tilted from the *c*-axis. A possible origin of such a structure was the occupancy modulation of Cu ions. As mentioned above, Pv-$CuTa_2O_6$ prepared via slow cooling exhibits a commensurate structure with the occupancy modulation of Cu ions along *c*-axis in the orthorhombic symmetry (Figure 2(a)). In the present case of Pv-$CuNb_2O_6$, the modulation periodicity would be incommensurate with the underlying periodicities of the basic structure. TEM BF observations were made for the [100]-oriented sample, and it was confirmed that the domain structures were almost perpendicular to the *c*-axis (Figure 9). These would be related to the modulated structure. Sattelite peaks associated with such modulation vector were not observed in our SXRD measurement. Further investigations will be required to determine the modulation in detail.

XANES gives us information about not only the valence state of a given element but also its coordination environment.[37,38] Figure 10 shows the room-temperature XANES at Cu and Nb K-edges for Pv-$CuNb_2O_6$ and reference materials. The data of $CaCu_3Ti_4O_{12}$ was taken with permission from a previous report.[39] The Cu K-edge XANES of Pv-$CuNb_2O_6$ was identical in position and shape to that of $CaCu_3Ti_4O_{12}$ but was different from those of Pv-$CuNbO_3$, Cu_2O and CuO. Hence, Cu ions in Pv-$CuNb_2O_6$ were found to adopt the same valence and coordination environment as those in $CaCu_3Ti_4O_{12}$, i.e., Cu^{2+} ions occupying the square-planar coordinated A' sites in quadruple perovskites, $AA'_3B_4O_{12}$. As a result, I confirmed that triangular coordinated Cu^+ ions in Pv-$CuNbO_3$ were changed into square-planar coordinated Cu^{2+} ions in Pv-$CuNb_2O_6$ via the topochemical cation deinsertion (see also Figure 1). Note that a little Cu^+ ions were shown to be present in Pv-$CuNb_2O_6$ through our Rietveld analysis, but they were not detected in XANES due to their meager fraction. The Nb valency in Pv-$CuNb_2O_6$ can be easily estimated to be +5 from the similarity of its Nb K-edge XANES to those of Nb_2O_5 and Pv-$CuNbO_3$.

To additionally probe the topochemical reaction of Pv-$CuNbO_3$ to Pv-$CuNb_2O_6$, thermal analysis was carried out for high-pressure-synthesized Pv-$CuNbO_3$. Figure 11(a) depicts the TG-DTA curves between 300 and 673 K. The exothermic peak with ~3.6 % weight gain was observed around 500–600 K. As demonstrated by XRD data (Figure 11(b)), Pv-$CuNbO_3$ changed into Pv-$CuNb_2O_6$ and CuO after the heating cycle up to 673 K, revealing that the structural instability locked under the "hard" high-pressure condition was released by the "soft" topochemical cation deinsertion. The weight gain corresponds to the change in the oxygen content in the following chemical reaction:

$$CuNbO_3 + 0.23O_2 \rightarrow 0.46CuO + 1/2Cu_{1.08}Nb_2O_6$$

The chemical composition ($Cu_{1.08}Nb_2O_6$) estimated by TG-DTA is in good agreement with the refinement result ($Cu_{1.02}Nb_2O_6$) of SXRD data.

Furthermore, it is known that rhombohedral perovskite-type ($LiNbO_3$-type) $CuTaO_3$ can be synthesized under high-pressure and high-temperature conditions.[40] I found that the high-pressure-synthesized $CuTaO_3$ transforms into cubic Pv-$CuTa_2O_6$ and CuO after post-annealing above 673 K and at ambient pressure (Figure 12). Namely, our "hard-soft" method also brings about the formation of a cubic Pv-$CuTa_2O_6$ via topochemical cation deinsertion, ensuring the availability of this approach.

5.2.2 Magnetic and Dielectric Properties

Figure 13 shows the temperature dependence of magnetic susceptibility, χ, of Pv-$CuNb_2O_6$ measured at 100 Oe under field-cooling (FC) and zero-field cooling (ZFC) conditions. The separation between FC and ZFC curves is observed below 20 K. As the temperature decreases, the FC susceptibility gradually increases. In comparison, the ZFC susceptibility shows a cusp at 12 K. There is no difference between FC and ZFC susceptibilities above 20 K. I analyzed the *M*-*T* curve in the temperature range of 100 to 400 K based on the Curie-Weiss law described by the following equation:

$$\chi = \chi_0 + C / (T - \theta_W),$$

where χ_0 is a temperature-independent term, C is the Curie constant, and θ_W is the Weiss temperature. I obtained $\chi_0 = 3.03(6) \times 10^{-4}$ emu Oe^{-1} mol^{-1}, $C = 0.397(3)$ emu K Oe^{-1} mol^{-1} and $\theta_W = -22.9(7)$ K. The calculated Curie constant agrees with that expected for $0.98Cu^{2+}$ (0.368 emu K Oe^{-1} mol^{-1}) in the refined composition $(Cu^{+}_{0.04}Cu^{2+}_{0.98})Nb_2O_6$. The negative Weiss temperature indicates that antiferromagnetic interactions between Cu^{2+} ions dominate the paramagnetic region. Indeed, an antiferromagnetic transition was observed as a cusp at $T_N = 12$ K under ZFC condition.

To investigate the antiferromagnetic transition in detail, I measured the specific heat. Figure 14(a) depicts temperature dependence of the total specific heat divided by temperature, $C_p T^{-1}$. The λ-type peak is observed around 10 K, indicating the long-range antiferromagnetic ordering. $C_p T^{-1}$ can be fitted with the following equation below 60 K:

$$C_p T^{-1} = \gamma + \beta_1 T^2 + \beta_2 T^4,$$

where γ is the Sommerfeld coefficient, β_1 and β_2 are the lattice contributions. I obtained γ = 0.131(5) J mol^{-1} K^{-2}, β_1 = 1.67(6) × 10^{-4} J mol^{-1} K^{-4} and β_2 = −1.7(2) × 10^{-8} J mol^{-1} K^{-6}. The β_1 value gives a Debye temperature, θ_D, of 472 K, close to those reported for other quadruple perovskites (407–543 K).[47–49] I comparatively measured the specific heat of the cubic Pv-$CuTa_2O_6$ and found that its γ value (0.168(4) J mol^{-1} K^{-2}) and θ_D value (410 K) are almost the same as those of Pv-$CuNb_2O_6$, respectively (Figure 16). The large values of γ are typically caused by strong electron correlations, as in heavy fermions.[50,51] However, considering Pv-CuB_2O_6 (B = Nb, Ta) compounds were not metallic, the competition of antiferromagnetic and ferromagnetic interactions would realize their apparently large γ values, as reported in other insulating materials.[52,53] I extracted the magnetic specific heat, C_m, by subtracting the lattice contributions from C_p. The estimated values of $C_m T^{-1}$ and $\Delta S = \int(C_m T^{-1})dT$ are provided in Figure 14(b). The ΔS value was estimated in the temperature range below 25 K, corresponding to the higher-temperature side of the λ-type peak in $C_p T^{-1}$. The obtained entropy (4.7 J mol^{-1} K^{-1}) was about 82 % of the ideal value for $Cu_{0.04}^{+}Cu_{0.98}^{2+}Nb_2O_6$ (5.65 J mol^{-1} K^{-1}), indicating that the long-range ordered magnetic structure is well established in the vicinity of the transition temperature. Similar phenomena, i.e., the antiferromagnetic transition around 10 K and the FC-ZFC separation below 10 K, were also observed in the cubic $Pm\overline{3}$ Pv-$CuTa_2O_6$ (Figure 15 and 16).

It has been reported that Pv-$ACu_3B_4O_{12}$ with a nonmagnetic d^0 cation in the B-site (e.g., $CaCu_3Ti_4O_{12}$,[41–43] $CdCu_3Ti_4O_{12}$,[43] $CaCu_3Zr_4O_{12}$[44] and cubic Pv-$CuTa_2O_6$[33]) shows antiferromagnetism due to the antiferromagnetic Cu-O-B-O-Cu super-exchange interaction. Pv-CuB_2O_6 (B = Nb, Ta) possesses Nb^{5+} (4d^0) or Ta^{5+} (5d^0) cation in the B-site, and thus, the antiferromagnetic super-exchange interactions are expected to work between the nearest Cu^{2+} spins. The separation between the FC and ZFC susceptibilities of Pv-CuB_2O_6 at low temperatures would come from the competition of antiferromagnetic super-exchange interaction with ferromagnetic direct-exchange interaction between the nearest Cu^{2+} spins. [44–46]

Further, I examine the dielectric properties of Pv-$CuNb_2O_6$. In the measurements, both surfaces of pelletized samples with a relative density of 87 % were polished and sputtered with gold. Figure 17 presents the frequency dependence of real and imaginary parts of the dielectric constant, ε', ε'', and loss tangent, tanδ, at room temperature. The value of ε' is about 10^2 at 1 MHz, but it increases with decreasing frequency and eventually reaches nearly 10^5. The frequency dependence of ε' and its order of magnitude resemble well those reported for the quenched cubic Pv-$CuTa_2O_6$.[30] The unusual dielectric constant enhancement in the low-frequency region for Pv-$CuNb_2O_6$ would be attributed to an extrinsic factor, where space charges and long-range hopping conductions significantly enhance the complex dielectric constant, especially in the low-frequency region. It should be mentioned that the same mechanism has been applied to Pv-$CuTa_2O_6$ to explain the enhancement of its dielectric constant.[26,27,30] I, therefore, analyzed dielectric constant with a model involving the complex conductivity, as employed in previous reports:[30,54,55]

$$\varepsilon' = \varepsilon_\infty + \frac{(\varepsilon_s - \varepsilon_\infty)[1 + (\omega\tau)^{1-\alpha}\sin(\frac{\alpha\pi}{2})]}{1 + 2(\omega\tau)^{1-\alpha}\sin(\frac{\alpha\pi}{2}) + (\omega\tau)^{2-2\alpha}} + \frac{\sigma''}{\varepsilon_0\omega^s} \ ,$$

$$\varepsilon'' = (\varepsilon_S - \varepsilon_\infty)\ \frac{(\omega\tau)^{1-\alpha}\cos(\frac{\alpha\pi}{2})}{1 + 2(\omega\tau)^{1-\alpha}\sin(\frac{\alpha\pi}{2}) + (\omega\tau)^{2-2\alpha}} + \frac{\sigma'}{\varepsilon_0\omega^s} \ ,$$

where ε_S is the static dielectric constant, ε_∞ is dielectric constant at the high-frequency limit, ω is the angular frequency, τ is the mean dielectric relaxation time, $0 < \alpha < 1$ is the distribution of the dielectric relaxation, σ' is the long-range carrier hopping conduction, σ'' is the parameter associated with space charges, and $0 < s < 1$ is the distribution of the carrier polarization relaxation. There is only a slight discrepancy between the fitted curves and experimental values. I obtained $\varepsilon_S = 6.0(2) \times 10^4$, $\varepsilon_\infty = 6.4(9) \times 10$, $\tau = 1.1(1) \times 10^{-1}$ s, $\alpha = 0.367(1)$, $\sigma' = 3.6667(2) \times 10^{-4}$ S m^{-1}, $\sigma'' = 2.31(4) \times 10^{-6}$ S m^{-1} and $s = 0.9958(1)$. The calculated σ'' value is in the same order of magnitude as that reported for cubic $Pm\overline{3}$ Pv-$CuTa_2O_6$ (1.15×10^{-6}),[47] indicating that the dielectric constant is enhanced by space charge to the same extent in both cases. On the contrary, the presence of conductive carriers leads to an increase in ε'', with the value of tanδ close to 100 in the low-frequency region.

The temperature dependence of ε' and tanδ for Pv-$CuNb_2O_6$ measured between 300 and 500 K at 1, 10, and 100 kHz are illustrated in Figure 18. One can see that the values of ε' and tanδ increased with increasing temperature for all measurement frequencies. According to our high-temperature SXRD experiment, Pv-$CuNb_2O_6$ was found not to exhibit any phase transitions at this temperature range (Figure 19). The enhancements in ε' and tanδ would be originating from thermally activated carriers, as observed in $CaCu_3Ti_4O_{12}$[16–19] and Pv-$CuTa_2O_6$.[26,27,30] One of the possible reasons for the space charge in Pv-$CuNb_2O_6$ is the formation of a core-shell structure due to the concentration distribution of Cu. When Cu is removed from Pv-$CuNbO_3$, Cu would not be completely released in the bulk but be entirely eliminated at grain boundaries. In such a way, Pv-$Cu_{1+x}Nb_2O_6$ in the bulk would exhibit semiconducting conduction due to the Cu^{+}-Cu^{2+} hopping mechanism, while $CuNb_2O_6$ at the grain boundary would be more insulating due to the suppressed hopping conduction. The difference in the conducting behaviours will lead the space charges.

High-dielectric constant materials have been intensively studied for high energy density storage and microelectronic applications.[56,57] Pv-$CuNb_2O_6$ may also become a subject of research in the future. However, since it suffers from large tanδ values, it is necessary to reduce the values for practical use by doping and so forth, as has been studied for $CaCu_3Ti_4O_{12}$.[58–60]

5.3 Summary of This Chapter

A novel A-site deficient quadruple perovskite-type oxide, $CuNb_2O_6$, has been successfully prepared by high-pressure synthesis and post-annealing at ambient pressure, representing a rare example of "hard-soft" chemistry with cation deinsertion. It forms a non-centrosymmetric cubic $I23$ structure. My study revealed that an antiferromagnetic transition occurs at T_N = 12 K. I also find that the dielectric constant was enhanced in Pv-$CuNb_2O_6$ by space charges as in the related quadruple perovskite-type compounds, $CaCu_3Ti_4O_{12}$ and $CuTa_2O_6$.

5.4 Tables and Figures

Table 1. Refined structural parameters of Pv-$CuNb_2O_6$ at 300 K

atom	site	g	x	y	z	U / Å^2
Cu1	6*b*	0.680(2)	0	1/2	1/2	0.0049(3)
Nb1	8*c*	1	0.25970(4)	= *x*	= *x*	0.0078(2)
O1	24*f*	1	0.9978(6)	0.3038(4)	0.1834(4)	0.0142(8)

Space group: *I*23 (No. 197), $Z = 4$, $Cu_{1.02}Nb_2O_6$ (fw = 346.67 g mol^{-1}), $a = 7.52516(3)$ Å, $V = 426.135(3)$ Å^3, $R_{wp} = 8.65$ % and $R_B = 5.46$ %.

Table 2. Refined composition, crystal symmetry, lattice volume, bond lengths, bond angles, and BVS for $CuNb_2O_6$, and those for $CuTa_2O_6$ and $LiCuNb_3O_9$, as previously reported.[24,25]

	$CuNb_2O_6$		**$CuTa_2O_6$**		**$LiCuNb_3O_9$**	
Refined composition	$Cu_{1.02}Nb_2O_6$		$Cu_{1.01}Ta_2O_6$		$LiCuNb_3O_9$	
Crystal symmetry	cubic *I*23		cubic *Pm*3		cubic *I*23	
V /Å^3	426.13		419.69		426.72	
Bond length /Å	Cu1-O1	2.021(4) × 4	Cu1-O2	2.033(3) × 4	Cu1-O1	2.02(2) × 4
			Cu2-O1	2.033(3) × 4		
	Nb1-O1	1.903(5) × 3	Ta1-O1	1.974(2) × 3	Nb1-O1	1.92(3) × 3
	-O1	2.079(5) × 3	-O2	1.977(2) × 3	-O1	2.07(3) × 3
Bond angles / °	Nb1-O1-Nb1	142.2(2)	Ta1-O1-Ta1	143.0(2)	Nb1-O1-Nb1	142.2(10)
			Ta1-O2-Ta1	142.4(2)		
BVS	Cu1	1.9	Cu1	1.9	Cu1	1.6
			Cu2	1.9		
	Nb1	5.0	Ta1	5.2	Nb1	4.9
References	This work		24		25	

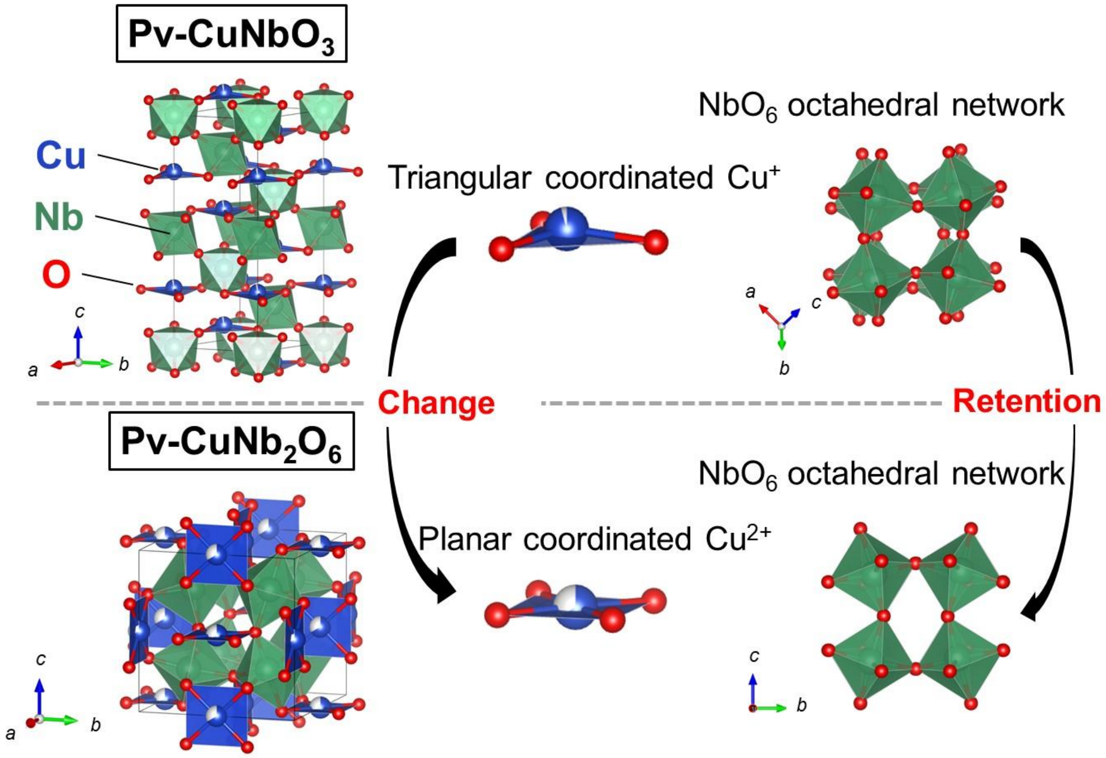

Figure 1. Crystal structures of Pv-CuNbO$_3$ (upper) and Pv-CuNb$_2$O$_6$ (lower), highlighting that the topochemical cation deinsertion alters the local environment around Cu ions from triangular coordination into square-planar coordination while maintaining the NbO$_6$ octahedral network.

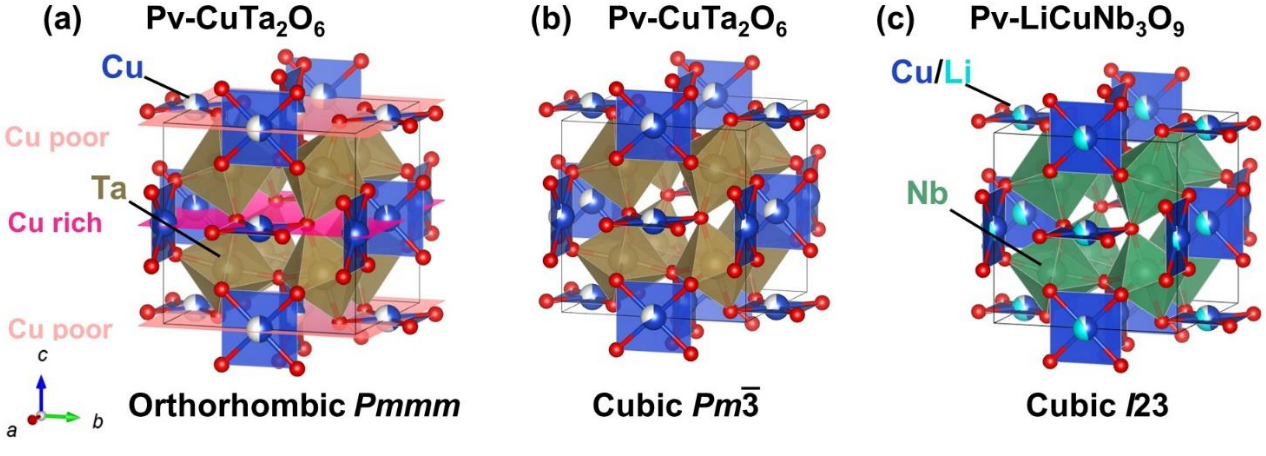

Figure 2. Crystal structures of (a) orthorhombic Pv-CuTa$_2$O$_6$ with Cu-Cu layered ordering, (b) cubic Pv-CuTa$_2$O$_6$ without Cu-Cu layered ordering, and (c) cubic Pv-LiCuNb$_3$O$_9$.

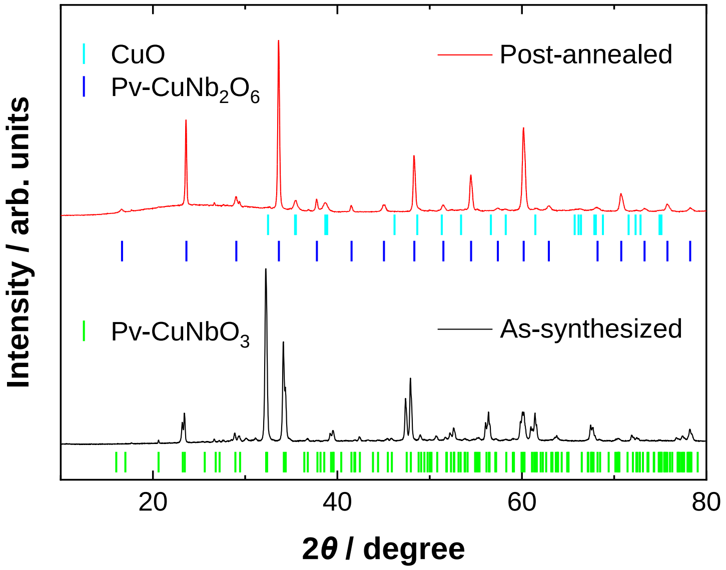

Figure 3. Laboratory XRD patterns (Cu Kα) at room temperature of high-pressure-synthesized CuNbO$_3$ (black line) and that post-annealed at 773 K (red line). The light blue, purple, and light green ticks correspond to the Bragg positions for CuO, Pv-CuNb$_2$O$_6$, and Pv-CuNbO$_3$, respectively.

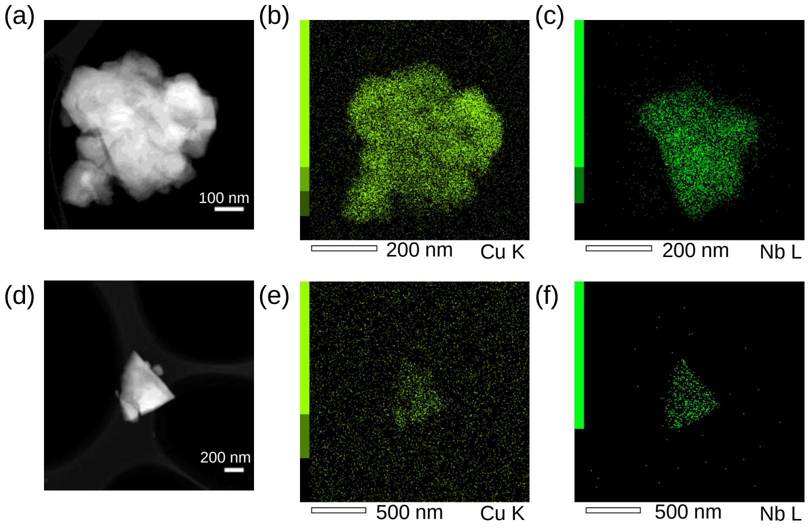

Figure 4. HAADF-STEM images for the post-annealed mixture grains of Pv-CuNb$_2$O$_6$ and CuO. (a) and (d) represent the appearance of grain 1 and grain 2, respectively. (b) Cu and (c) Nb EDX mapping for grain 1, and (e) Cu and (f) Nb EDX mapping for grain 2. The association of the smaller grains containing only Cu atom (CuO) on the larger grains containing both Cu and Nb atoms (Pv-CuNb$_2$O$_6$) is observed.

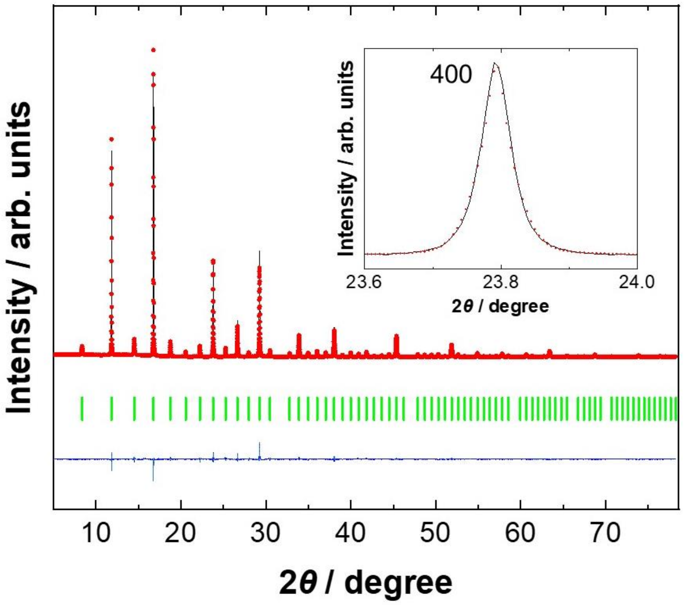

Figure 5. Rietveld refinements against the SXRD pattern (λ = 0.75003 Å) of Pv-$CuNb_2O_6$ at room temperature, showing the observed (red circles) and calculated (solid black lines) profiles. The solid blue lines represent the difference between the observed and calculated profiles. The green ticks correspond to the positions of the allowed Bragg reflections. The inset is an enlarged view of 400 peak, indicating no peak splitting.

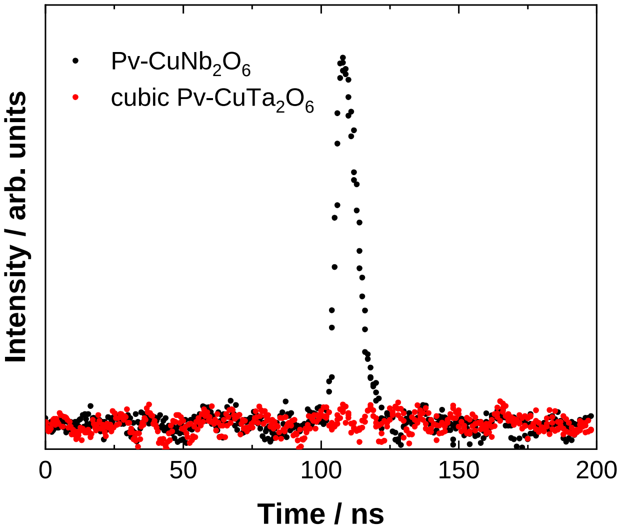

Figure 6. Oscilloscope traces of the SHG signals for Pv-$CuNb_2O_6$ and quenched cubic Pv-$CuTa_2O_6$ (centrosymmetric reference) at room temperature.

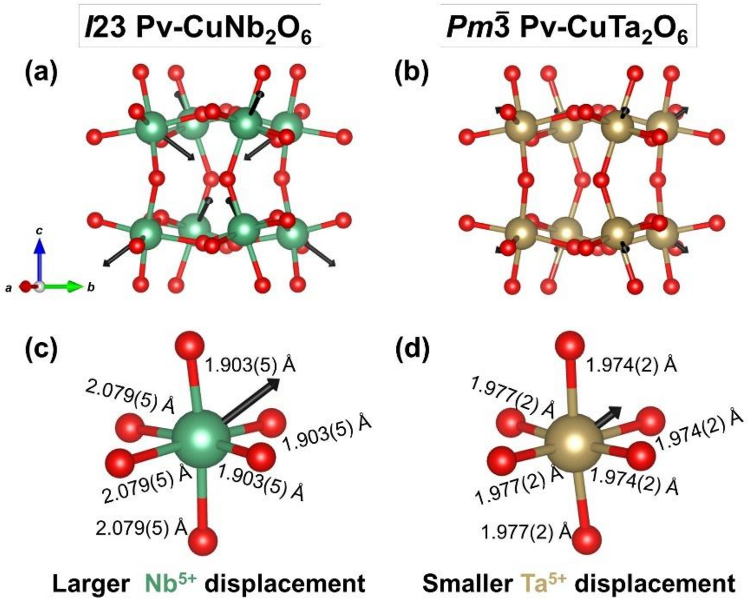

Figure 7. Local environments of the B-site cations in (a), (c) *I*23 Pv-CuNb$_2$O$_6$ and (b), (d) $Pm\bar{3}$ Pv-CuTa$_2$O$_6$. The black arrows indicate the off-center B-site cations displacements. The directions of the eight B-site cations displacements are displayed in the unit cell of (a) Pv-CuNb$_2$O$_6$ and (b) Pv-CuTa$_2$O$_6$. The magnitude of the B-site cations displacements and the B-O bond lengths within the BO$_6$ octahedra are shown for (c) Pv-CuNb$_2$O$_6$ and (d) Pv-CuTa$_2$O$_6$.

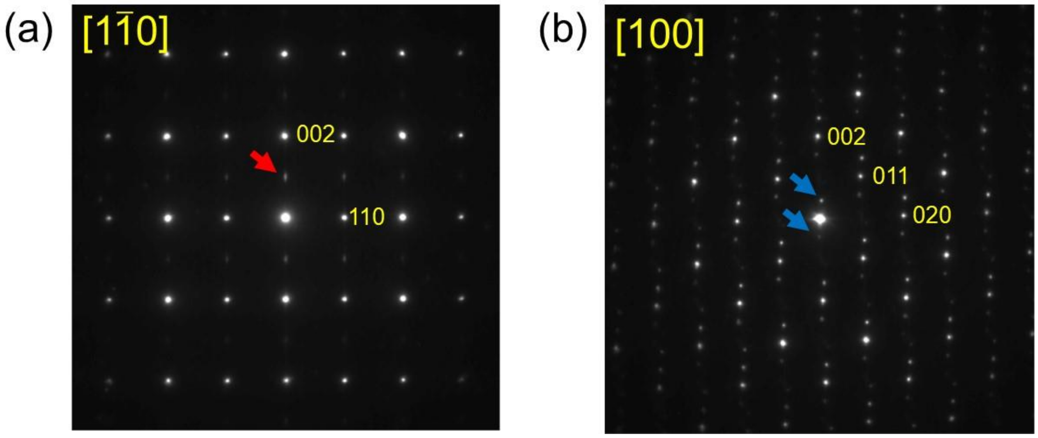

Figure 8. ED patterns of Pv-CuNb$_2$O$_6$ at room temperature taken along (a) [1$\bar{1}$0] and (b) [100]. Representative indices are shown just to the right of the corresponding spots. The red arrow in (a) and blue arrows in (b) represent satellite reflections

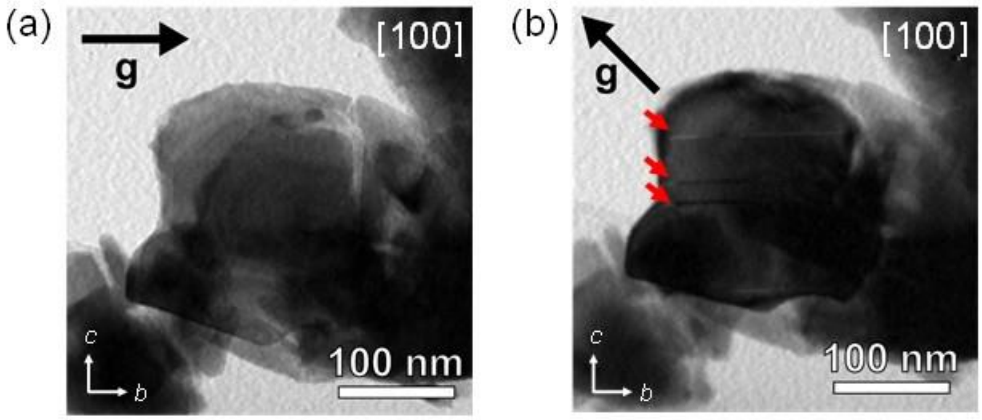

Figure 9. TEM BF images of [100]-oriented Pv-CuNb$_2$O$_6$. The diffraction vector, g, is set to in-plane (a) [010] and (b) [0$\bar{1}$1]. The red arrows in (b) represent the domain structures. Only when observed with $g = 0\bar{1}1$, domain structures perpendicular to the c-axis (red arrows in (b)) can be observed.

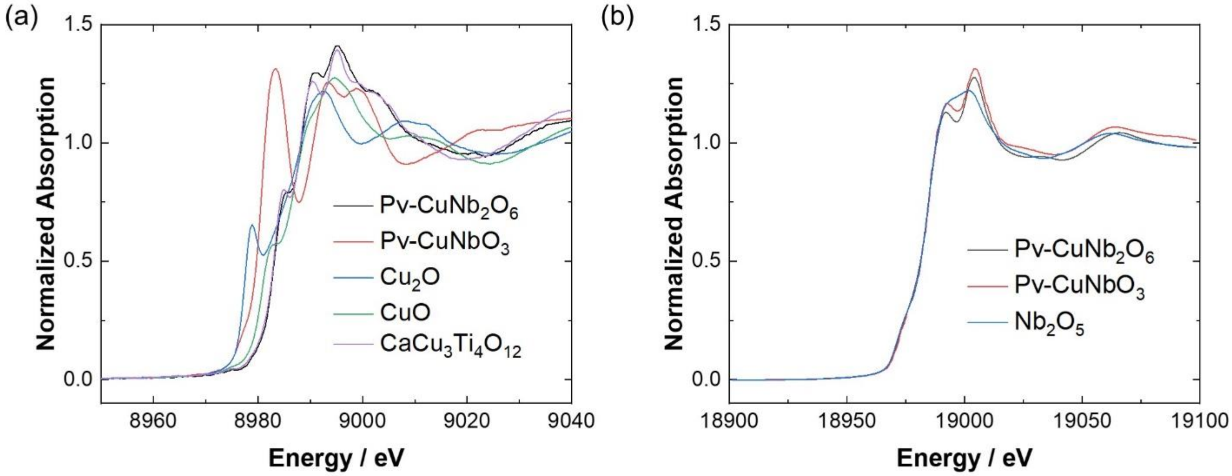

Figure 10. (a) Experimental Cu K-edge XANES spectrum at room temperature of Pv-CuNb$_2$O$_6$ (black) in comparison with those of Pv-CuNbO$_3$ (red), Cu$_2$O (blue), CuO (light green), and CaCu$_3$Ti$_4$O$_{12}$ (purple). (b) Experimental Nb K-edge XANES spectrum at room temperature of PvCuNb$_2$O$_6$ (black) in comparison with those of Pv-CuNbO$_3$ (red) and Nb$_2$O$_5$ (blue)

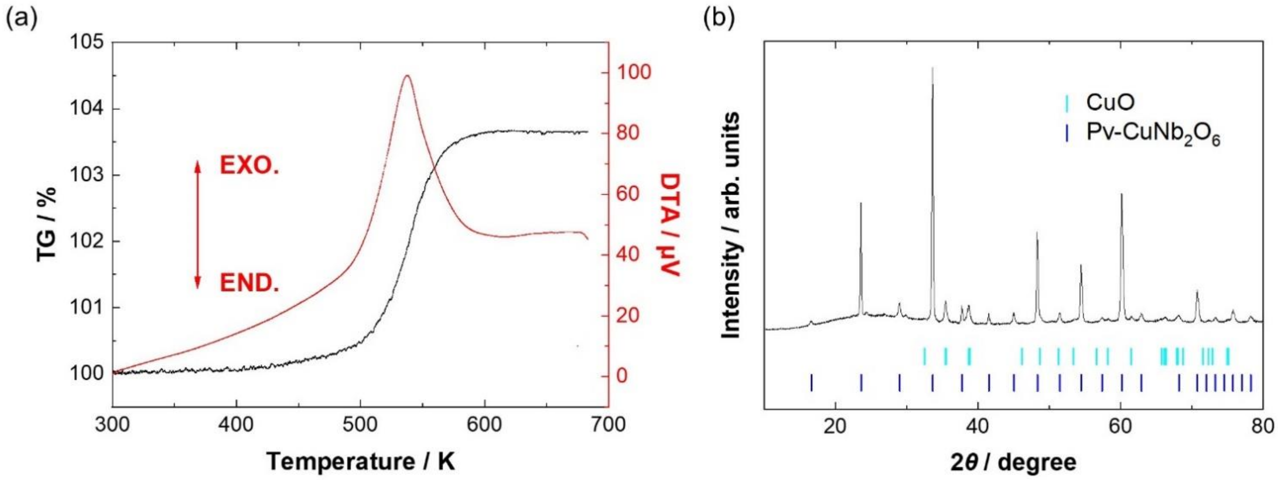

Figure 11. (a) TG-DTA curves for Pv-CuNbO$_3$ between 300 and 673 K and (b) laboratory XRD pattern (CuKα) measured at room temperature after heating of high-pressure-synthesized Pv-CuNbO$_3$ to 673 K in the TG-DTA experiment. The light blue and blue ticks correspond to the Bragg positions for CuO and Pv-CuNb$_2$O$_6$, respectively.

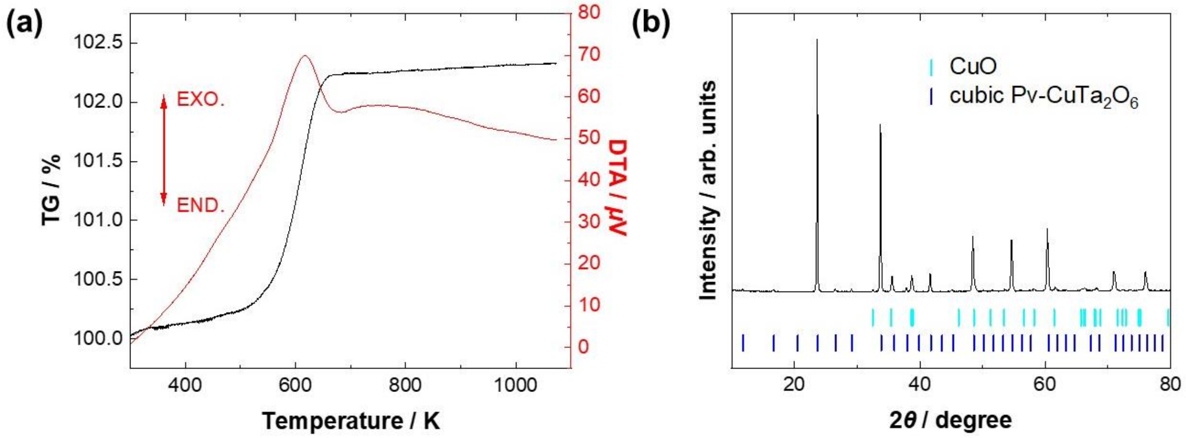

Figure 12. (a) TG-DTA curves measured between 300 and 1073 K for high-pressure-synthesized Pv-CuTaO$_3$. The exothermic peak with ~2 % weight gain (estimated by subtracting background level) was observed at around 600 K, corresponding to the topochemical reaction: $CuTaO_3 + 0.19O_2 \rightarrow 0.38CuO + Cu_{1.24}Ta_2O_6$. (b) Laboratory XRD pattern (CuKα) measured at room temperature after heating of high-pressure-synthesized Pv-CuTaO$_3$ to 1073 K in the TG-DTA experiment. The light blue and blue ticks correspond to the Bragg positions for CuO and Pv-CuTa$_2$O$_6$, respectively.

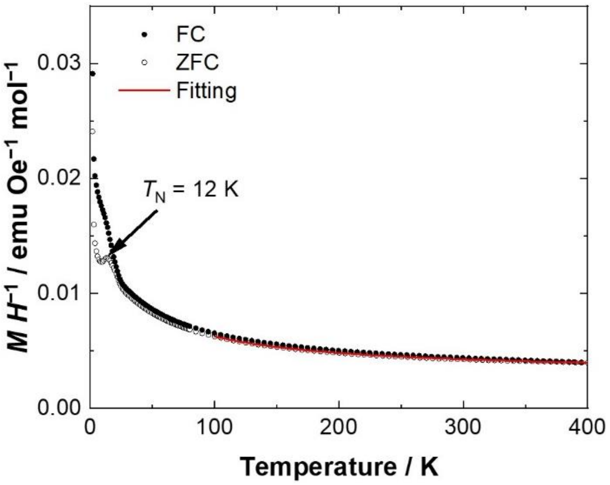

Figure 13. Temperature dependence of magnetic susceptibility, $\chi = M\ H^{-1}$, of Pv-CuNb$_2$O$_6$ measured at H = 100 Oe after field cooling (FC) and zero-field cooling (ZFC). The black filled and open circles represent the observed FC and ZFC data, whereas the solid red line is the fitted curve based on the Curie-Weiss law.

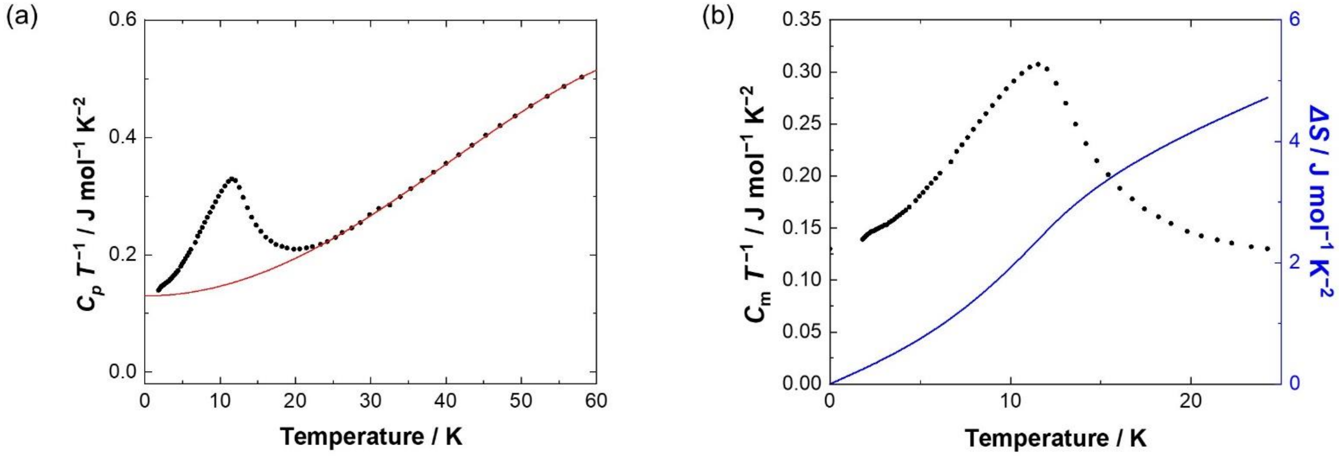

Figure 14. (a) The specific heat divided by temperature, $C_p\ T^{-1}$ (black dots), and the fitting results of the lattice specific heat for Pv-CuNb$_2$O$_6$ (solid red line). (b) The magnetic specific heat divided by temperature, $C_m\ T^{-1}$ (black dots), and the magnetic entropy (solid blue line).

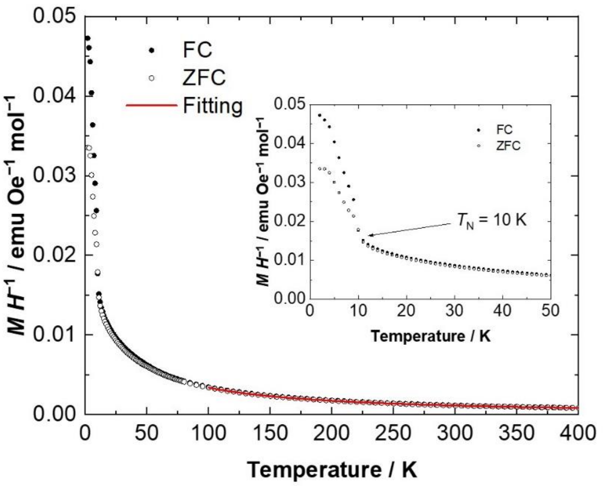

Figure 15. Temperature dependence of magnetic susceptibility, $\chi = M H^{-1}$, of the quenched cubic Pv-$CuTa_2O_6$ measured at H = 100 Oe after field cooling (FC) and zero-field cooling (ZFC). The inset features a magnified view near the antiferromagnetic transition temperature. The black filled and open circles represent the observed FC and ZFC data, whereas the solid red line is the fitted curve based on the Curie-Weiss law, $\chi = \chi_0 + C / (T - \theta_W)$. Following parameters were obtained: $\chi_0 = -1.49(6) \times 10^{-4}$ emu Oe^{-1} mol^{-1}, C = 0.402(3) emu K Oe^{-1} mol^{-1} and $\theta_W = -13.8(6)$ K.

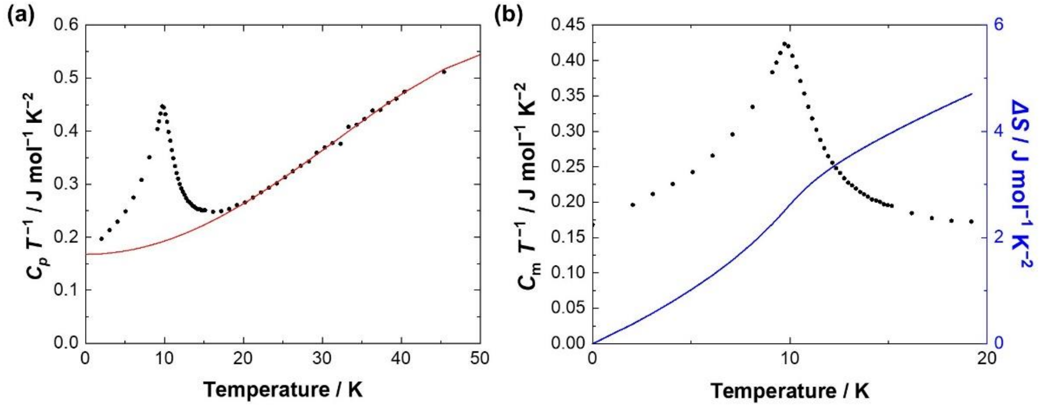

Figure 16. (a) The specific heat divided by temperature, $C_p T^{-1}$ (black dots), and the fitting results of the lattice specific heat for quenched cubic Pv-$CuTa_2O_6$ (solid red line), based on the following equation below 50 K, $C/T = \gamma + \beta_1 T^2 + \beta_2 T^4$. (b) The magnetic specific heat divided by temperature, $C_m T^{-1}$ (black dots), and the magnetic entropy (solid blue line) below 20 K. Following parameters were obtained: γ = 0.168(4) J mol^{-1} K^{-2}, $\beta_1 = 2.55(7) \times 10^{-4}$ J mol^{-1} K^{-4} and $\beta_2 = -4.2(2) \times 10^{-8}$ J mol^{-1} K^{-6} and ΔS = 4.7 J mol^{-1} K^{-1}.

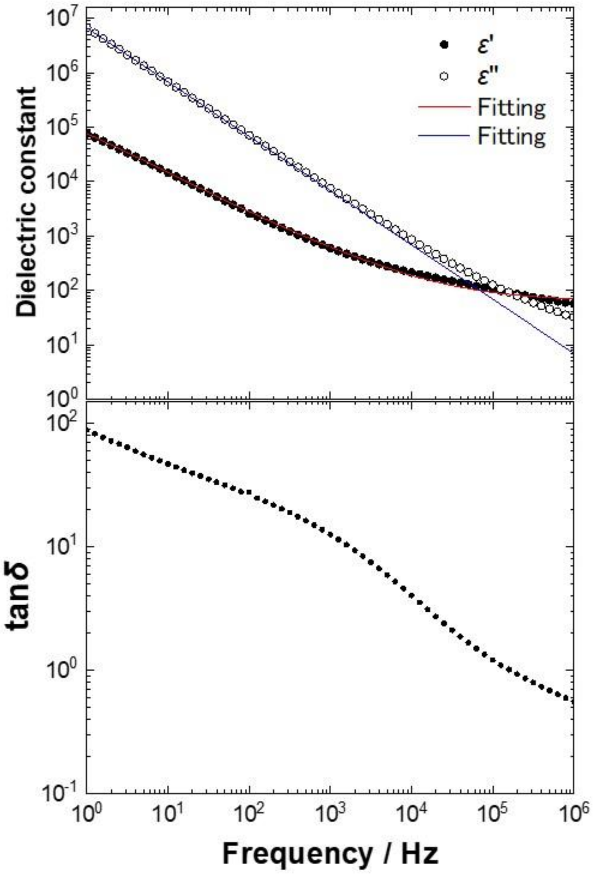

Figure 17. Frequency-dependent real and imaginary parts of the dielectric constant, ε' and ε'' (black filled and open circles in the upper panel), and loss tangent, tanδ (black dots in the lower panel), of Pv-$CuNb_2O_6$ at room temperature. The solid red and blue lines in the upper panel are the fitted curve based on a model involving the contribution of complex conductivity.

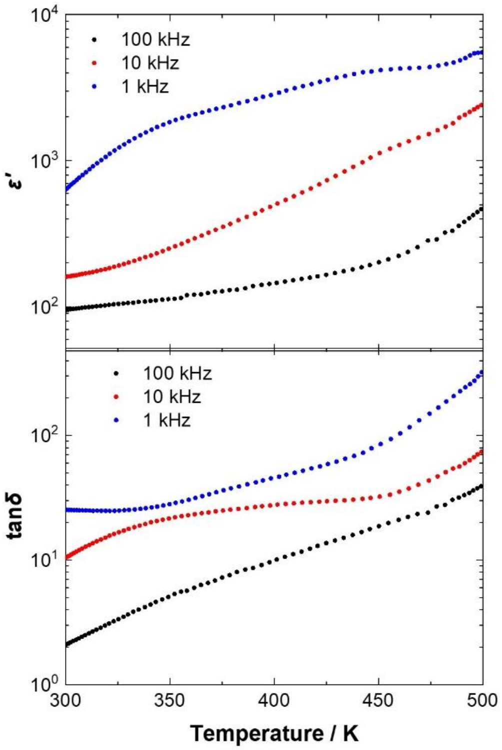

Figure 18. A temperature-dependent real part of the dielectric constant, *ε*' (the upper panel), and loss tangent, tan*δ* (the lower panel), between 300 and 500 K. The blue, red, and black filled circles represent data measured at 1, 10 and 100 kHz.

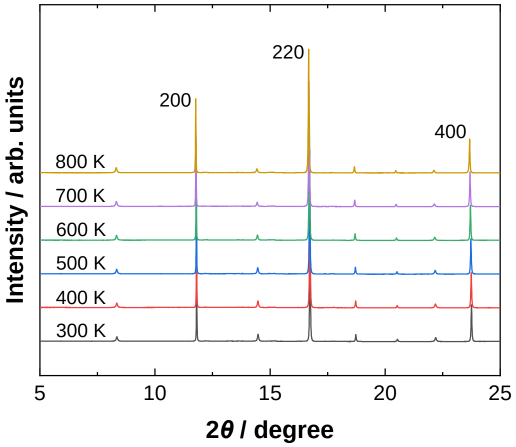

Figure 19. Temperature evolution of SXRD patterns (λ = 0.77443 Å) of Pv-$CuNb_2O_6$ in the temperature range of 300 to 800 K.

5.5 References

(1) Schaak, R. E.; Mallouk, T. E. Perovskites by Design: A Toolbox of Solid-State Reactions. *Chem. Mater.* **2002**, *14* (4), 1455–1471.

(2) Kageyama, H.; Hayashi, K.; Maeda, K.; Attfield, J. P.; Hiroi, Z.; Rondinelli, J. M.; Poeppelmeier, K. R. Expanding Frontiers in Materials Chemistry and Physics with Multiple Anions. *Nat. Commun.* **2018**, *9* (1), 772.

(3) Gupta, A. S.; Akamatsu, H.; Strayer, M. E.; Lei, S.; Kuge, T.; Fujita, K.; dela Cruz, C.; Togo, A.; Tanaka, I.; Tanaka, K.; Mallouk, T. E.; Gopalan, V. Improper Inversion Symmetry Breaking and Piezoelectricity through Oxygen Octahedral Rotations in Layered Perovskite Family, $LiRTiO_4$(R= Rare Earths). *Adv. Electron. Mater.* **2016**, *2* (1), 1500196.

(4) Zhang, H.; Gao, S.; Zhang, Q.; Wu, J.; Liang, J.; Dong, C.; Gu, L.; Dong, S.; Sun, J.; Liao, F.; Lin, J.; Zou, R.; Li, G. Topotactic Reduction toward a Noncentrosymmetric Deficient Perovskite $Tb_{0.50}Ca_{0.50}Mn_{0.96}O_{2.37}$ with Ordered Mn Vacancies and Piezoelectric Behavior. *Chem. Mater.* **2017**, *29* (22), 9840–9850.

(5) Sturza, M.; Daviero-Minaud, S.; Kabbour, H.; Gardoll, O.; Mentré, O. Fluorination of Iron Hexagonal Perovskites Promoting Low Temperature Oxygen Mobility. *Chem. Mater.* **2010**, *22* (24), 6726–6735.

(6) Kobayashi, Y.; Hernandez, O. J.; Sakaguchi, T.; Yajima, T.; Roisnel, T.; Tsujimoto, Y.; Morita, M.; Noda, Y.; Mogami, Y.; Kitada, A.; Ohkura, M.; Hosokawa, S.; Li, Z.; Hayashi, K.; Kusano, Y.; Kim, J. E.; Tsuji, N.; Fujiwara, A.; Matsushita, Y.; Yoshimura, K.; Takegoshi, K.; Inoue, M.; Takano, M.; Kageyama, H. An Oxyhydride of $BaTiO_3$ Exhibiting Hydride Exchange and Electronic Conductivity. *Nat. Mater.* **2012**, *11* (6), 507–511.

(7) Arévalo-López, A. M.; Rodgers, J. A.; Senn, M. S.; Sher, F.; Farnham, J.; Gibbs, W.; Attfield, J. P. "Hard-Soft" Synthesis of $SrCrO_{3-\delta}$ Superstructure Phases. *Angew. Chem. Int. Ed.* **2012**, *51* (43), 10791–10794.

(8) Arevalo-Lopez, A. M.; Liang, B.; Senn, M. S.; Murray, C.; Tang, C.; Attfield, J. P. Hard–Soft Synthesis of a New Series of Vacancy-Ordered Perovskites, $CaCrO_{3-\delta}$. *J. Mater. Chem. C* **2014**, *2* (44), 9364–9367.

(9) Su, Y.; Tsujimoto, Y.; Fujii, K.; Masubuchi, Y.; Ohata, H.; Iwai, H.; Yashima, M.; Yamaura, K. Stepwise Topochemical Fluorination of $SrCrO_3$ Perovskite via a Super-Structured Oxide. *Chem.*

Commun. **2019**, *55* (50), 7239–7242.

(10) Juillerat, C. A.; Tsujimoto, Y.; Chikamatsu, A.; Masubuchi, Y.; Hasegawa, T.; Yamaura, K. Fluorination and Reduction of $CaCrO_3$ by Topochemical Methods. *Dalton Trans.* **2020**, *49* (6), 1997–2003.

(11) Felten, E. J. The Preparation of $CuNb_2O_6$ and $CuTa_2O_6$. *J. Inorg. Nucl. Chem.* **1967**, *29* (4), 1168–1171.

(12) Wahlström, E.; Marinder, B.-O. Phase Analysis Studies in the Copper-Niobium-Oxygen System. *Inorg. Nucl. Chem. Lett.* **1977**, *13* (11), 559–564.

(13) Drew, M. G. B.; Hobson, R. J.; Padayatchy, V. T. Synthesis, Single-Crystal Structure and Magnetic Properties of Orthorhombic $CuNb_2O_6$. *J. Mater. Chem.* **1993**, *3* (8), 889–892.

(14) Drew, M. G. B.; Hobson, R. J.; Padayatchy, V. T. Synthesis, Structure and Magnetic Properties of Monoclinic CuNb2O6 and the Electronic Spectra of Both Polymorphs of $CuNb_2O_6$. *J. Mater. Chem.* **1995**, *5* (11), 1779–1783.

(15) Kumada, N.; Kinomura, N. Topochemical Preparation of $LiNbO_3$ Type $Li_{1-x}Cu_xNbO_3$ from $CuNb_2O_6$. *Mater. Res. Bull.* **1990**, *25* (7), 881–889.

(16) Ramirez, A. P.; Subramanian, M. A.; Gardel, M.; Blumberg, G.; Li, D.; Vogt, T.; Shapiro, S. M. Giant Dielectric Constant Response in a Copper-Titanate. *Solid State Commun.* **2000**, *115* (5), 217–220.

(17) Subramanian, M. A.; Li, D.; Duan, N.; Reisner, B. A.; Sleight, A. W. High Dielectric Constant in $ACu_3Ti_4O_{12}$ and $ACu_3Ti_3FeO_{12}$ Phases. *J. Solid State Chem.* **2000**, *151* (2), 323–325.

(18) Homes, C. C.; Vogt, T.; Shapiro, S. M.; Wakimoto, S.; Ramirez, A. P. Optical Response of High-Dielectric-Constant Perovskite-Related Oxide. *Science* **2001**, *293* (5530), 673–676.

(19) Sinclair, D. C.; Adams, T. B.; Morrison, F. D.; West, A. R. $CaCu_3Ti_4O_{12}$: One-Step Internal Barrier Layer Capacitor. *Appl. Phys. Lett.* **2002**, *80* (12), 2153–2155.

(20) Lunkenheimer, P.; Fichtl, R.; Ebbinghaus, S. G.; Loidl, A. Nonintrinsic Origin of the Colossal Dielectric Constants in $CaCu_3Ti_4O_{12}$. *Phys. Rev. B* **2004**, *70* (17), 1–4.

(21) Singh, L.; Rai, U. S.; Mandal, K. D.; Singh, N. B. Progress in the Growth of $CaCu_3Ti_4O_{12}$ and Related Functional Dielectric Perovskites. *Prog. Cryst. Growth Charact. Mater.* **2014**, *60* (2), 15–62.

(22) Ahmadipour, M.; Ain, M. F.; Ahmad, Z. A. A Short Review on Copper Calcium Titanate (CCTO) Electroceramic: Synthesis, Dielectric Properties, Film Deposition, and Sensing Application.

Nanomicro Lett **2016**, *8* (4), 291–311.

(23) Reinen, D.; Propach, V. Verbindungen Mit Cu^{2+}-Ionen Auf Den a-Plaetzen von Perowskiten ABO_3. *Inorg. Nucl. Chem. Lett.* **1971**, *7* (7), 569–572.

(24) Propach, V. Kristallstruktur von $Ca_{0.5}Cu_{1.5}Ti_2O_6$, $Cu_{1.5}TaTiO_6$ Und $CuTa_2O_6$. Das Spektroskopische Verhalten von Cu^{2+}-Ionen in Kuboktaedrischer Umgebung. *Z. Anorg. Allg. Chem.* **1977**, *435* (1), 161–171.

(25) Sato, M.; Hama, Y. Structure of New Perovskite-Related Compounds, $LiCuM_3O_9$ (M = Nb, Ta). *J. Mater. Chem.* **1993**, *3* (3), 233–236.

(26) Renner, B.; Lunkenheimer, P.; Schetter, M.; Loidl, A.; Reller, A.; Ebbinghaus, S. G. Dielectric Behavior of Copper Tantalum Oxide. *J. Appl. Phys.* **2004**, *96* (8), 4400–4404.

(27) Szwagierczak, D.; Kulawik, J. Sintering and Dielectric Properties of $Cu_2Ta_4O_{12}$ Ceramics. *J. Eur. Ceram. Soc.* **2008**, *28* (10), 2075–2083.

(28) Chen, X.; Ma, D.; He, F.; Huang, G.; Zhou, H. Origin of Giant Dielectric Response in $LiCuNb_3O_9$ Distorted Perovskite Ceramics. *J. Eur. Ceram. Soc.* **2017**, *37* (4), 1861–1864.

(29) Gao, D.; Xie, J.; Jiang, X.-M.; Liu, H.; Li, G.; Wang, J.; Zhang, L.; Xiong, F.; Hu, W. Colossal-Permittivity Behaviors in A-Site Distorted Double-Perovskite $LiCuNb_3O_9$ with Correlated Magnetoelectric Effect and Variable-Range Hopping. *ACS Appl. Electron. Mater.* **2019**, *1* (1), 64–74.

(30) Chen, K.; Liu, M.; Li, G.; Wang, J.; Lei, X.; Yu, Q.; Hu, C.; Li, Z.; Liu, L. Enhancement of Dielectric Response by the Interaction of Point Defect and Grain Boundary in Copper Tantalate Oxides. *Ceram. Int.* **2021**, *47* (11), 16178–16185.

(31) Ahmed, R.; Wang, J.; Si, R. J.; Rehman, S. ur; Li, T.; Bi, H.; Yu, Y.; Li, Q. J.; Li, Y. D.; Huang, S. G.; Guo, Y. M.; Wang, C. C. Jahn-Teller Assisted Polaronic Electron Hopping in $LiCuNb_3O_9$. *J. Eur. Ceram. Soc.* **2021**, *41* (4), 2625–2632.

(32) Gao, D.; Xie, J.; Wang, J.; Hu, W. B-Site Octahedral Bridge and A-Site Polyvalent Cu Cations Related Electron Hopping in $LiCuNb_3O_9$-Based Colossal Permittivity Materials. *J. Mater. Chem. C Mater. Opt. Electron. Devices* **2021**.

(33) Ebbinghaus, S. G. Influence of Composition and Thermal Treatment on the Properties of $Cu_{2+x}Ta_4O_{12+\delta}$. *Prog. Solid State Chem.* **2007**, *35* (2), 421–431.

(34) Kunz, M.; Brown, I. D. Out-of-Center Distortions around Octahedrally Coordinated D0 Transition Metals. *J. Solid State Chem.* **1995**, *115* (2), 395–406.

(35) Gagné, O. C.; Hawthorne, F. C. Bond-Length Distributions for Ions Bonded to Oxygen: Results for the Transition Metals and Quantification of the Factors Underlying Bond-Length Variation in Inorganic Solids. *IUCrJ* **2020**, *7* (Pt 4), 581–629.

(36) Brese, N. E.; O'Keeffe, M. Bond-Valence Parameters for Solids. *Acta Crystallogr. B* **1991**, *47* (2), 192–197.

(37) Schmidt, R.; Stennett, M. C.; Hyatt, N. C.; Pokorny, J.; Prado-Gonjal, J.; Li, M.; Sinclair, D. C. Effects of Sintering Temperature on the Internal Barrier Layer Capacitor (IBLC) Structure in $CaCu_3Ti_4O_{12}$ (CCTO) Ceramics. *J. Eur. Ceram. Soc.* **2012**, *32* (12), 3313–3323.

(38) Shimizu, K.-I.; Maeshima, H.; Yoshida, H.; Satsuma, A.; Hattori, T. Ligand Field Effect on the Chemical Shift in XANES Spectra of Cu(II) Compounds. *Phys. Chem. Chem. Phys.* **2001**, *3* (5), 862–866.

(39) Yamada, I.; Odake, T.; Tanaka, A.; Okazaki, Y.; Toda, F.; Ishii, Y.; Taniguchi, T.; Kawaguchi, S.; Hariki, A. A Sequential Electron Doping for Quadruple Perovskite Oxides $ACu_3Co_4O_{12}$ (A = Ca, Y, Ce). *Inorg. Chem.* **2020**, *59* (13), 8699–8706.

(40) Sleight, A. W.; Prewitt, C. T. Preparation of $CuNbO_3$ and $CuTaO_3$ at High Pressure. *Mater. Res. Bull.* **1970**, *5* (3), 207–211.

(41) Koitzsch, A.; Blumberg, G.; Gozar, A.; Dennis, B.; Ramirez, A. P.; Trebst, S.; Wakimoto, S. Antiferromagnetism in $CaCu_3Ti_4O_{12}$ Studied by Magnetic Raman Spectroscopy. *Phys. Rev. B* **2002**, *65* (5), 052406.

(42) Kim, Y. J.; Wakimoto, S.; Shapiro, S. M.; Gehring, P. M.; Ramirez, A. P. Neutron Scattering Study of Antiferromagnetic Order in $CaCu_3Ti_4O_{12}$. *Solid State Commun.* **2002**, *121* (11), 625–629.

(43) Pires, M. A.; Israel, C.; Iwamoto, W.; Urbano, R. R.; Agüero, O.; Torriani, I.; Rettori, C.; Pagliuso, P. G.; Walmsley, L.; Le, Z.; Cohn, J. L.; Oseroff, S. B. Role of Oxygen Vacancies in the Magnetic and Dielectric Properties of the High-Dielectric-Constant System $CaCu_3Ti_4O_{12}$: An Electron-Spin Resonance Study. *Phys. Rev. B* **2006**, *73* (22), 224404.

(44) Toyoda, M.; Yamauchi, K.; Oguchi, T. Ab Initio Study of Magnetic Coupling in $CaCu_3B_4O_{12}$ (Ti, Ge, Zr, and Sn). *Phys. Rev. B* **2013**, *87* (22), 224430.

(45) Shiraki, H.; Saito, T.; Yamada, T.; Tsujimoto, M.; Azuma, M.; Kurata, H.; Isoda, S.; Takano, M.; Shimakawa, Y. Ferromagnetic Cuprates $CaCu_3Ge_4O_{12}$ and $CaCu_3Sn_4O_{12}$ with A-Site Ordered Perovskite Structure. *Phys. Rev. B* **2007**, *76* (14), 140403.

(46) Shimakawa, Y.; Shiraki, H.; Saito, T. Unusual Ferromagnetic-to-Antiferromagnetic-to-Ferromagnetic Transitions in Cu^{2+} ($S = 1/2$) Cubic Spin Lattice of A-Site Ordered Perovskites. *J. Phys. Soc. Jpn.* **2008**, *77* (11), 113702–113702.

(47) Levchenko, A. A.; Marchin, L.; Moriya, Y.; Kawaji, H.; Atake, T.; Guillemet-Fritsch, S.; Durand, B.; Navrotsky, A. Calorimetric Study of $CaCu_3Ti_4O_{12}$, a Ceramic with Giant Permittivity. *J. Mater. Res.* **2008**, *23* (6), 1522–1531.

(48) Tanaka, S.; Shimazui, N.; Takatsu, H.; Yonezawa, S.; Maeno, Y. Heavy-Mass Behavior of Ordered Perovskites $ACu_3Ru_4O_{12}$ (A=Na, Ca, La). *J. Phys. Soc. Jpn.* **2009**, *78* (2), 024706–024706.

(49) Akizuki, Y.; Yamada, I.; Fujita, K.; Taga, K.; Kawakami, T.; Mizumaki, M.; Tanaka, K. Rattling in the Quadruple Perovskite $CuCu_3V_4O_{12}$. *Angew. Chem. Int. Ed.* **2015**, *54* (37), 10870–10874.

(50) Andres, K.; Graebner, J. E.; Ott, H. R. 4f-Virtual-Bound-State Formation in $CeAl_3$ at Low Temperatures. *Phys. Rev. Lett.* **1975**, *35* (26), 1779–1782.

(51) Stewart, G. R.; Fisk, Z.; Wire, M. S. New Ce Heavy-Fermion System: $CeCu_6$. *Phys. Rev. B* **1984**, *30* (1), 482–484.

(52) Zhang, S.-Y.; He, Z.-Z.; Yang, M.; Guo, W.-B.; Tang, Y.-Y. Synthesis and Magnetic Properties of a New Polymorph of $Cu_2(VO_4)(OH)$ with a Quasi-2D Layer Structure. *Dalton Trans.* **2014**, *43* (9), 3521–3527.

(53) Shon, W.; Rhyee, J.-S.; Jin, Y.; Kim, S.-J. Magnetic Polaron and Unconventional Magnetotransport Properties of the Single-Crystalline Compound $EuBiTe_3$. *Phys. Rev. B* **2019**, *100* (2), 024433.

(54) Abdelkafi, Z.; Abdelmoula, N.; Khemakhem, H.; Bidault, O.; Maglione, M. Dielectric Relaxation in $BaTi_{0.85}(Fe_{1/2}Nb_{1/2})_{0.15}O_3$ Perovskite Ceramic. *J. Appl. Phys.* **2006**, *100* (11), 114111.

(55) Liu, L.; Ren, S.; Liu, J.; Han, F.; Zhang, J.; Peng, B.; Wang, D.; Bokov, A. A.; Ye, Z.-G. Localized Polarons and Conductive Charge Carriers: Understanding $CaCu_3Ti_4O_{12}$ over a Broad Temperature Range. *Phys. Rev. B* **2019**, *99* (9), 094110.

(56) Pandey, R. K.; Stapleton, W. A.; Tate, J.; Bandyopadhyay, A. K.; Sutanto, I.; Sprissler, S.; Lin, S. Applications of CCTO Supercapacitor in Energy Storage and Electronics. *AIP Adv.* **2013**, *3* (6), 062126.

(57) Wang, Y.; Jie, W.; Yang, C.; Wei, X.; Hao, J. Colossal Permittivity Materials as Superior Dielectrics for Diverse Applications. *Adv. Funct. Mater.* **2019**, *29* (27), 1808118.

(58) Hutagalung, S. D.; Ooi, L. Y.; Ahmad, Z. A. Improvement in Dielectric Properties of Zn-Doped $CaCu_3Ti_4O_{12}$ Electroceramics Prepared by Modified Mechanical Alloying Technique. *J. Alloys Compd.* **2009**, *476* (1), 477–481.

(59) Boonlakhorn, J.; Kidkhunthod, P.; Chanlek, N.; Thongbai, P. (Al^{3+}, Nb^{5+}) Co–Doped CaCu3Ti4O12: An Extended Approach for Acceptor–Donor Heteroatomic Substitutions to Achieve High–Performance Giant–Dielectric Permittivity. *J. Eur. Ceram. Soc.* **2018**, *38* (1), 137–143.

(60) Jumpatam, J.; Putasaeng, B.; Chanlek, N.; Boonlakhorn, J.; Thongbai, P.; Phromviyo, N.; Chindaprasirt, P. Significantly Improving the Giant Dielectric Properties of $CaCu_3Ti_4O_{12}$ Ceramics by Co-Doping with Sr^{2+} and F^- Ions. *Mater. Res. Bull.* **2021**, *133* (111043), 111043.

Chapter 6. General Conclusions

As described in Chapter 1, lead-free ferroelectric materials have been attracting much attention because of the environmental concern. In order to design novel lead-free ferroelectrics, I have focused on the distortion of non-lead cations, i.e., first- or second-order Jahn-Teller distortions of V^{4+} and Nb^{5+}. I synthesized two novel polar materials, $CaMn(Ti_{1-x}V_x)_2O_6$ which combine the first-order Jahn-Teller distortion of V^{4+} and an order-disorder type ferroelectric mechanism, and $CuNbO_3$, where the coexistence of the second-order Jahn-Teller distortion of Nb^{5+} with the covalent nature of Cu-O bonding leads to an unusual dipole ordering. The latter compound also shows a novel topochemical reaction with cation-deinsertion, forming a novel colossal permittivity material, $CuNb_2O_6$.

The result in each chapter is summarized as below.

In Chapter 3, I investigated the structural evolution and physical properties of $CaMn(Ti_{1-x}V_x)_2O_6$. I successfully found enhanced spontaneous polarization, by the combination of the first-order Jahn-Teller active V^{4+} ion and an order-disorder mechanism in $CaMnTi_2O_6$. The maximum P_s value was observed for $x = 0.4$, and is 1.7 times larger than that for $x = 0$. On the other hand, the presence of antisite disorder between Ca^{2+} and Mn^{2+} associated with Mn−V inter-metallic charge transfer hindered such a V^{4+} displacement in V^{4+}-rich composition as shown by our magnetic and HAXPES studies.

In Chapter 4, I found the perovskite-type $CuNbO_3$ shows an unusual temperature-induced ferrielectric-ferroelectric phase transition. The high-temperature phase adopts a “collinear ferroelectric” $R3c$ structure. It transforms into the low-temperature “noncollinear ferrielectric” Pc structure at 470 K, accompanied by the antiparallel off-center Nb^{5+} displacement. The Pc structural distortion originates from the coexistence of Cu-O and Nb-O covalencies, highlighting that the bonding nature of both cations, as well as the tolerance factor, has a great impact on electric dipole order in perovskites.

In Chapter 5, I investigated a novel topochemical reaction, the combination of the high-pressure synthesis and subsequent ambient-pressure post-annealing. This reaction represents a rare example of cation-deinsertion, forming the novel perovskite-type $CuNb_2O_6$. I found this compound crystallizes in an A-site deficient quadruple perovskite structure and exhibits colossal dielectric constant up to 10^4. This colossal value can be attributed to an extrinsic effect, i.e., space charge, as previously reported in related quadruple perovskite-type compounds, $CaCu_3Ti_4O_{12}$ and $CuTa_2O_6$.

The conclusion of the whole thesis is that we can design ferroelectric materials exhibiting fascinating behavior by not just introducing first- or second-order Jahn-Teller active V^{4+} or Nb^{5+}, but combining these cations with other distortions, i.e., order-disorder type ferroelectric mechanism or Cu-O covalency. I revealed that in such ways, colossal displacement of V^{4+} in lead-free compounds and unusual cation dipole ordering in a noncollinear ferrielectric manner can be induced, which will provide a new design concept for high-performance ferroelectrics. In addition, I successfully observed a novel topochemical reaction accompanied by cation-deinsertion. This type of reactions will provide novel metastable functional materials.

Acknowledgements

I sincerely appreciate my supervisor, Professor Masaki Azuma, for his continuous support and encouragement.

I would like to acknowledge Professor Takafumi Yamamoto, Professor Takao Sasagawa, Professor Hiroshi Funakubo, Professor Hitoshi Kawaji for serving as my committee and giving fruitful pieces of advice.

Besides, I am deeply grateful to the following collaborators for their supports and discussion.
Professor Katsuhisa Tanaka (Kyoto University), Professor Koji Fujita (Kyoto University), Professor Ikuya Yamada (Osaka Prefecture University), Professor Hidenobu Murata (Osaka Prefecture University), Professor Olivier Hernandez (Univ Rennes), Dr. Clemens Ritter (Institut Laue-Langevin), Professor Jürgen Rödel (Technische Universität Darmstadt), Mr. Mao-Hua Zhang (Technische Universität Darmstadt), Dr. Shogo Kawaguchi (Japan Synchrotron Radiation Research Institute), Professor Mitsuru Itoh (Tokyo Institute of Technology), Professor Shin-ya Koshihara (Tokyo Institute of Technology), Professor Yoichi Okimoto (Tokyo Institute of Technology), Mr. Hongwu Yu (Tokyo Institute of Technology), Mr. Chihiro Takahashi (Kyoto University), and Mr. Yuya Yoshida (Kyoto University)

I greatly thank supports of Azuma-Yamamoto group members; Dr. Yuki Sakai, Dr. Kei Shigematsu, Dr. Zhao Pan, Dr. Lei Hu, Dr. Takahiro Ogata, Dr. Takumi Nishikubo, Mr. Takuma Itoh, Mr. Hayato Ishizaki, Ms. Marin Katsumata, Mr. Kotaro Ohashi, Mr. Shogo Wakazaki, Mr. Keita Ozawa, Ms. Kana Matsuno, Mr. Kazuma Miyazaki, Mr. Yusuke Arai, Mr. Takuya Ohmi, Ms. Shiori Kihara, Mr. Akira Sugai, Mr. Jinya Suzuki, Mr. Qiumin Liu, Mr. Koomok Lee, Mr. Hiroyasu Okochi, Mr. Jei Okajima, Mr. Takehiro Koike, Mr. Ryotaro Hanabusa, Mr. Teppei Nagase, Mr. Yasuhito Nagase, Mr. Masahito Ikeda, Mr. Ryuju Itoh, Mr Taiki Kosuge, Mr. Takatoshi Hiro-oka, Ms. Miwa Shimoda, Mr. Kota Yoshikawa, and Ms. Kaori Handa.

Finally, I truly appreciate my wife.

Masayuki Fukuda

Achievements

List of publications

Chapter 3.

[1] **Masayuki Fukuda**, Takumi Nishikubo, Zhao Pan, Yuki Sakai, Mao-Hua Zhang, Shogo Kawaguchi, Hongwu Yu, Yoichi Okimoto, Shin-ya Koshihara, Mitsuru Itoh, Jurgen Rodel, and Masaki Azuma,* "Enhanced Spontaneous Polarization by V^{4+} Substitution in a Lead-Free Perovskite $CaMnTi_2O_6$.", *Inorganic Chemistry*, **59**, 11749-11756, 2020

Chapter 4.

[2] **Masayuki Fukuda**, Ikuya Yamada, Hidenobu Murata, Hajime Hojo, Olivier Hernandez, Clemens Ritter, Katsuhisa Tanaka, and Koji Fujita,* "Perovskite-Type $CuNbO_3$ Exhibiting Unusual Noncollinear Ferrielectric to Collinear Ferroelectric Dipole Order Transition.", *Chemistry of Materials*, **32**, 5016-5027, 2020.

Chapter 5.

[3] **Masaayuki Fukuda**,* Ikuya Yamada, Hajime Hojo, Chihiro Takahashi, Yuya Yoshida, Katsuhisa Tanaka, Masaki Azuma, and Koji Fujita,* "Topochemical synthesis of perovskite-type $CuNb_2O_6$ with colossal dielectric constant.", *Journal of Materials Chemistry C*, **9**, 13981-13990, 2021.

Others

[4] Koji Fujita, Takahiro Kawamoto, Ikuya Yamada, Olivier Hernandez, Hirofumi Akamatsu, Yu Kumagai, Fumiyasu Oba, Pascal Manuel, Ryo Fujikawa, Suguru Yoshida, **Masayuki Fukuda**, Katsuhisa Tanaka, "Perovskite-Type $InCoO_3$ with Low-Spin Co^{3+}: Effect of In–O Covalency on Structural Stabilization in Comparison with Rare-Earth Series." *Inorganic Chemistry* **56**, 11113–11122, 2017.

[5] Zhehong Liu, Yuki Sakai, Junye Yang, Wenmin Li, Ying Liu, Xubin Ye, Shijun Qin, Jinming Chen, Stefano Agrestini, Kai Chen, Sheng-Chieh Liao, Shu-Chih Haw, Francois Baudelet, Hirofumi Ishii, Takumi Nishikubo, Hayato Ishizaki, Tatsuru Yamamoto, Zhao Pan, **Masayuki Fukuda**, Kotaro Ohashi, Kana Matsuno, Akihiko Machida, Tetsu Watanuki, Shogo Kawaguchi, Angel M Arevalo-Lopez,

Changqing Jin, Zhiwei J. Paul. Attfield, Masaki Azuma, and Youwen Long, “Sequential Spin State Transition and Intermetallic Charge Transfer in PbCoO^3.” *Journal of American Chemical Society*, **142**, 5731–5741, 2020.

[6] Zhao Pan, Mao-Hua Zhang, Takumi Nishikubo, Yuki Sakai, Hajime Yamamoto, Hajime Hojo, **Masayuki Fukuda**, Lei Hu, Hayato Ishizaki, Satoru Kaneko, Shogo Kawaguchi, Jurij Koruza, Jürgen Rödel, Masaki Azuma, “Polarization Rotation at Morphotropic Phase Boundary in New Lead-Free $Na_{1/2}Bi_{1/2}V_{1-x}Ti_xO_3$ Piezoceramics.” *ACS Applied Materials&Interfaces*, **13**, 5208–5215, 2021.

[7] Lei Hu, Yingcai Zhu, Yue-Wen Fang, **Masayuki Fukuda**, Takumi Nishikubo, Zhao Pan, Yuki Sakai, Shogo Kawaguchi, Hena Das, Akihiko Machida, Tetsu Watanuki, Shigeo Mori, Koshi Takenaka, and Masaki Azuma, “Origin and Absence of Giant Negative Thermal Expansion in Reduced and Oxidized Ca_2RuO_4.” *Chemistry of Materials* **33**, 7665–7674, 2021.

List of Presentations

International conferences

[1] **Masayuki Fukuda**, Takumi Nishikubo, Yuki Sakai, Hongwu Yu, Yoichi Okimoto, Shin-ya Koshihara, Masaki Azuma "Change in Spontaneous Polarization of Order-disorder Ferroelectrics Induced by V^{4+}." The 10th Asian Conference on High Pressure Research (ACHPR10), Online, November, 2021 (*Oral*).

[2] **Masayuki Fukuda**, Ikuya Yamada, Hidenobu Murata, Hajime Hojo, Katsuhisa Tanaka, and Koji Fujita, "Reversible phase transition and irreversible topochemical reaction in a perovskite-type $CuNbO_3$" The 11th International Conference on the Science and Technology for Advanced Ceramics (STAC-11), Ibaraki, Japan, July, 2019 (*Poster*).

[3] Yiran Wang, **Masayuki Fukuda**, Romain Gautier, Atsushi Miyake, Sergey Nikolaev, Hena Das, Masashi Tokunaga, Masaki Azuma, Kenneth R. Poeppelmeier “Low-dimensional Magnetism with Triangular “CuV2” Motifs” 2021 MRS Fall Meeting, Online, December, 2021 (*Oral*)

Japanese domestic conferences

[1] ○**福田真幸**, 西久保匠, Hongwu Yu, 沖本洋一, 腰原伸也, 東正樹, 酒井 雄樹「新規 A サイト柱状秩序ダブルペロブスカイト $CaZnV_2O_6$ の高圧合成」『日本セラミックス協会 2021 年年会』, オンライン, 2021 年 3 月, （*口頭*）

[2] ○福田真幸, 東正樹, Yiran Wang, Kenneth Poppelmeier, 三宅厚志, 徳永将史「S=1/2 テトラマースピンギャップ物質$[\mathrm{Cu(4,4'\text{-}Me_2\text{-}bpy)(H_2O)}]_2[\mathrm{V_2O_2F_8}]$」『日本物理学会第 76 回年次大会』, オンライン, 2021 年 3 月, （*口頭*）

[3] ○福田真幸, 西久保匠, Zhao Pan, Hongwu Yu, 沖本洋一, 腰原伸也, 伊藤満, 東正樹, 酒井雄樹, Mao-Hua Zhang, Jurgen Rodel, 河口彰吾「非鉛強誘電体 $\mathrm{CaMnTi_2O_6}$ の $\mathrm{V^{4+}}$置換による自発分極の変化」『日本セラミックス協会第 33 回シンポジウム』, オンライン, 2020 年 9 月, （*口頭*）

[4] ○福田真幸, 西久保匠, 東正樹, 酒井雄樹「非鉛強誘電体 $\mathrm{CaMnTi_2O_6}$ の $\mathrm{V^{4+}}$置換による自発分極増大」『日本セラミックス協会 2020 年年会』, 東京, 2020 年 3 月, （*口頭*）

[5] ○福田真幸, 東正樹「A サイト columnar 秩序型ペロブスカイトの高圧合成と誘電特性」『第 60 回高圧討論会』, 北海道, 2019 年 10 月, （*口頭*）

[6] ○福田真幸, 山田幾也, 北條元, 田中勝久, 藤田晃司「ペロブスカイト型酸化物 $\mathrm{CuNbO_3}$ の高圧合成とトポケミカル分解」『日本材料学会材料シンポジウムワークショップ』, 京都, 2018 年 10 月, （*口頭*）

[7] ○福田真幸, 山田幾也, 北條元, 田中勝久, 藤田晃司「ペロブスカイト型酸化物 $\mathrm{CuNbO_3}$ の高圧合成とその特異な熱分解挙動」『日本セラミックス協会第 31 回秋季シンポジウム』, 愛知, 2018 年 9 月, （*口頭*）

Awards

[1] Gold Poster Award, The 11th International Conference on the Science and Technology for Advanced Ceramics (STAC-11), (2018)